9-27-2021

Mid-Miocene Icelandites of Eastern Oregon: Petrogenesis and Magmatic Lineage to Main-Phase CRBG with Constraints on Storage Sites

Melissa Aileen Carley
Portland State University

Mid-Miocene Icelandites of Eastern Oregon:

Petrogenesis and Magmatic Lineage to Main-Phase CRBG with

Constraints on Storage Sites

by

Melissa Aileen Carley

A thesis submitted in partial fulfillment of the
requirements for the degree of

Master of Science
in
Geology

Thesis Committee:
Martin J. Streck, Chair
John Bershaw
Barry Walker Jr.

Portland State University
2021

Abstract

The La-Grande Owyhee eruptive axis is a mid-Miocene to Pliocene ~300 km long volcanic belt located at the eastern margin of the Columbia River Basalt Group (CRBG) in Oregon. Within this volcanic belt there are numerous vents that have produced a large volume of petrologically diverse rocks ranging from the tholeiitic flood basalts of the CRBG to rhyolitic tuffs of caldera complexes such as the Lake Owyhee Volcanic field. Icelandites, which are iron rich andesites, are known to occur in association with silica saturated to oversaturated tholeiitic basalts as a minor part of continental flood basalt volcanism. This study investigates these icelandites. This includes summarizing their currently known extent, documenting their compositional variations, describing their lithologic and petrographic characteristics, and to petrogenetically relate icelandite magmas to main stage CRBG magmas..

Prior mapping and our work in eastern Oregon have revealed numerous occurrences of mid-Miocene Fe-rich andesite (icelandite) lavas among flood basalts and rhyolites of the Columbia River magmatic province in eastern Oregon from north of Baker City to McDermitt along the Oregon-Nevada state border. Icelandite lavas typically overlie main units of the Columbia River Basalt Group (CRBG) and are intercalated with mid-Miocene rhyolites. This stratigraphic control and select radiometric ages (new and existing) indicate they range in age from >16 Ma (e.g., 16.1) to ~15 Ma suggesting icelandites represent the last pulse of main phase CRBG volcanism. Icelandites are found in

proximal mafic pyroclastic deposits, lava flows or as magmatic components in strongly zoned (rhyolite-icelandite) ignimbrites.

Our compiled data set in combination with published data are used to investigate processes involved in formation of these rocks. Icelandites of eastern Oregon range from ~57 to 63 wt% SiO_2, with >8 wt% FeO* and as high as 13.4. FeO*/MgO can be as high as 14 and Mg # ranges from 7.1 to 26.1. Although FeO* and FeO*/MgO is characteristically high in all samples, there are subtle differences within icelandites yielding two groups that internally vary with increased silica as discerned mostly by Nb, Ta, Zr, Hf, Th, and rare earth elements. The trace element enriched Group 1 has lower Al_2O_3 content than the samples of the trace element depleted Group 2. Internally, both groups vary in their TiO_2 that decreases with increased SiO_2. The two icelandite groups are petrogenetically modeled as being derived from main phase CRBG. The more enriched Group 1 is more consistent with a parent magma similar to the Imnaha Basalt. The compositions of the less enriched Group 2 are consistent with a Picture Gorge Basalt parent magma and Grande Ronde basaltic andesite samples (including Hunter Creek and Birch Creek samples of the Malheur Gorge area) as intermediary compositions. This suggests that the majority of these icelandites are the products of continued magmatic evolution from magmas of the Grande Ronde Basalt through a combination of processes including fractionation and mixing with felsic material such as a rhyolite or contamination with country rock.

Table of Contents

List of Tables

List of Figures

Introduction

The lava flows of the mid-Miocene Columbia River Basalt Group (CRBG) cover ~200,000 km^2 in Oregon, Washington, and Idaho. The La Grande-Owyhee eruptive axis lies between the main outcrop area of the CRBG exposed across the Columbia plateau in the north and mid-Miocene bimodal eruptive centers exposed in the Owyhee plateau to the south (Ferns and McClaughry, 2013). It is in the La Grande-Owyhee eruptive axis and surroundings that geochemically and petrologically diverse suites of magmas ranging from tholeiitic, silicic, and calc-alkaline, to alkalic compositions have been erupted throughout the mid-Miocene and into the Pliocene of which some are not well studied. On the other hand, the main CRBG lavas to the north, exclusively comprising tholeiitic flood basalts, have been highly studied, and CRBG lavas west and south of the Baker graben are more intimately associated with silicic and intermediate compositions (Ferns and McClaughry, 2013).

Included in CRBG volcanism that started at 17.2 Ma (Cahoon, 2020) is the eruption of highly evolved tholeiitic andesites (icelandites) at several locations along the length of the eruptive axis (Figure 1B). Lavas classified as icelandite lavas have SiO_2 of 57-64 wt%, total FeO >8 wt%, less than 16.5 wt% Al_2O_3, TiO_2 <3 wt% and low alkali content (Carmichael, 1964; Irvine and Baragar, 1971). The much higher iron content of icelandites is a characteristic difference to typical andesites of volcanic arcs.
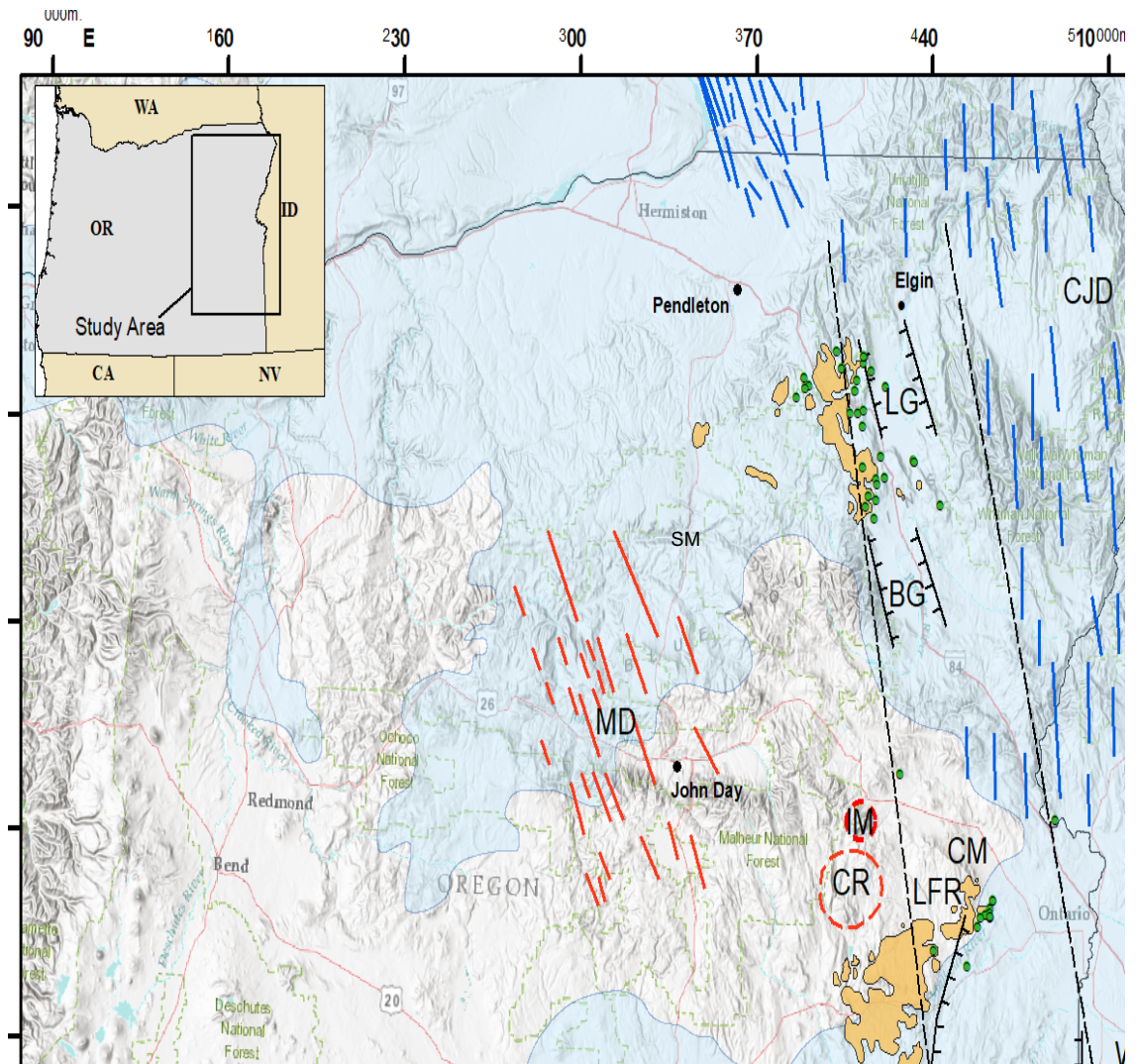
Figure 1. Map showing La Grande-Owyhee eruptive axis and the first two stages in the evolution along it. Regional features are as follows: WA—Washington; OR—Oregon; ID—Idaho; LG—La Grande graben; CRBG—Columbia River Basalt Group; BG—Baker graben; OIG—Oregon-Idaho graben; CR—Castle Rock Caldera; SM—Strawberry Volcanics; IM—Ironside Mountain; SD—Steens Dike Swarm; MD—Monument dike swarm; CJD—Chief Joseph dike swarm; LFR—Littlefield Rhyolite; CM—Rhyolite of Cottonwood Mountain; WSRP—Western Snake River Plain. Extent of the Columbia River Basalt Group, stage 1 flood basalts (blue shade), in eastern Oregon. Extent of stage 2 icelandite lavas (pre-2017 extent) along the eruptive axis shown in orange shade (from Ferns and McClaughry, 2013). Published data points (pre-2017 samples) taken from previous work by: Bailey (1989), Binger (1997), Brooks (1992, 2006), Brooks and O'Brien (1992a,b), Brueseke and Hart (2007), Camp et al. (2003), Edwards (2013), Ferns and McClaughry (2013), Ferns and McConnell (2005), Ferns et al (2010), Ferns (1989a), Ferns and O'Brien (1992a,b), Hooper et al. (2002a), Korosec (1987), Lees (1994), MacLeod (1990a), Madin (1997), Wright (1979) and Wright et al. (1980) and Zimmerman (1991).

The term icelandite was first coined by I.S.E. Carmichael in his 1964 study of the

petrology of the Tertiary Thingmuli volcano in eastern Iceland to describe iron-rich

alumina-poor andesites that were geochemically different from orogenic andesites. Subsequent research by several authors in the decades since Carmichael's study on Thingmuli has been able to better identify the major element geochemical characteristics of icelanditic lavas. Icelandites differ most consistently from orogenic andesites at plate boundaries by being enriched in Fe, Mn, P, and Ti but depleted in Al, Ca, and Mg at any given silica content (Gill, 1981). In the years since the study of Thingmuli, icelandites have been found to primarily exist in large igneous provinces such as Etendeka-Parana, Columbia River Basalt Group, North Shore Volcanic Group-Keweenawan Plateau lavas, and the North Atlantic Igneous Province (NAIP), the intra-continental volcanics of the Dongargarh fold belt in India as well as rift margins such as Iceland. The icelandites associated with the Columbia River Basalt Group are subject of this study. This includes summarizing their currently known extent, documenting their compositional variations, describing their lithologic and petrographic characteristics, and to petrogenetically relate icelandite magmas to main stage CRBG magmas.

Background

GEOLOGIC SETTING

The Columbia River Basalt Group (CRBG; Figure 1) constitutes the Earth's youngest large igneous province (Barry et al., 2013). The Columbia River flood basalt province covers most of eastern Washington and Oregon, western Idaho, and part of northern Nevada (Reidel et al., 2013). Eruptive activity within the CRBG was generally agreed to have begun in the mid-Miocene at 16.8 Ma (Barry et al., 2013) but new data suggest that it started earlier at 17.2 (Cahoon, 2020). The Columbia River Basalt Group is estimated to have a total volume of 210,000 km^3 and an areal extent of 208,000 km^2 (Reidel et al., 2013). The members included in the CRBG are the Steens Basalt, Imnaha, Grande Ronde, Wanapum, and Saddle Mountain Basalts as well as the Picture Gorge Basalt and Prineville Basalt (Reidel and Tolan, 2013; Figure 2).

4
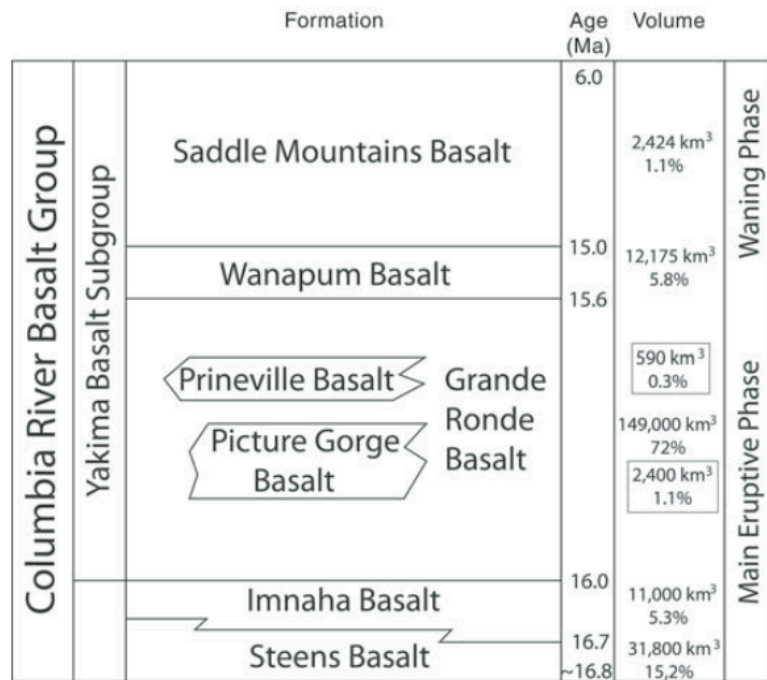
Figure 2. Stratigraphic column illustrating the major subdivisions of the Columbia River Basalt Group. (from Reidel et al., 2013).

More recent studies utilizing advancements in mapping and geochronological analyses have suggested that the basalt of Malheur Gorge, which is located to the south of most of the original main phase units (Imnaha and Grande Ronde Basalts), is a lava flow package composed of Steens Basalt at the base, Imnaha Basalt in the middle and Grande Ronde Basalt on top and thus represents an area were CRBG lavas from the north (Imnaha and Grand Ronde Basalt) overlap (Figure 3) with those lavas coming from the south (Steens Basalt) (Hooper et al., 2002; Camp et al., 2003). Newest data now suggest that lavas of the Picture Gorge Basalt reach into the Malheur Gorge area as well (Cahoon, 2020).

Figure 3. (Correlation diagram)

La Grande and Baker grabens	Oregon-Idaho graben
Powder River volcanic field — Alkalic volcanics: Jones Butte vent (2.1 Ma); Tamarack Mountain lavas (3.2 Ma); Spring Mountain lavas / Alkalic vents near Elgin (7.3–6.5 Ma); Basanite lavas (10.8 Ma)	*Alkalic volcanics:* Kivett sequence lavas (1.9–0.8 Ma); Sourdough sequence / Graveyard Point sill (6.7 Ma) / Lavas (7.8 Ma)
Calc-alkaline volcanics: Mount Harris, Mount Emily, and Sawtooth Crater volcanoes; Dacite and andesite lavas (13.8–11.9 Ma)	*Calc-alkaline volcanics:* Keeney sequence / Andesite at Vines Hill (11.45, 10.87, and 10.3 Ma)
Little Catherine Creek basalt (14.4–13.3 Ma)	Timms Peak basalt
Wanapum Basalt: Powatka lava flow / basalt of Dodge; Fiddlers Hell member (15.54 Ma); Dooley Mountain rhyolite (15.59 Ma). *Lake Owyhee volcanic field:* Dinner Creek Tuff (16.16–15 Ma)	*Lake Owyhee volcanic field:* Dinner Creek Tuff (16.16–15 Ma); Mahogany Mountain caldera (15.9–15.6 Ma); Upper Littlefield Rhyolite (16.05 Ma; 16.01 Ma); Hunter Creek Basalt (~16.1 Ma); Lower Littlefield Rhyolite (16.20 Ma; 16.12 Ma); Unity rhyolites (?) (~17.00–16.54 Ma)
Grande Ronde Basalt (N2, R1): Winter Water Member (N2); Mount Horrible and Wapshilla Ridge Members (R2)	*Malheur gorge basalt:* Birch Creek basalt; basalt of Bishops Ranch(?); Upper Pole Creek basalt (16.42 Ma); Lower Pole Creek basalt
Imnaha Basalt	

(Left margin labels: La Grande-Owyhee eruptive axis; Stages 6, 5, 4, 2–3, 1–2; Columbia River Basalt Group.)

Figure 3. Correlation diagram of stratigraphic relationships between mapped units of the La Grande-Owyhee eruptive axis. The Dinner Creek Tuff, shown in gray, is exposed over a wide geographic area from north to south along the eruptive axis. Magnetic polarities are listed within the Grande Ronde Basalt identify magnetostratigraphic units defined by Reidel et al. (2013). Abbreviations: Ma, mega-annum (million years before present); "(?)," stratigraphic position uncertain. (Figure from Ferns, et al., 2017).

The Grande Ronde Basalt represents the main pulse of Columbia River Basalt Group volcanism (Swanson et al., 1979a). Grande Ronde eruptive activity began in the mid-Miocene from the end of the Imnaha Basalt at ~16.4 Ma to the end of the Grande Ronde Basalt volcanism at ~15.9 Ma (Wolff and Ramos, 2013). Flows of the Grande Ronde Basalt erupted from the Chief Joseph dike swarm of northeastern Oregon/southwestern

Washington and produced 150,400 km^3 of basaltic lavas that covered ~169,600 km^2.

These are among the largest known lava flows on Earth (Figure 2) and provide an

excellent example of the magnitude of flood basalt volcanism (Reidel and Tolan, 2013).

The La Grande-Owyhee eruptive axis (LOEA) in eastern Oregon is a north-northwest

trending, ~300 km long mid-Miocene to Pliocene volcanic belt located near the eastern

margin of the CRBG province (Ferns and McClaughry, 2013). The eruptive axis extends

from the town of Elgin on the north to the town of Jordan Valley on the south and is

juxtaposed between the Chief Joseph dike swarm on the east and the Monument dike

swarm and

the middle Miocene Strawberry Volcanics on the west (Figure 1). It is defined by

numerous volcanic vents, contained within or directly adjacent to the La Grande, Baker,

and Oregon-Idaho grabens, from which a diverse assemblage of tholeiitic, silicic, calc-

alkaline, and alkalic lavas erupted (Ferns and McClaughry, 2013). The volcanic rocks that

erupted from and are preserved within the eruptive axis stratigraphically link northern

exposures of CRBG units with correlative mid Miocene basaltic lavas exposed over vast

parts of SE Oregon and Northern Nevada (Ferns and McClaughry, 2013).

Volcanism along the LOEA progressed through six stages, beginning in the middle

Miocene and continuing through the Pliocene. Stage 1 (17.2-15.5) in the evolution of

the eruptive axis were the fissure eruptions of the Grande Ronde Basalt member of the

CRBG. The 2nd stage (16.1-15.2 Ma) was marked by fissure eruptions of highly evolved

tholeiitic lavas (icelandites) along the length of the eruptive axis. Caldera forming

eruptions of rhyolitic lavas and rhyolitic ash-flow tuffs from eruptive centers including

the Littlefield Rhyolite, Dinner Creek Tuff, and Lake Owyhee Volcanic Field along the

central and southern extents of the axis comprised stage 3 (15.5-14.7 Ma) of volcanic

activity. In stage 4 (14.7-13.7 Ma), fissure eruptions produced olivine basalts along the

length of the eruptive axis. Stage 5 (13.5-10.0 Ma) in the characterized by the eruption

of calc-alkaline basaltic andesite, andesite, and dacite lavas along the length of the

eruptive axis. Finally, stage 6 (7-1 Ma) was defined by small volume alkalic eruptions

along the length of the LEOA (Ferns and McClaughry, 2013).

ICELANDITE DISTRIBUTION
Icelandites can be found in both the northern and southern sections of the La Grande-

Owyhee eruptive axis (Figure 1). In the northern end of the eruptive axis the icelandite

lavas form a geochemically distinct unit known as the Fiddler's Hell member and can be

found on top of the Grande Ronde basalts on the west side of the La Grande graben.

Bailey (1990) reported several analyses indicating that Fiddlers Hell lavas also form

isolated erosional remnants atop pre-Tertiary basement rocks east of the Baker graben.

Lavas with similar icelanditic compositions to Fiddlers Hell can be found near Indian

Rock on Mt Emily just west of La Grande as well as to the north and south of Ironside

Mountain. In the southern part of the La Grande-Owyhee eruptive axis, icelandite-type

lavas have been recorded as part of the Hunter Creek Basalt by Ferns and McClaughry

(2013) and Camp et al. (2003). Iron-rich andesite and basaltic andesite lavas are also

exposed on the east, near the Oregon-Idaho border. Zimmerman (1991) described a

succession at Indian Head Mountain in Washington County, Idaho, wherein flows of

icelandite lavas are separated from the Grande Ronde Basalt lavas by a dacitic ash-flow tuff (Ferns and McClaughry, 2013). Zimmerman described the evolved (icelandite) flows as averaging up to 20 meters in thickness with flows being typically fine grained, aphyric and comprised of plagioclase, augite, spinel, and glass. The geochemistry of the icelanditic flows is said to be distinguished from local Grande Ronde flows by their slightly more evolved nature which is higher in SiO_2 and K_2O and lower in MgO and CaO. This was the status of knowledge on the compositions and distribution of icelandites (as compositionally defined above) before MS thesis work by Cruz (2017), Webb (2017), and this study.

Methods

SAMPLE COLLECTION

Samples for this study were collected during fieldwork in summer of 2017 (Figure 4).

The field area for this study covers an area of roughly 17,000 sq. miles from Pendleton in

the northwest corner to Jordan Valley in the southeast corner. The primary focus in the

northern half of the field area, which contains the La Grande graben and the Baker

graben, was to resample at 29 locations that had been previously mapped and to

further investigate the areas around the sample locations to verify the previously

mapped extents of icelandite units. For icelandites of the southern field area, 25

samples and associated outcrop locations for this study came from prior MS thesis work

by Cruz (2017), Webb (2017), and unpublished data from my advisor, Dr. Martin Streck,

acquired since 2012. These 25 samples were added to 11 new samples that were

collected during this study.

The samples that were collected during fieldwork for this study were given ID's denoting

the initials of the collector (MAC) followed by the year and the sample number. For

locations with more than one sample, the sample number included a letter identifier as

well. While in the field, characteristics of the units from which samples were collected

were recorded, major lithological characteristics of overlying and underlying units at

sample locations when visible were noted, as well as GPS coordinates of the locations

using the Avenza Maps app for iPhone and a Garmin eTrex handheld GPS unit.
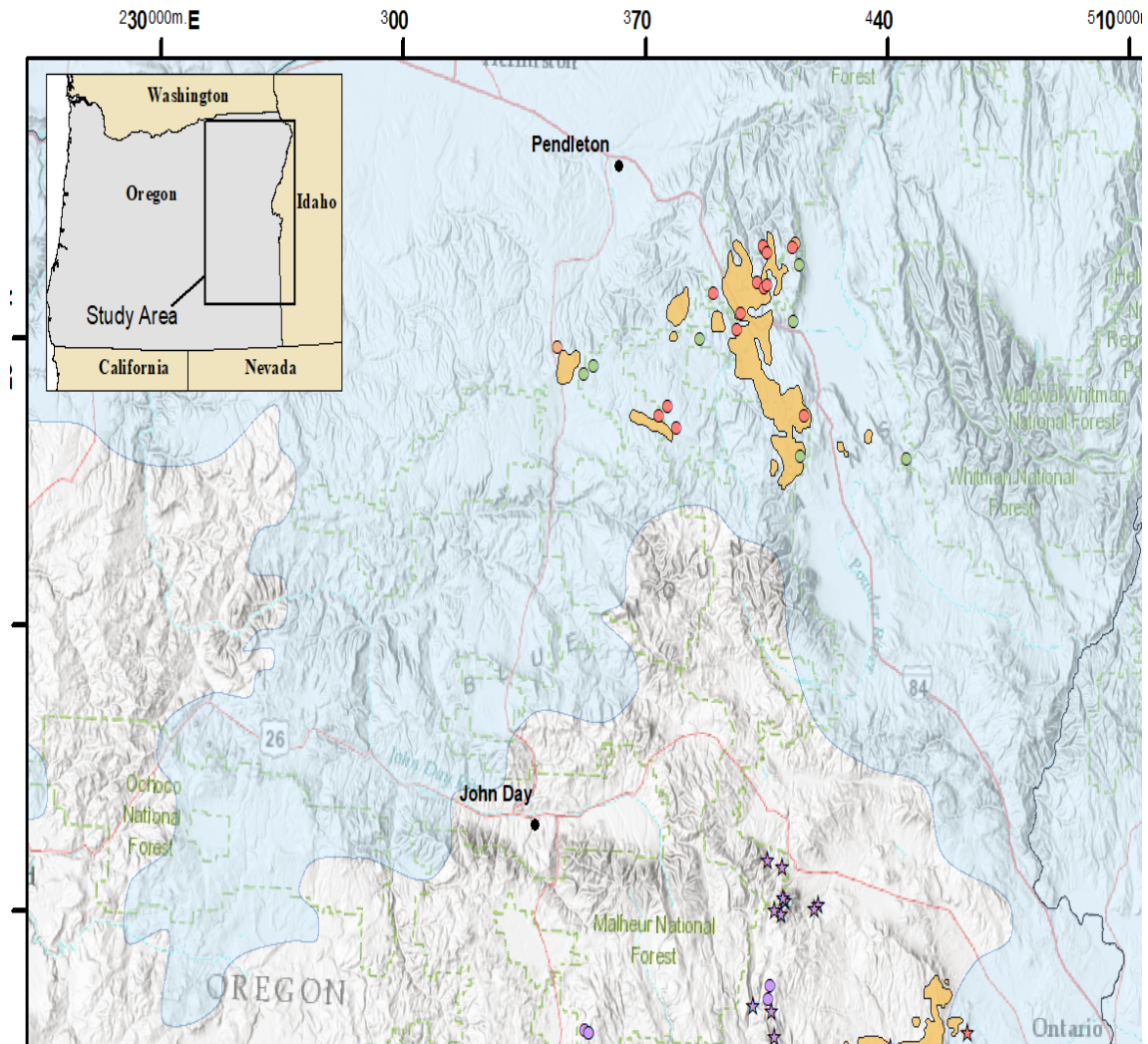
Figure 4. Map of study area in eastern Oregon. Mapped extent of icelandites prior to 2017 fieldwork is shown in orange shade. CRBG extent is shown in blue shade. Base map from ArcGIS online library.

PREPARATION AND GEOCHEMICAL ANALYSIS

Thirty-one samples were selected from the 42 samples collected during this study for

bulk rock analysis. The samples were chipped using a chipmunk rock crusher in the

facilities at Portland State University to uniform size fraction of ~0.5cm and then

handpicked to remove weathering rinds, secondary mineralization in vesicles and other

alteration products. The samples were then taken to the Peter Hooper GeoAnalytical lab

at Washington State University in Pullman Washington. There the samples underwent

11

further preparation where the rock chips were broken down into a powder, 3.5g of the

powder was mixed with 7.0g dilithium tetroborate flux and fused into glass beads for

XRF analysis. For ICP-MS analysis 250mg of the sample and flux powder mixture for the

samples were dissolved in acid solutions. The glass beads and rock-acid solutions were

then analyzed for major and trace element elemental concentrations using the Thermal

–ARL automated x-ray fluorescence spectrometer (XRF) for the glass beads and Agilent

inductively coupled plasma mass spectrometer (ICP-MS) for the rock-acid solutions.

Data collected from the XRF and ICP-MS analysis can be found in the appendices (see

Appendix A).

PETROGRAPHIC AND SEM ANALYSIS
Petrographic analysis was completed at Portland State University using a Zeiss

Primotech polarized light microscope to analyze samples of this study. Detailed

descriptions of the thin sections including textures, phenocryts size/shape, groundmass,

alteration products, mineral assemblages, and proportion of phenocrysts were recorded

and can be found in Appendix F. Five of the thin sections were carbon coated for SEM

analysis at Portland State University's Center for Electron Microscopy and

Nanofabrication (CEMN). The SEM analysis was conducted on the ZEISS Sigma VP FEG

SEM using back-scatter electron (BSE) imaging and energy-dispersive x-ray spectroscopy

(EDS) on specific minerals within the sections to determine their composition. The sites

that were selected for back-scatter electron imaging BSE and electron dispersive

spectroscopy (EDS) were the largest unaltered fracture less plagioclase and

clinopyroxene phenocrysts in the selected sections. A 5-10 microphenocrysts of

plagioclase and pyroxene were also selected from each thin section for EDS. The images

and EDS spectra were then processed using Oxford's Aztec software at Portland State

University. Data for plagioclase and clinopyroxenes analyzed using EDS were plotted

into ternary phase diagrams.

GEOCHEMICAL MODELING

Two models were set up, the first utilizing only fractional crystallization (Rayleigh

fractionation) to establish if icelandites could be generated from fractional

crystallization alone and the second model using magma mixing to evaluate if

icelandites could be plausibly generated from magma mixing between mid-Miocene

felsic magmas and a Grande Ronde type end member.

Fractional crystallization was used to assess the feasibility of producing icelandites via

Rayleigh fractionation from a parent magma (see below). Equation 2 is the rearranged

equation for fractional (Rayleigh) crystallization to solve for the daughter magma. In it,

the concentration C^l of a solid phase in the daughter magma, is a function of the

concentration of the solid phase in the parent magma, C^0, the bulk partition coefficient

$D,$ and the melt fraction remaining F.

$$C_l = F^{D-1} \times C_0 \tag{1}$$

In order to accurately model the formation of icelandites, partition coefficients (D-

values) were carefully selected from published sources of tholeiitic basalts and andesites

based on the identified mineral phases of the samples. Partition coefficients (K_D) were

interpolated when no published values could be identified (K_D values and sources can be

found in Appendix C, Table 1). The missing values were interpolated based on the

13

surrounding K_D values. A bulk partition coefficient was calculated for individual elements

based on the partition coefficient for individual phases using Equation 1, where $\overline{D}$, the

bulk partition coefficient for any element, *i*, is determined from the weight fraction *X* of

a solid mineral phase, *s,* and D_i^s, the partition coefficient for an element, *i*, in a solid

mineral phase.

$$\overline{D}_i = \sum X_s D_i^s \qquad (2)$$

Observed modal mineral proportions determined of icelandites and basaltic andesites of

the Grande Ronde/Hunter Creek Basalt along with the volatile free re-normalized CIPW

norms calculated from the bulk rock analyses were used to determine mineral

proportions to calculate bulk partition coefficients for the models. The parent magmas

were estimated by linearly tracing back on chemical plots from the icelandite to Grande

Ronde and Hunter Creek Basalt to identify the Grande Ronde/Hunter Creek Basalt

samples with the most plausible major and trace elemental concentrations. It was

deduced early on that the two groups of icelandites very likely came from two slightly

different parent magma bodies. The elemental concentrations of the two parent

magmas that were used for modeling reflect those subtle differences. The trace element

concentrations were calculated for 0% to 40% fractionation in 2% increments using the

partition coefficients that can be found in Appendix C. The calculated values for major

and trace elements were plotted in Harker diagrams versus SiO_2 and compared to the

averaged values of the icelandites groups. Trace element values and REE were plotted in

spider diagrams that were also compared to the averaged icelandites group values. The

spider diagrams of the resulting trace element and REE calculated values were

normalized using the primitive mantle of Sun and McDonough (1989) and C1 chondrite

normalizing values of McDonough and Sun (1995). The calculated values and diagrams

for Rayleigh crystallization can be found in Appendix D

The second model utilized Equation 3, which is a standard mass balance equation, to

determine if an icelanditic magma would result from mixing of a Grande Ronde type

endmember with a rhyolitic endmember. The rhyolitic endmembers used in the model

are the four units of the Dinner Creek Tuff as well as the upper and lower Littlefield

rhyolite,

$$C_m = C_a X_a + C_b(1 - X_a)$$ (3)

In the standard mass balance equation for mixing between two magmas, the

concentration of each element in the mixed magma is the sum of the elemental

concentration (C_a) in the mafic endmember, (X_a) is the mass fraction of the mafic

endmember in the mix, and (C_b) is the elemental concentration of the felsic endmember

in the mixture. The mixed magma was calculated for 0% to 50% mix in increments of 5%

for all felsic endmembers except for Dinner Creek Tuff Unit 4, which was calculated to

70%. The resulting trace element values of the mixed magma were normalized to the

primitive mantle of Sun and McDonough (1989) and C1 chondrite values of McDonough

and Sun (1995). The initial and calculated values for the binary mixing model can be

found in Appendix E.

Results

<small>LITHOLOGY</small>

The rocks of the Fiddlers Hell unit, which are found in the vicinity of the La Grande and

Baker grabens (Figure 5) are tholeiitic basaltic andesites and icelandites. These rocks

range in color from bluish gray to dark gray to almost black in color. The Fiddlers Hell

flows are generally fine-grained and range from aphyric in the lower-most flows to

sparsely (1-3%) plagioclase phyric in capping flows. Samples that were collected from

ridge top locations in and around the La Grande and Baker grabens had reddish brown

weathering rinds of up to ~1 cm in thickness covering the exterior. The flows themselves

were either platy or hackly and formed large slightly rounded blocks when found in

outcrops.
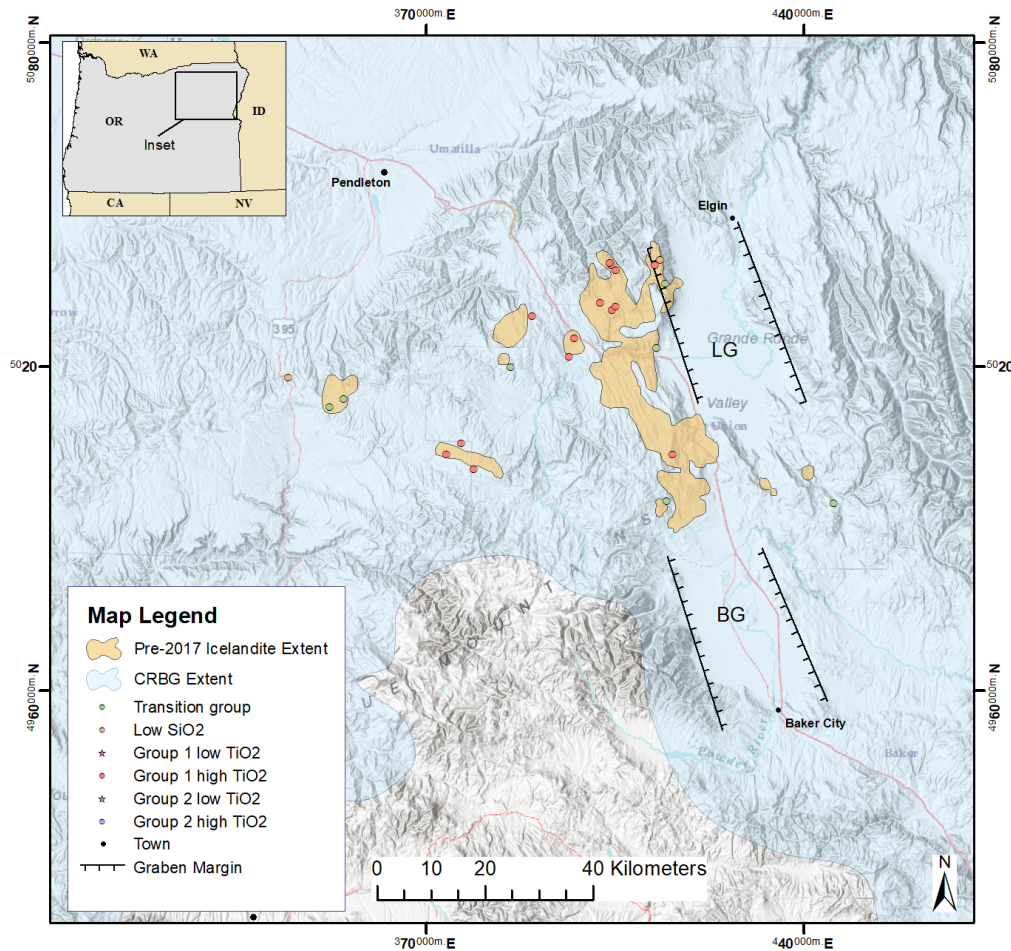
Figure 5. Map of northern half of study area. Regional features are as follows: WA—Washington; OR—Oregon; ID—Idaho; LG—La Grande graben; BG—Baker graben; Mapped extent of icelandites prior to 2017 fieldwork is shown in orange shade. CRBG extent is shown in blue shade. Base map from ArcGIS online library.

In the Malheur Gorge (Figure 6), icelandites occur as part of lava flows of the Hunter Creek Basalt unit and as the icelandite of Alder Creek mapped by Webb (2017). The flows of the ~16.1 Ma Hunter Creek Basalt overlie the 16.16-15 Ma Dinner Creek Tuff and intercalated between lower and upper Littlefield Rhyolite in the Malheur River Gorge (Webb et al., 2018). In the southern stratigraphic transect of Alder Creek canyon, Webb (2017) describes the occurrence of an icelandite lava (~62 wt % SiO_2) overlying the Dinner Creek Tuff. This icelandite lava forms steep talus dominated slopes that

obscure outcrops. The icelandite is itself overlain by a thin lens of moderately-welded dacitic tuff which directly underlies the glassy base of the upper Littlefield rhyolite. This icelandite was previously mapped as part of the Hunter Creek basalt on the basis of lithological characteristics and stratigraphy (Kittleman et al., 1967; Evans and Binger, 1999c) and thus is stratigraphically equivalent to the Hunter Creek Basalt (Webb, 2017). Icelanditic flows are generally indistinguishable from the bulk of the Hunter Creek Basalt that is more mafic, basaltic andesite lavas. All are gray to dark gray in color and very fine grained. These rocks are generally aphyric to very sparsely plagioclase phyric, nearly all phenocrysts are virtually undetectable with the unaided eye. Webb (2017) describes the icelandite of Alder Creek as being lithologically similar and petrogenetically linked to the Hunter Creek are geochemically distinct from the other icelandites observed in this study.
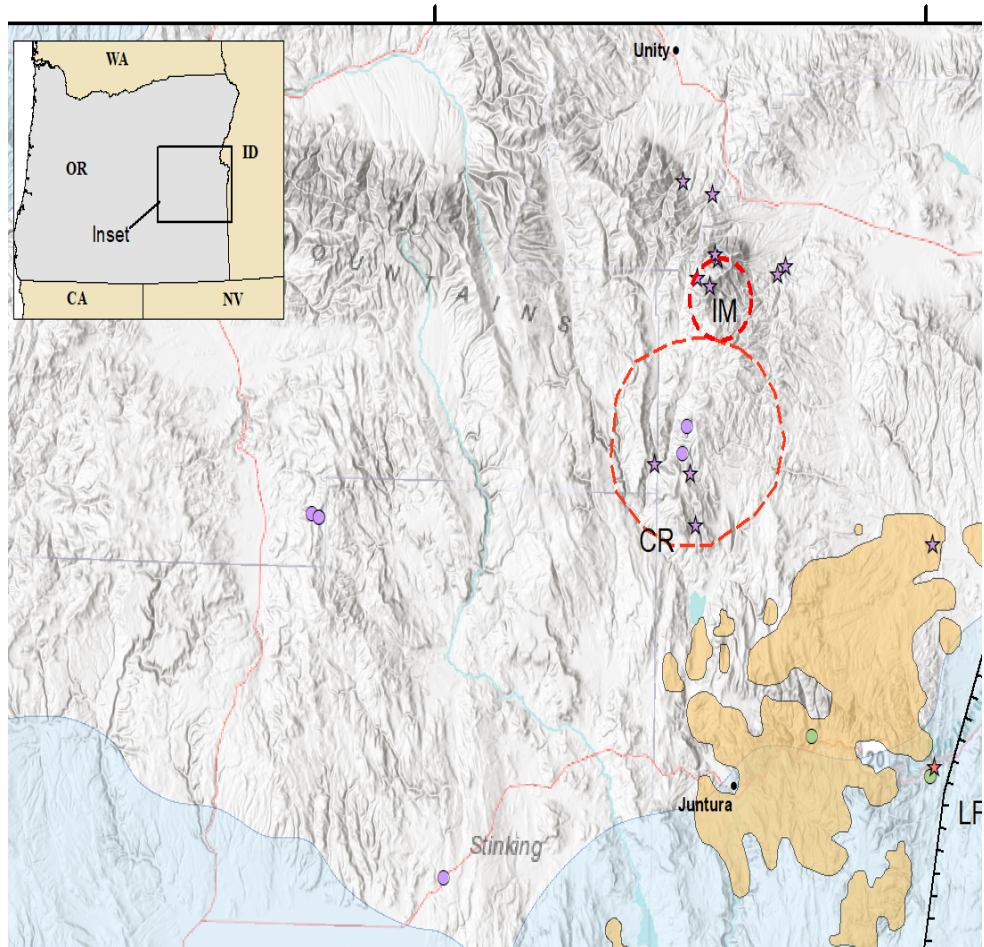
Figure 6. Map of Southern half of study area. Regional features are as follows: WA—Washington; OR—Oregon; ID—Idaho; OIG—Oregon-Idaho graben; CR—Castle Rock Caldera; SM—Strawberry Volcanics; IM—Ironside Mountain; LFR—Littlefield Rhyolite; CM—Rhyolite of Cottonwood Mountain; Mapped extent of icelandites prior to 2017 fieldwork is shown in orange shade. CRBG extent is shown in blue shade. Base map from ArcGIS online library.

In the field area of Cruz (2017) between Castle Rock in the south and Ironside Mountain in the north (Figure 6), samples of icelandites are found as sills, dikes, and lava flows. Some of these icelandites were emplaced along with aphyric basaltic andesites after the eruption of Dinner Creek Tuff eruptive units 1 and 2, which they intrude into. They are also known to overlie the intra-caldera tuffs and caldera floor sediments of the Castle Rock Caldera and Ironside Mountain Caldera. Cruz identifies six icelandites in his work through geochemical analysis and petrography, which has been expanded to include

19

MC-45-16, MC-69-16, MC-106-16, MC-15-16, and MC-98-16 using geochemical analysis

performed during this study.

PETROGRAPHY

A subset of 7 samples were selected from the 47 samples that were newly collected

during this study and six samples from the work of previous students. The samples

chosen for petrographic analysis were determined based on bulk geochemistry,

geographic location, and freshness of the sample. A complete table of the petrographic

analysis that includes texture, mineral phases, and mineral characteristics can be found

in Appendix F. The samples overall are fine grained aphanitic, with matrix material size

of less than or equal to 50 μm, with the matrix being comprised of plagioclase feldspar,

clinopyroxene, ilmenite, and magnetite, with sparse altered olivine. Samples are

generally aphyric to plagioclase phyric and sparsely pyroxene phyric. When phenocrysts

are present, they are small, mostly ranging in size from 70 μm to 500 μm. Larger

phenocrysts are rare, but a few have been found in select thin sections with a size of up

to 1.7 mm. The samples from the Fiddlers Hell unit (MAC-17-04a, MAC-17-06, MAC-17-

16, MAC-17-18, and MAC-17-29) contain between 1-3% phenocrysts, while the sample

MS-12-34 (Hunter Creek at Neal Hot Springs) has ~1% phenocrysts and MC-94-16

(icelandite from east of Ironside Mountain) contains <1% phenocrysts. The phenocrysts

are plagioclase feldspar and clinopyroxene (Figure 9-10). Twinning of plagioclase is

common and is a combination of simple and/or poly-synthetic twinning in these

sections. MAC-17-04a (Figure 7) and MAC-17-06 (Figure 8) are the only sections to

exhibit twinning in clinopyroxene of the Fiddlers Hell sample.
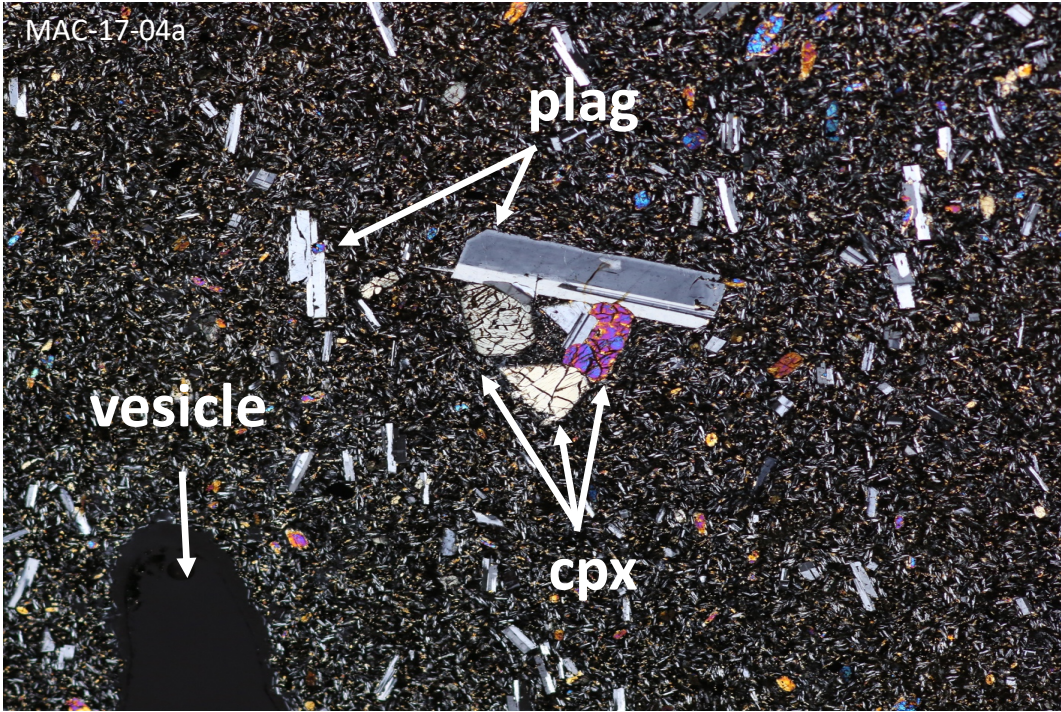
Figure 7. Photomicrograph of clinopyroxene and plagioclase feldspar phenocrysts in plain polarized light (PPL) and cross-polarized light (XPL) for sample MAC-17-04a. The field of view for both images is 9mm in width. Images taken under 50x magnification. Thin sections images courtesy of Dr. Daniel Heaton of Oregon State University.

Figure 8. Photomicrograph of clinopyroxene and plagioclase feldspar phenocrysts in plain polarized light (PPL) and cross-polarized light (XPL) for sample MAC-17-06. The field of view for both images is 9mm in width. Images taken under 50x magnification. Thin sections images courtesy of Dr. Daniel Heaton of Oregon State University.

MS-94-16 (Figure 9) has the most fine-grained groundmass within the thin sections. This

sample contains 5-7 phenocrysts, of which, one is a plagioclase phenocryst with an

embayed crystal that was possibly formed at an earlier time in the evolution of the

magma. The crystal appears to have been in the process of being resorbed into the

magma at the time of eruption. Both the phenocryst and margin of the smaller embayed

crystal appear to have a narrow reaction rim along which groundmass crystals have

aligned. The reaction rim with aligned iron oxide microlites is an indicator of

disequilibrium within the magma during crystallization. The section of Hunter Creek

Basalt from Neal Hot springs, MS-12-34 (see Appendix F), contains sparse phenocrysts of

plagioclase feldspar and clinopyroxene. Both the plagioclase phenocrysts and the

pyroxene phenocrysts range from moderately anhedral to euhedral. Two pyroxenes

show textures that are consistent with being actively resorbed. The texture of the

sample is aphanitic, and the micro-phenocryst content is between 1-2% at most. The

other most abundant materials in the thin sections are alteration products.

The icelandites of Alder Creek, BW-14-37A and BW-14-37B, are overall petrographically

similar to typical Hunter Creek Basalt lavas, having aphanitic texture containing

groundmass feldspar, magnetite, clinopyroxene, and interstitial glass, but they contain a

few relatively large, phenocrysts of tabular feldspars (Webb, 2017).

MC-106-16 consists of mostly microlites consisting of plagioclase lathes, opaque

minerals, and tiny crystals with higher interference colors that are likely pyroxenes,

Figure 9. Photomicrograph of clinopyroxene and plagioclase feldspar phenocrysts in plain polarized light (PPL) and cross-polarized light (XPL) for sample MAC-17-06. The field of view for both images is 9mm in width. Images taken under 50x magnification. Thin sections images courtesy of Dr. Daniel Heaton of Oregon State University.

although they are too small to properly analyze even under highest magnification. Only

four phenocrysts of simply twinned plagioclase can be observed in this sample. MC-98-

16 comes from an icelandite dike on the west flank of Ironside Mountain. Like MC-106-16, this sample has a texture with mostly microlites and with rare plagioclase phenocrysts. MC-15-16 is also aphyric under the petrographic microscope, even lacking sparse plagioclase phenocrysts that occur in MC-106-16 and MC-98-16. All three of these samples occur stratigraphically above the Dinner Creek Tuff unit 1, with MC-15-16 occurring within the Castle Rock caldera, and MC-98-16 and MC- 106-16 occurring at the Ironside Mountain caldera. The MC-101-16 sample comes from the western flank of Ironside Mountain. These samples were taken from aphyric icelandite lava intrusive into altered Dinner Creek Tuff unit 2.

WHOLE ROCK GEOCHEMISTRY

The 47 icelandite samples analyzed for this study range in composition from basaltic andesite to dacite in a total alkali silica (TAS) diagram (Figure 11). The most mafic sample, MAC-17-15 is a basaltic andesite with SiO_2 content of ~54% and the most felsic sample, BW-14-37A, is a dacite with ~63% SiO_2. The samples with the highest SiO_2 content are samples of the icelandite of Alder Creek located in the southern part of the Namorf quadrangle area in the Malheur River Gorge and the icelandites of the Castle Rock caldera area. The samples with the lowest total alkali content of this study are located near Castle Rock Caldera. These two samples have been classified as a pumice lapilli tuff by Cruz (2017). Published icelandite data shown in geochemical plots along with data of this study were compiled from Carlson and Hart (1987), Bailey (1989), Hooper and Swanson (1990), Hooper and Hawkesworth (1993), Hooper (2000), Hooper

et al. (2002) Lees (1994), Binger (1997), Reidel (1998), Reidel and Tolan (2013), Camp et al. (2003), Brueseke and Hart (2007), and Ferns et al., (2010).

Based on data of this study, the icelandites are divided into two primary groups based on the concentrations of Al_2O_3 and selected trace elements (Tables 1 and 2; Figures 10-13 and 17-23). Group 1 has lower concentrations of Al_2O_3 compared to the samples of Group 2. Group 1 is more enriched in the selected trace elements and REE while Group 2 is depleted in those same elements and REE. The division of the two main groups into secondary high and low TiO_2 groups is based on the large gaps between the samples within Groups 1 and 2. This can be seen in both the tables as well as the plot of TiO_2 versus SiO_2 (Figure 12).
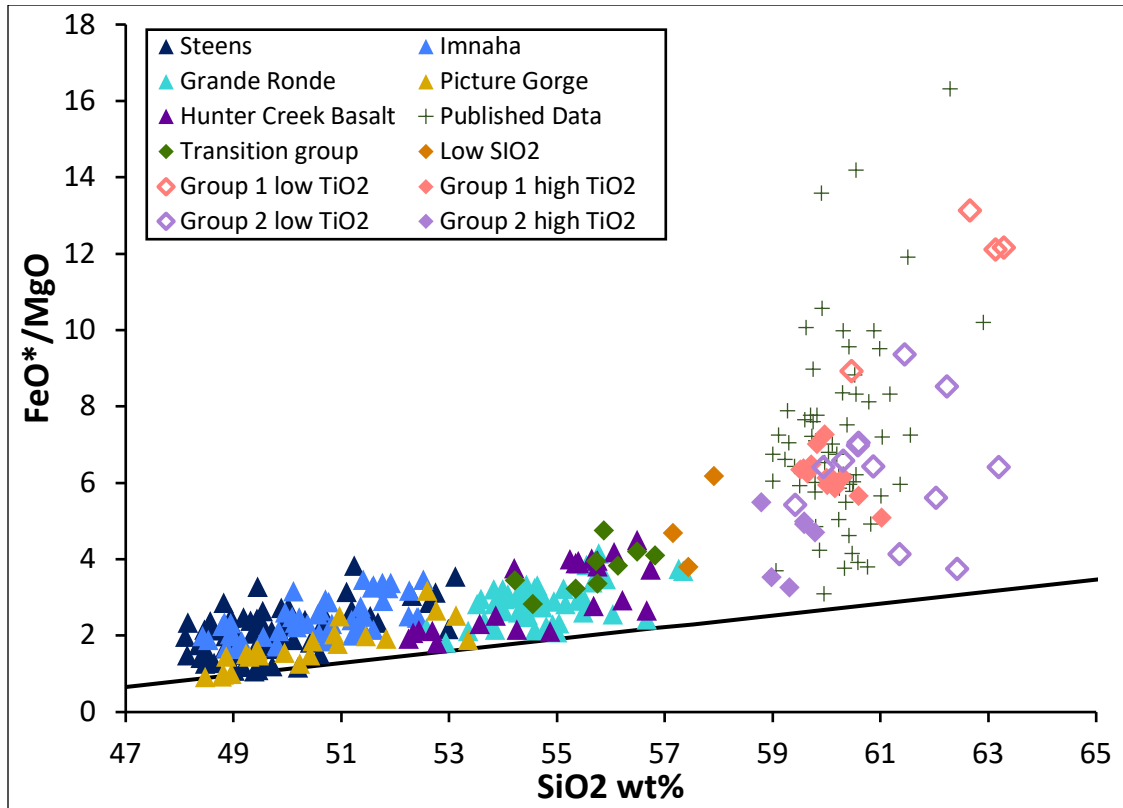
Figure 10. Plot of FeO*/MgO ratio versus silica content CRBG main phase members, Basalt of Malheur Gorge, Picture Gorge Basalt, Hunter Creek Basalt, icelandite groups of this study and previously published icelandites of CRBG from Carlson and Hart (1987), Bailey (1989), Hooper and Swanson (1990), Hooper and Hawkesworth (1993), Hooper (2000), Hooper et al. (2002), Lees (1994), Binger (1997), Reidel (1998), Reidel and Tolan (2013), Camp et al. (2003), Brueseke and Hart (2007), and Ferns et al., (2010).

Table 1. Ranges for major element concentrations in icelanditic rocks. Data for this table can be found in Appendix A.

Group	Transition	Low SiO_2	Group 1 low TiO_2	Group 1 High TiO_2	Group 2 low TiO_2	Group 2 High TiO_2
$SiO2$	54.22-56.81	57.15-57.91	60.46-63.28	59.51-61.02	59.42-63.20	58.79-59.78
TiO_2	2.14-2.41	1.84-2.39	1.19-1.56	1.95-2.01	1.08-1.50	1.77-1.95
Al_2O_3	13.32-14.54	13.41-16.09	12.87-13.54	13.13-13.56	14.08-15.45	14.96-15.47
FeO*	11.21-13.35	9.36-11.38	9.84-11.76	8.84-11.25	7.81-10.54	8.17-9.61
MnO	0.17-0.23	0.19-0.53	0.20-0.26	0.21-0.28	0.13-0.21	0.15-0.21
MgO	2.73-4.03	1.51-2.86	0.75-1.32	1.55-1.75	1.06-2.76	1.75-2.52
CaO	6.15-8.18	5.77-6.47	3.99-5.04	4.96-5.43	4.35-5.51	5.10-5.96
Na_2O	3.04-3.72	3.07-4.32	3.49-4.05	3.36-3.80	1.49-4.22	3.69-4.30
K_2O	1.34-1.99	1.40-2.40	2.65-3.31	2.27-2.91	1.45-2.70	1.72-2.23
P_2O_5	0.38-0.61	0.56-1.62	0.27-0.59	0.78-0.82	0.27-0.66	0.77-1.12

Table 2. Ranges for selected trace element and REE concentrations in icelanditic rocks. Data used for this table can be found in Appendix A.

Element (ppm)	Transition	Low SiO$_2$	Group 1 Low TiO$_2$	Group 1 High TiO$_2$	Group 2 Low TiO$_2$	Group 2 High TiO$_2$
Ba	559-942	691-1148	1091-1204	931 -1403	765-1039	710-1094
Th	3.99-6.31	4.2-6.8	8.3-9.8	7.9-8.3	3.0-5.4	3.2-4.0
Nb	11.7-15	13.0-16.5	20.1-23.4	17.2-18.0	8.5-11.3	11.0-13.9
Y	35.4-47	38.5-52.5	58.2-67.7	55.1-63.2	43.2-52.2	43.4-53.4
Hf	4.64-5.9	5.5-6.1	7.7-9.2	6.8-7.1	4.4-5.8	5.0-5.2
Ta	0.75-0.99	0.9-1.1	1.3-1.5	1.1-1.2	0.6-0.7	0.7-0.9
Rb	34.5-49.5	10.8-62.3	78.7-83.8	61.9-68.2	28.7-60.0	33.6-44.7
Zr	171.3-222.5	214.0-235.3	289.8-356.3	257.4-269.1	161.0-216.7	190.9-202.1
La	22.74-30.34	24.3-34.7	39.4-46.7	37.9-43.2	20.1-26.2	25.1-29.6
Ce	48.8-64.15	52.9-73.4	83.1-96.5	78.8-84.3	38.3-53.4	51.2-63.1
Pr	6.57-8.46	7.0-9.8	10.9-12.5	10.4-11.4	5.6-7.6	7.8-8.9
Nd	28.45-36.5	30.2-41.5	46.1-51.7	44.1-48.7	24.0-33.2	34.1-38.3
Sm	6.96-8.93	7.6 9.8	11.2-12.1	10.7-11.6	5.9-8.3	8.5-9.2
Eu	2.12-2.72	2.4 3.0	3.4-3.5	3.1-3.3	1.6-2.3	2.4-2.9
Gd	7.27-9.13	7.7 9.9	11.1-12.3	10.8-11.9	6.7-9.0	8.5-9.7
Tb	1.20-1.52	1.3 1.6	1.9-2.0	1.7-1.9	1.2-1.5	1.4-1.6
Dy	7.11-9.32	7.7 9.7	11.3-12.4	10.6-11.7	8.0-9.6	8.4-10.0
Ho	1.42-1.87	1.6 2.0	2.3-2.6	2.2-2.4	1.7-2.0	1.7-2.1
Er	3.75-5.05	4.2 5.3	6.3-7.0	5.8-6.6	4.5-5.6	4.5-5.5
Tm	0.53-0.72	0.6 0.8	0.9-1.0	0.8-0.9	0.7-0.8	0.6-0.8
Yb	3.19-4.43	3.6 4.7	5.7-6.2	5.0-5.6	4.2-5.1	3.9-4.9
Lu	0.5-0.72	0.6-0.8	0.9-1.0	0.8-0.9	0.7-0.8	0.6-0.8
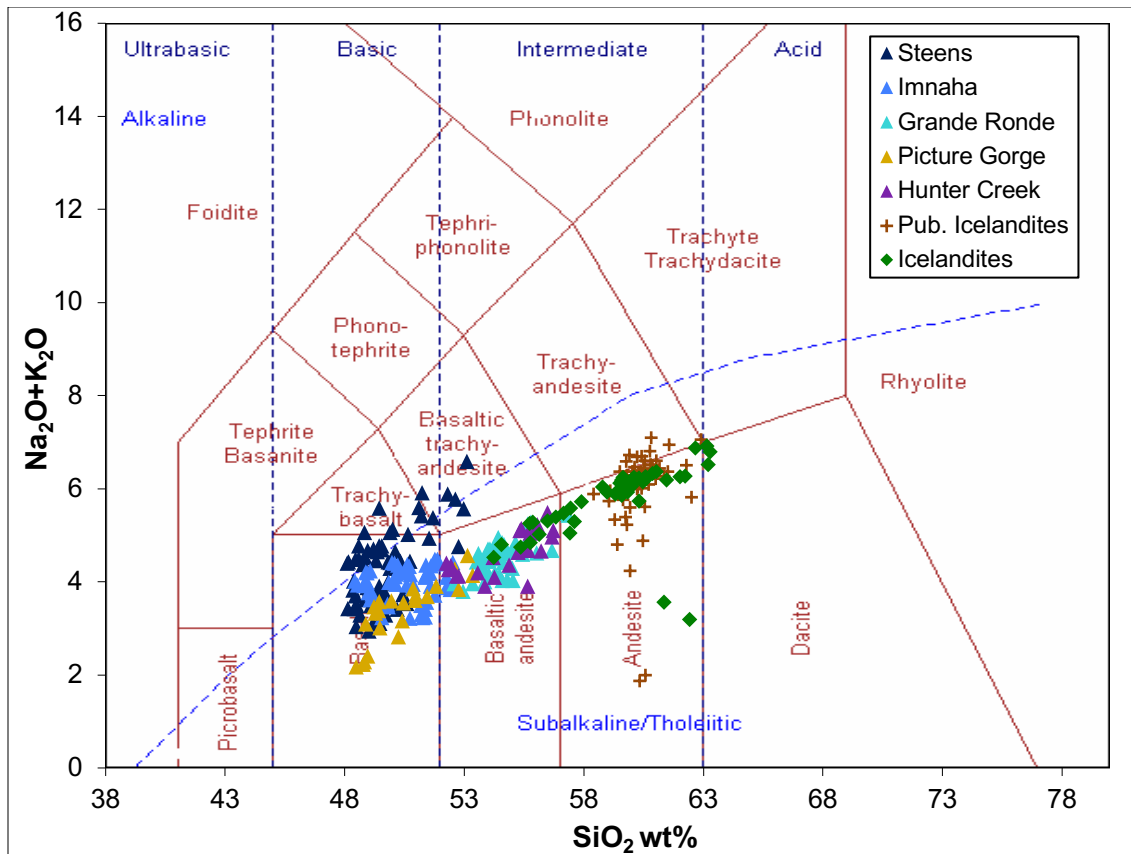
Figure 11. Total alkali versus silica content diagram (after Le Bas et al., 1986, Fig. 1) for main phase CRBG members, Picture Gorge Basalts, Basalt of Malheur Gorge, Hunter Creek Basalt, and icelandite units of this study. Analyses are from Carlson and Hart (1987), Bailey (1989), Hooper and Swanson (1990), Hooper and Hawkesworth (1993), Hooper (2000), Hooper et al. (2002) Lees (1994), Binger (1997), Reidel (1998), Reidel and Tolan (2013), Camp et al. (2003), Brueseke and Hart (2007), and Ferns et al., (2010). Data from this study used for plotting can be found in Appendix A.

With major elements, we see several differences between the icelandites of this study in

comparison to the CRBG main phase members and Hunter Creek Basalt. A significant

gap is observed in SiO_2 with all major element oxides, FeO*/MgO and Mg # continuing in

general the trend (increasing or decreasing) of main phase CRBG units (Figure 10 and

12-13). Only two samples above the lower limit for icelandite silica content have a TiO_2

content of over 2% wt, all remaining samples over 2% fall in the transition zone between

basaltic andesite and icelandite. The only sample with an Al_2O_3 content of more than 16%, is located in the Jump off Joe Mountain quadrangle.
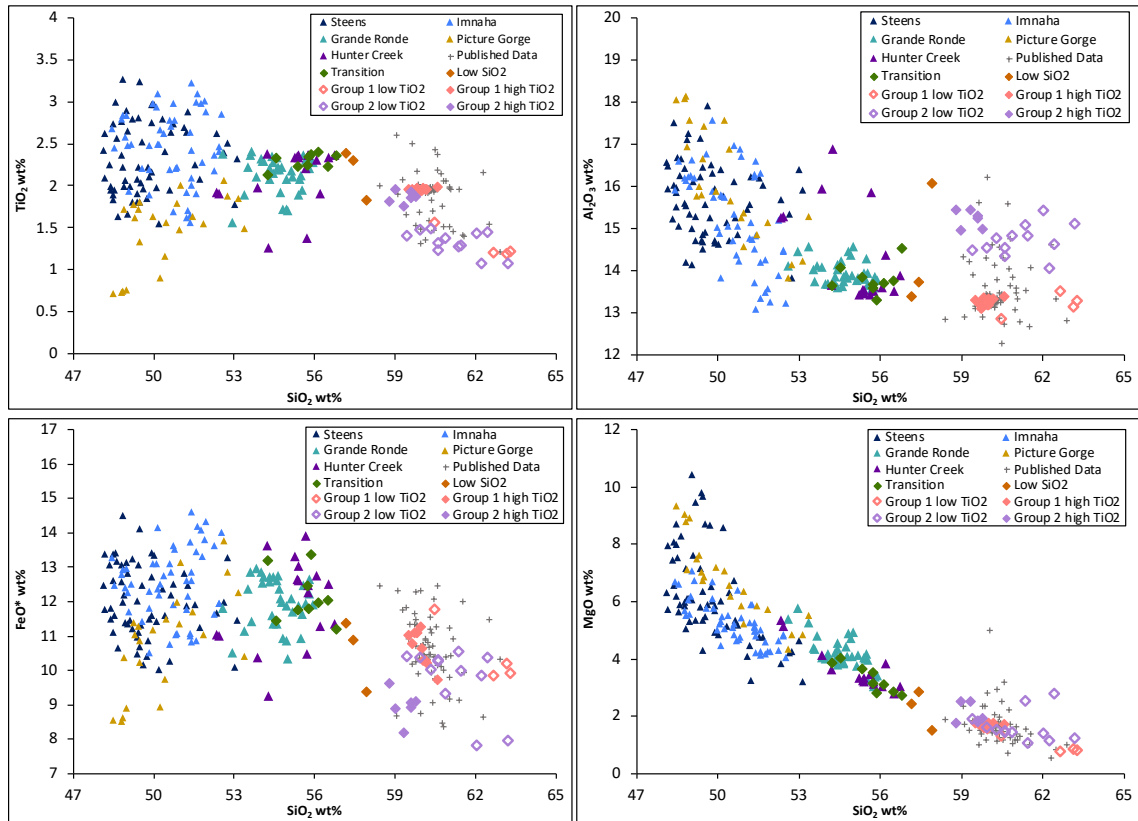
Figure 12. Major element x-y plots for TiO_2, Al_2O_3, FeO*, and MgO wt % vs. SiO_2 wt% for main phase CRBG members, Hunter Creek Basalt, Picture Gorge Basalt, and icelandites of this study. Data used for these plots can be found in Appendix A.

Variations in incompatible element concentrations and Al_2O_3 allow to separate icelandite samples with SiO_2 concentrations of 59 wt.% and higher into two main groups (Figures 12 and 16-23). Group 1 samples have distinctly higher concentrations of incompatible elements such as Nb, REE, and Th but lower Al_2O_3 than Group 2. Furthermore, based on a diagram of TiO_2 vs SiO_2 wt%, group 1 and 2 can be further subdivided. One can clearly see that both, group 1 and group 2, have both a high TiO_2

and low TiO₂ subgroup. Other samples of this study that are designated as transitional

and low SiO₂ plot closer to the Hunter Creek Basalt and to samples of CRBG.
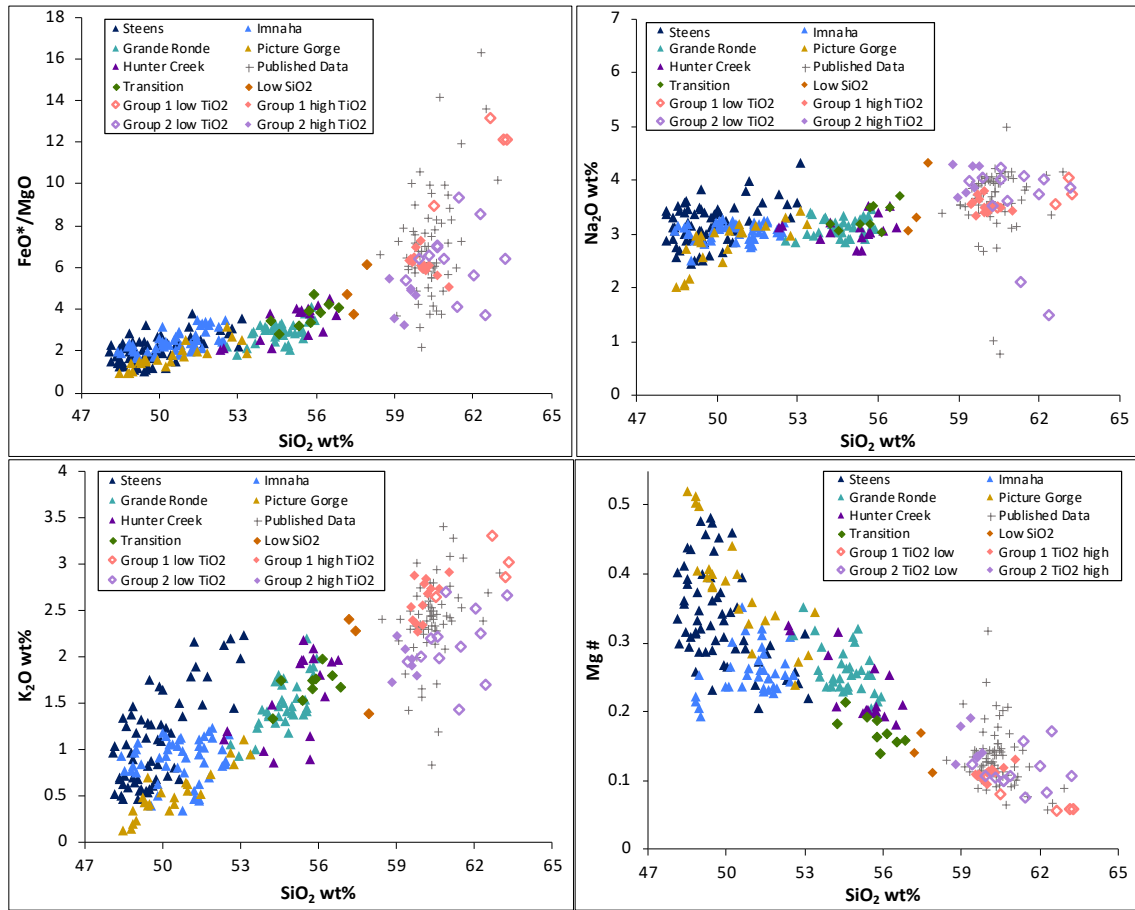
Figure 13. Major element x-y plots for Na₂O wt %, K₂O wt %, FeO*/MgO, and Mg # vs. SiO₂ wt% for main phase CRBG members, Hunter Creek Basalt, Picture Gorge Basalt, and icelandites of this study. Data used for these plots can be found in Appendix A.

The icelandites from this study share many of the trace and rare earth element

geochemical characteristics of the main phase CRB members at a slightly more enriched

level (Figure 14-15). However, the averages of the icelandites from this study and the

Hunter Creek Basalt differ from the main phase members of the CRBG in Sr and Ti, that

indicate depletion relative to neighboring elements. Values for both of these elements,

especially the concentration of Ti, fall closer to that of the Picture Gorge basalt. The Ba-

31

Th-U trough for Hunter Creek Basalt, Picture Gorge Basalt and samples of this study are more pronounced than the remaining CRB main phase and published icelandite averages. In contrast the magnitude of the Nb-Ta trough for Grande Ronde, Hunter Creek, and the icelandites is much more pronounced than that of the Steens, Imnaha and Picture Gorge.

The C1 chondrite normalized (McDonough and Sun, 1995) REE diagram (Figure 15) illustrates the enrichment level differences of the icelandites and lavas of the Hunter Creek Basalt relative to other CRBG members. The trend of the icelandites follows that of the Imnaha, Grande Ronde, and Hunter Creek Basalt from La through Nd. From Sm to Gd the Grand Ronde Basalt, Hunter Creek Basalt, and icelandites break away from the enrichment pattern of the Imnaha Basalt. After Gd the Hunter Creek Basalt and the icelandites begin to diverge from the Grande Ronde Basalt and the REE enrichment pattern becomes much flatter, resembling that of the Picture Gorge Basalt.
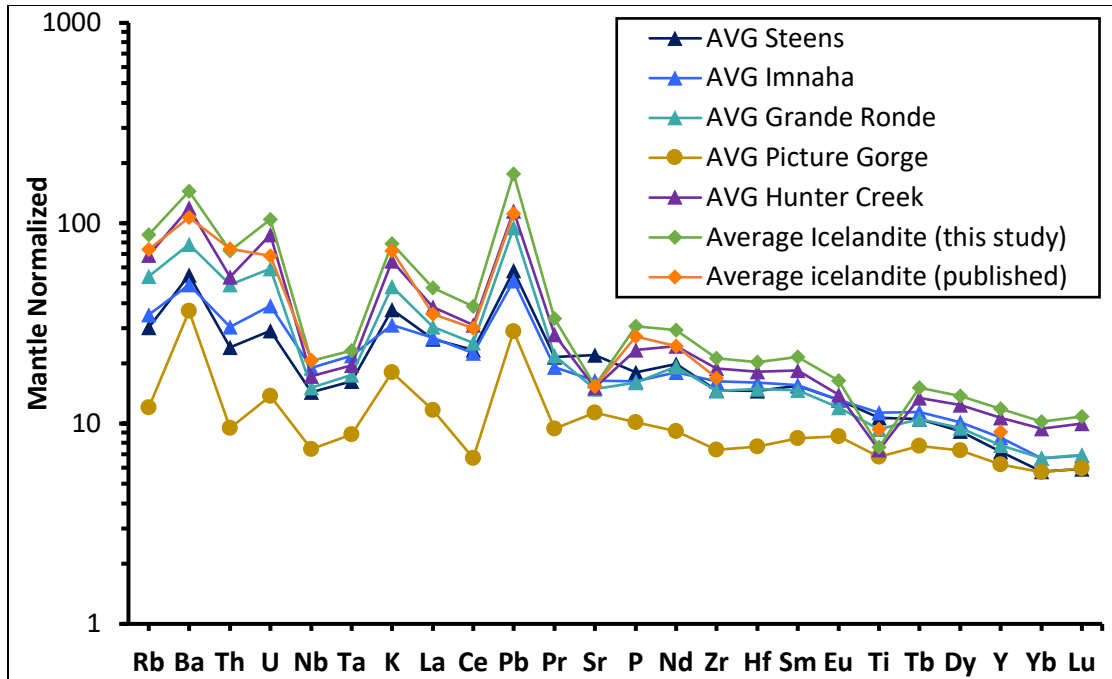
Figure 14. Primitive mantle normalized (Sun and McDonough, 1989) trace element diagram for averages of main phase CRBG members, Hunter Creek Basalt, published icelandites, and icelandites of this study. These values can be found in Appendix A.
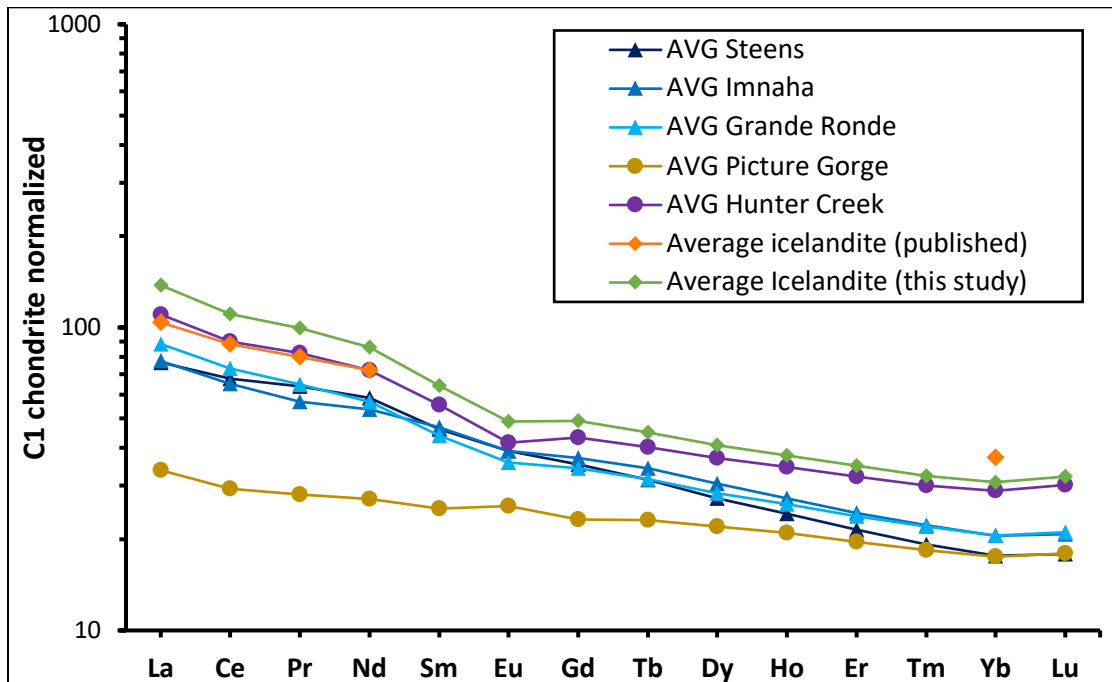
Figure 15. C1 chondrite (McDonough and Sun, 1995) normalized REE diagram for averages of main phase CRBG members, Hunter Creek Basalt, published icelandites, and icelandites of this study. These values can be found in Appendix A.

There are slight variations in concentration for several trace and REE between the different icelandite groups (Figure 16). The spider diagram for the averaged icelandite groups shows some of the variations in trace element concentrations that distinguish group 1 (trace element enriched) and group 2 (trace element depleted). In rare earth element (REE) concentrations (Figure 17), the TiO_2 subgroups have a similar pattern to the enrichment level until Dy, after which the low TiO_2 subgroups become enriched in the least incompatible REE and the high TiO_2 subgroups become depleted in the least incompatible REE. The Ba-Th-U trough is much steeper for the group 2 icelandites than it is for the group 1 samples.
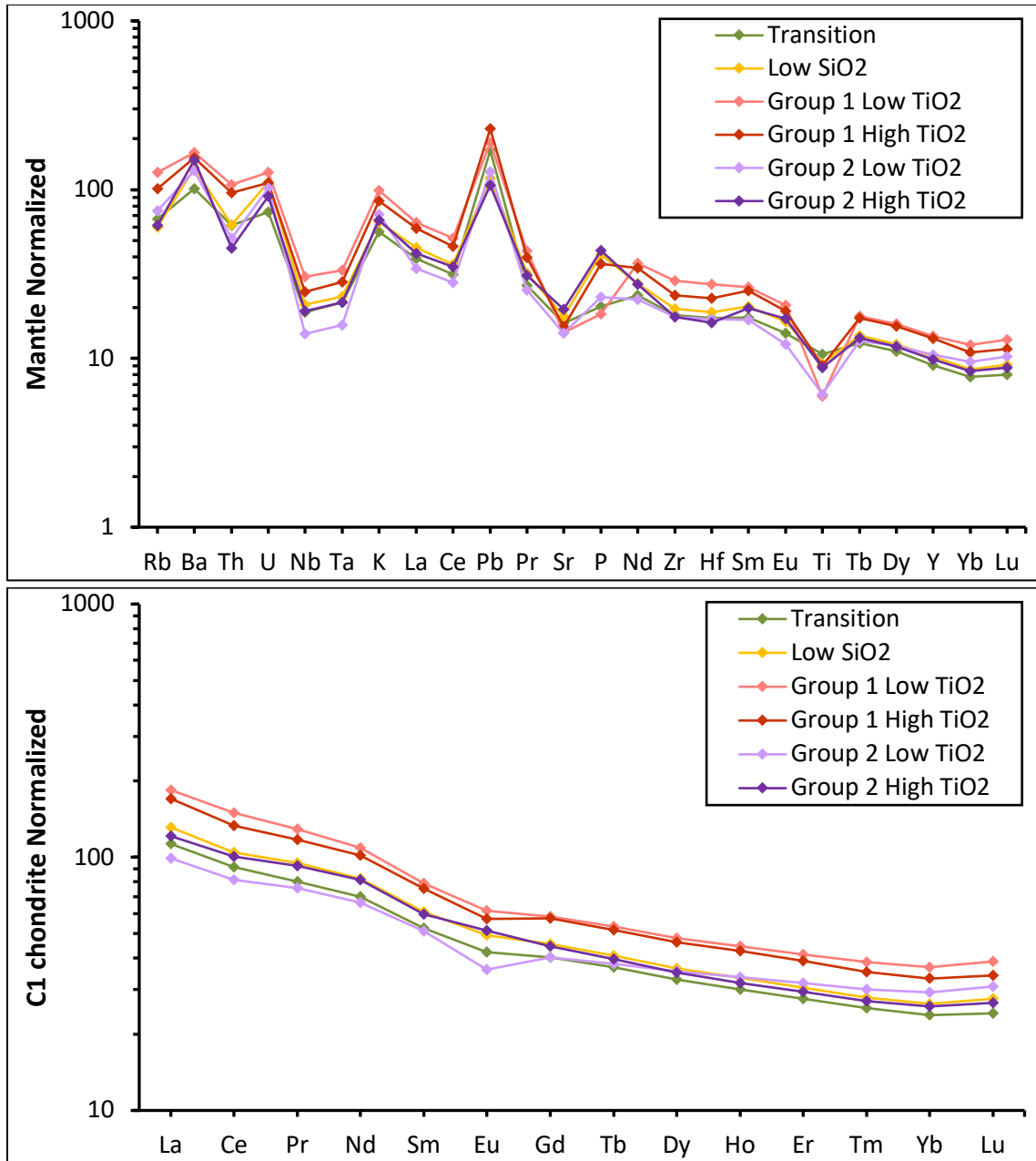
Figure 16. Primitive mantle normalized (Sun and McDonough, 1989) trace element diagram and C1 chondrite normalized (McDonough and Sun, 1995) REE diagram for average values of each icelandite group. These values can be found in Appendix A.

In all the key identifying trace and REE of the icelandites, the trend of higher enrichment

in group 1 compared to that of group 2 can be observed. These key trace elements

(including REE) are: Nb, Ta, Th, Zr, Rb, Y, La, Sm, Pr, Nd, Gd, Er, Tm, Yb, and Lu. It can

also be noted that the high TiO$_2$ subgroup for the most part corresponds to a lower silica content. The icelandites can have very similar concentrations in certain trace elements while also having very different concentrations in other trace elements (Figure 14-17). Rubidium and barium are two good examples of the similar elemental trends between the two groups of icelandites (Figure 17). The plot of Rb versus SiO$_2$ illustrates the clustering that occurs within the main icelandite groups and the TiO$_2$ subgroups. The plots for Rb and Ba versus SiO$_2$ also highlight the wide range in elemental concentration that can be found both in the Grande Ronde Basalt and Hunter Creek Basalt as well as the icelandites. Ba is one of the few trace elements that contains overlapping values between groups 1 and 2.

There is a decrease in concentration with Y, Nb, Ta, (also for most REE elements, see Figures 17-23) as silica increases in group 2 icelandites while the group 1 icelandites having a positive trend of increasing enrichment with increasing silica content.

Regarding Th, we have 2 strong linear trends starting with two separate clusters of the Hunter Creek basalt and going through data of the two groups of icelandites (Figure 19). The lower concentration group also tracks backward to the Th concentrations of the Picture Gorge basalts. The more enriched group 1 icelandites can be linearly traced back to the other main phase CRBG members.
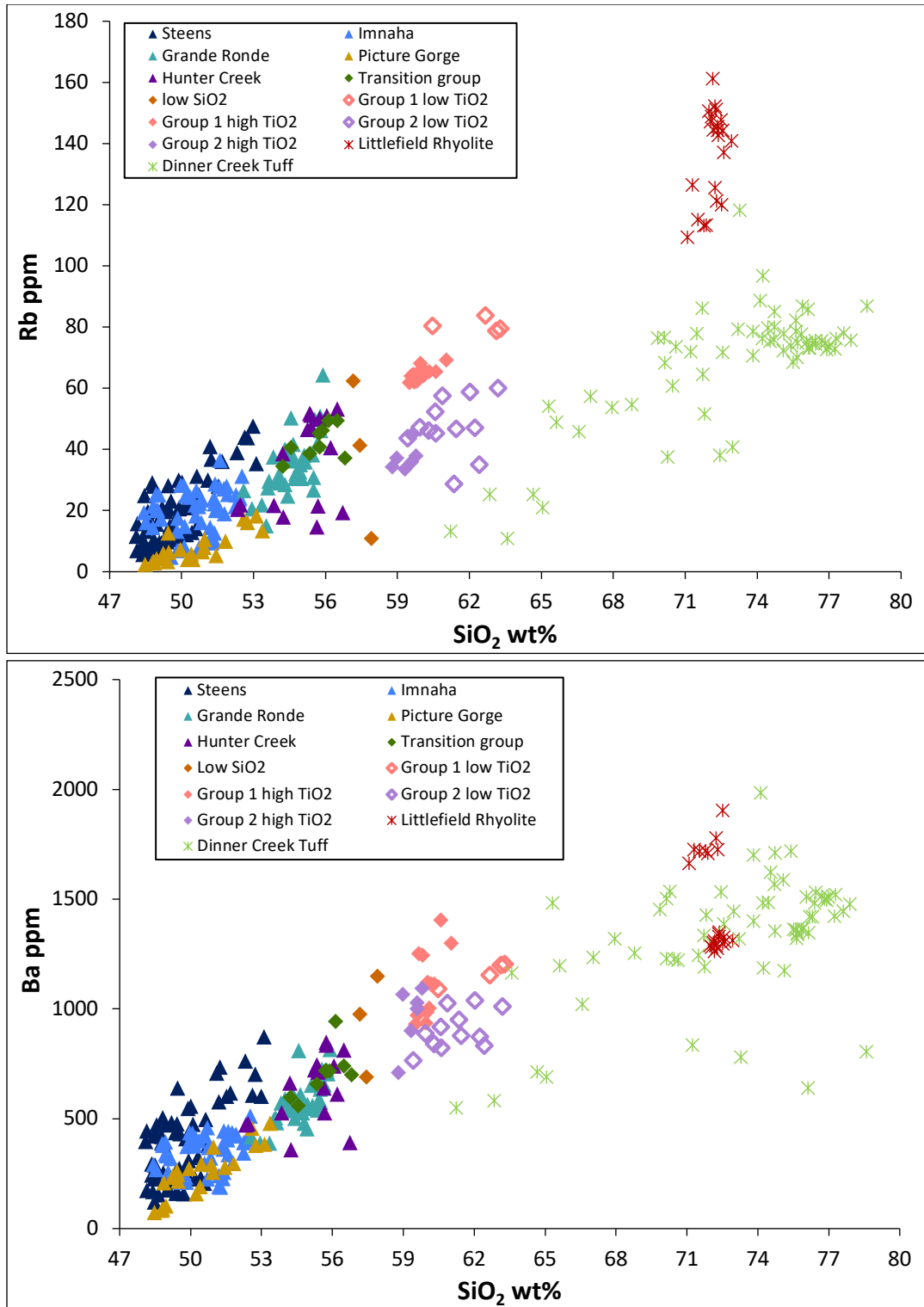
Figure 17. Major-trace element x-y plot Rb and Ba vs. SiO₂ wt% for main phase CRBG members, Hunter Creek Basalt, Picture Gorge Basalt, Dinner Creek Tuff, Littlefield Rhyolite and icelandites of this study. Data used for plots can be found in Appendix A. DIT samples from 60-65% SiO2 are Laser ablation ICP-MS for mafic globules in the Dinner Creek Tuff,

37
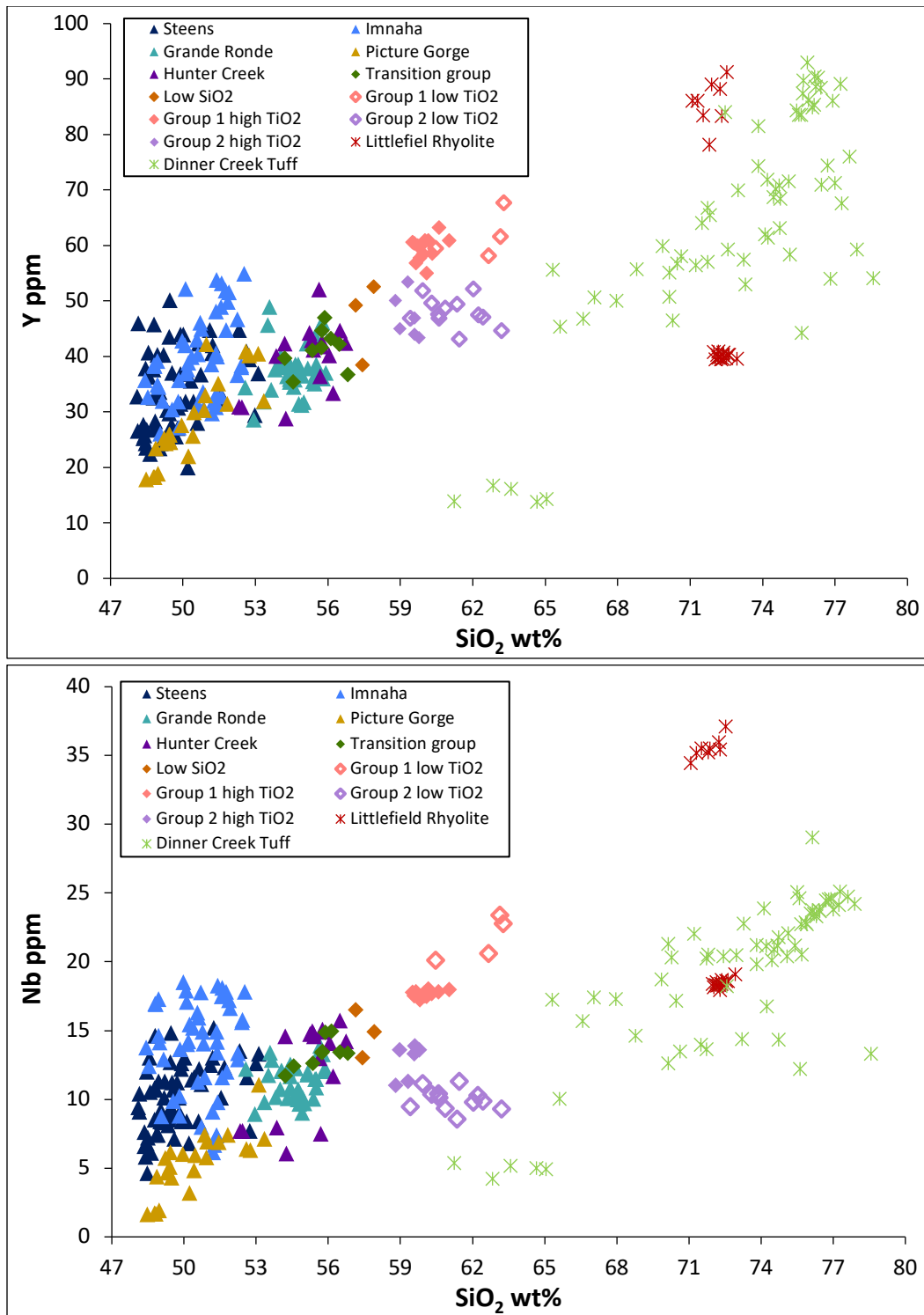
Figure 18. Major-trace element x-y plot for Y and Nb vs. SiO$_2$ wt% for main phase CRBG members, Hunter Creek Basalt, Picture Gorge Basalt, Dinner Creek Tuff, Littlefield Rhyolite, and icelandites of this study. Data used for plots can be found in Appendix A. DIT samples from 60-65% SiO2 are Laser ablation ICP-MS for mafic globules in the Dinner Creek Tuff,
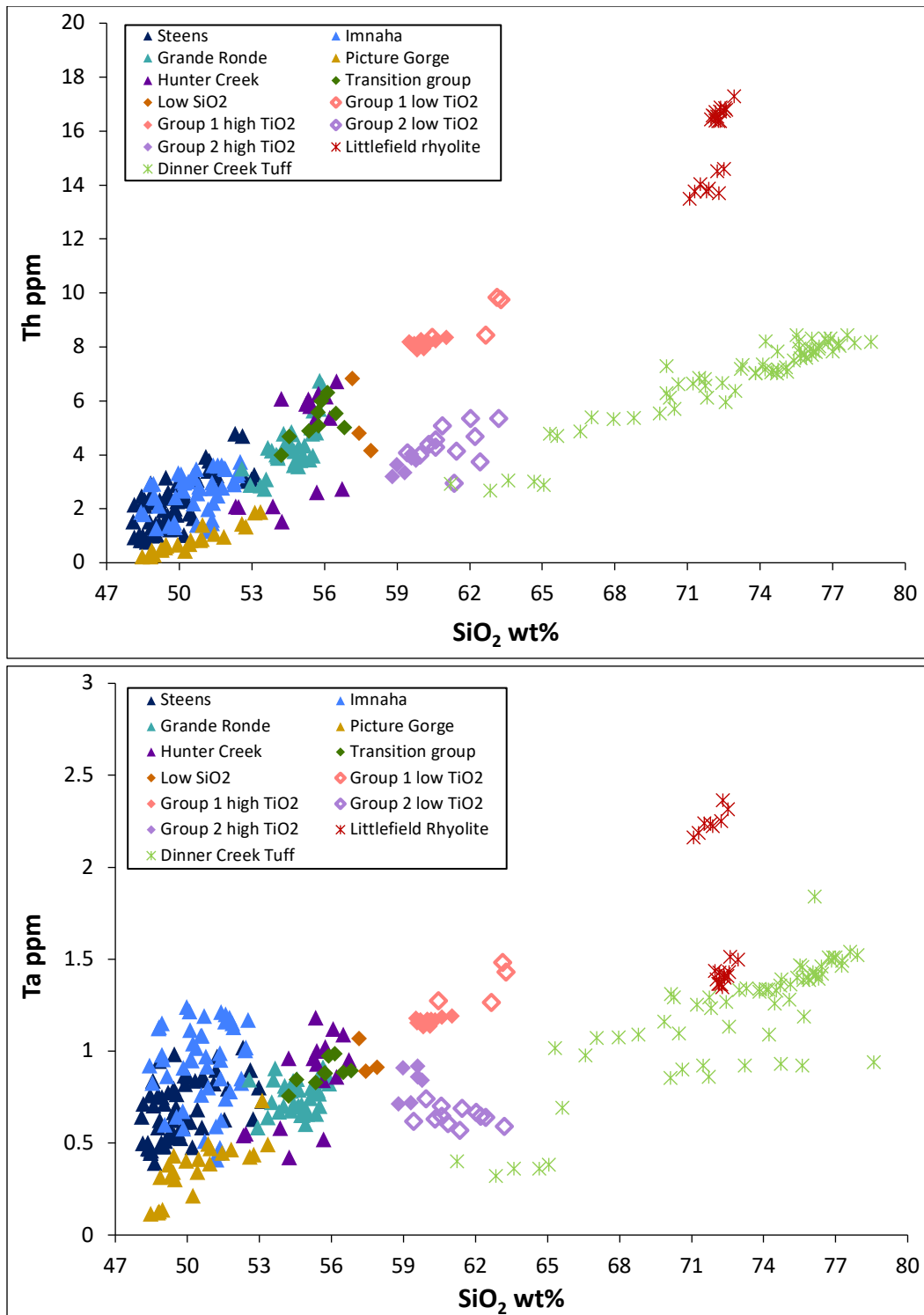
Figure 19. Major-trace element x-y plots for Th and Ta vs. SiO₂ wt% for main phase CRBG members, Hunter Creek Basalt, Picture Gorge Basalt, Dinner Creek Tuff, Littlefield Rhyolite and icelandites of this study. Data used for these plots can be found in Appendix A. DIT samples from 60-65% SiO₂ are Laser ablation ICP-MS for mafic globules in the Dinner Creek Tuff,

The enrichment trend from the most incompatible to the least incompatible of the REE in the icelandites also displays the differences between the two main icelandite groups (Figures 20-23). The group 2 icelandites have enrichment that changes with the compatibility of the REE, while the enrichment of REE in the group 1 icelandites remains relatively unchanged. La, the first of the REE plotted has a negative trend of enrichment in group 2 and in Lu, final REE plotted the trend has changed to a positive trend of enrichment. The REE plots between these two elements show the change in the trend of enrichment from negative to positive for group 2 icelandites.
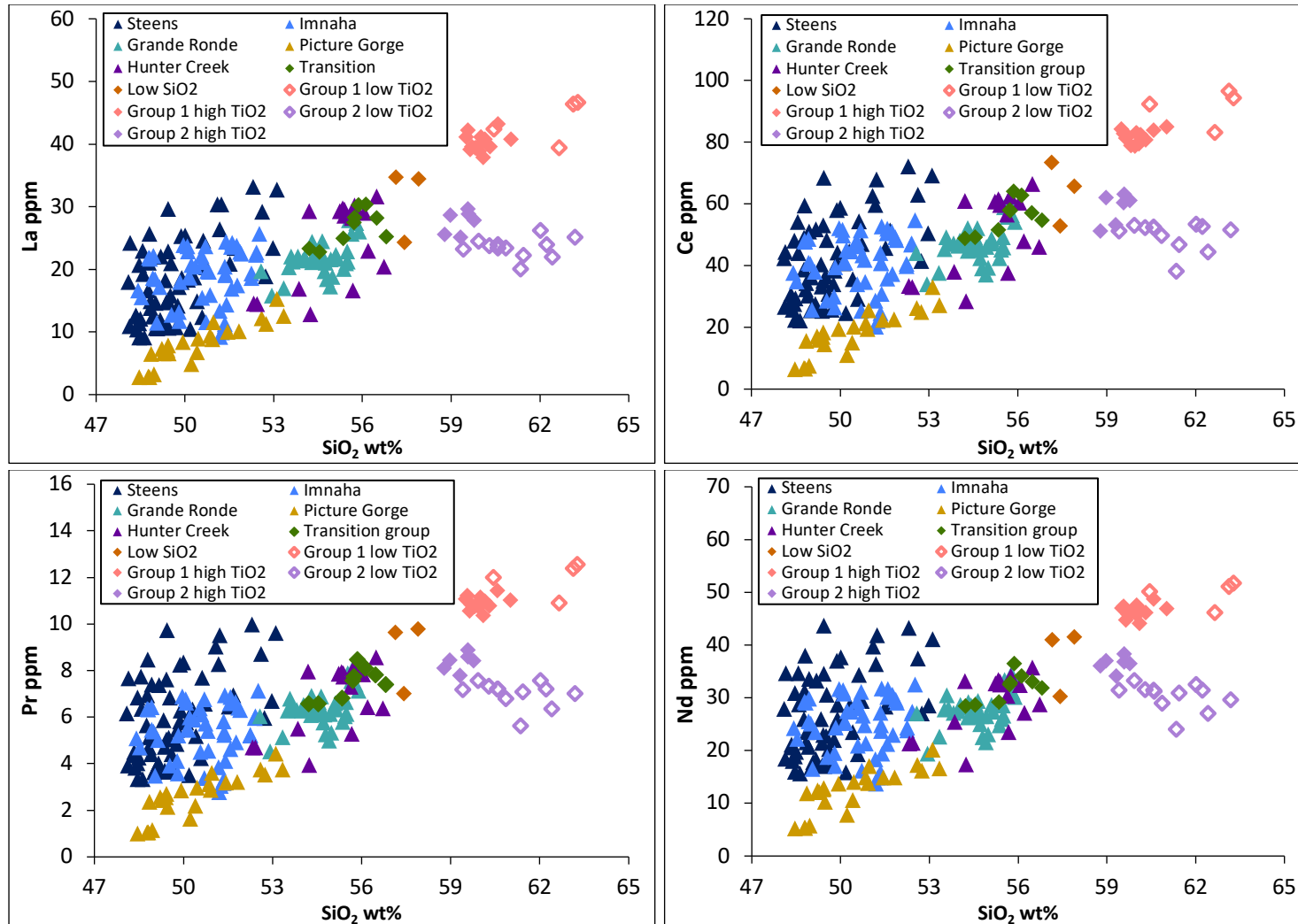
Figure 20. Plots of rare earth elements (REE) vs. SiO₂ wt% for main phase CRBG members, Hunter Creek Basalt, Picture Gorge Basalt, and icelandites of this study. Data used for these plots can be found in Appendix A.
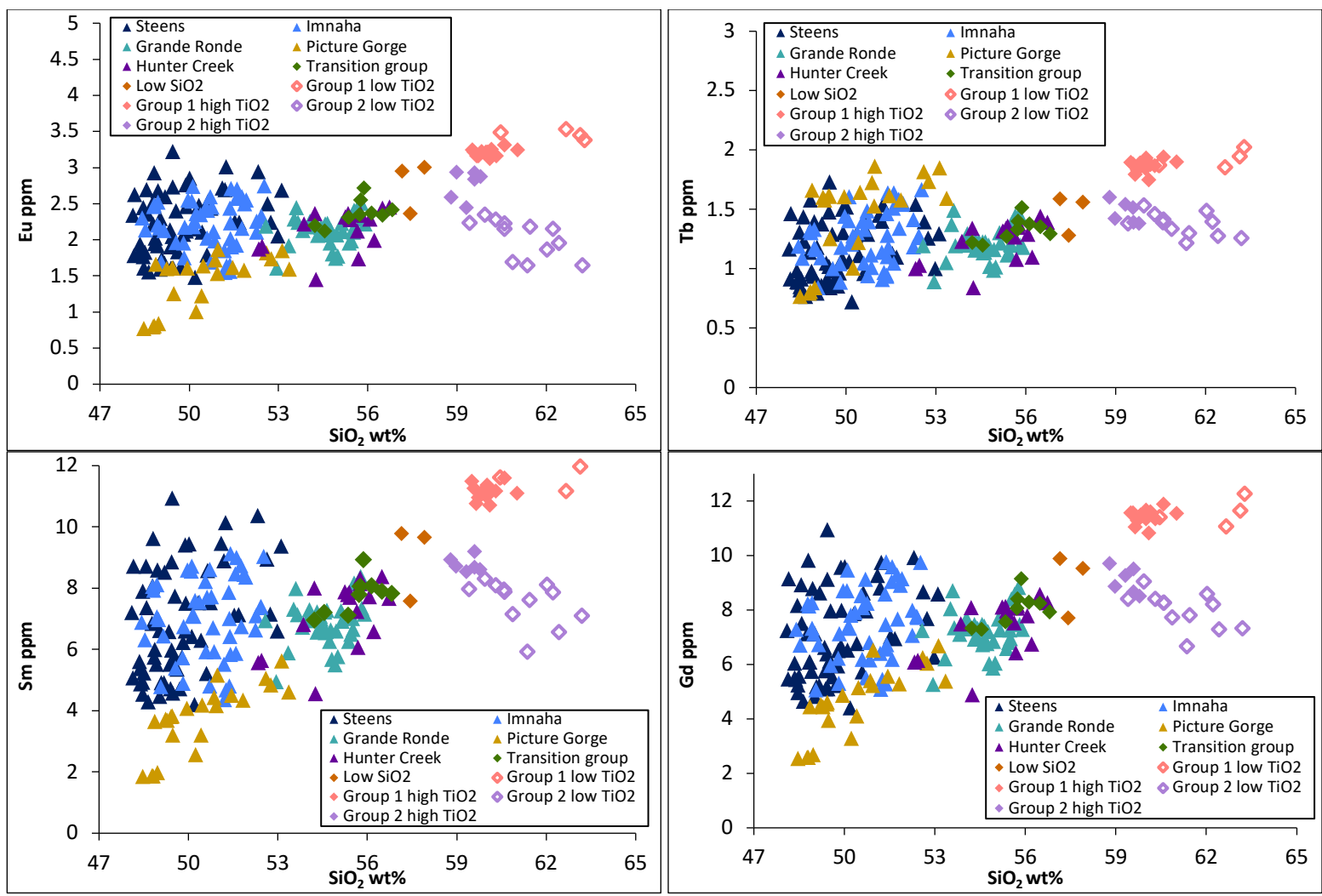
Figure 21. Plots of rare earth elements (REE) vs. SiO_2 wt% for main phase CRBG members, Hunter Creek Basalt, Picture Gorge Basalt, and icelandites of this study. Data used for these plots can be found in Appendix A.
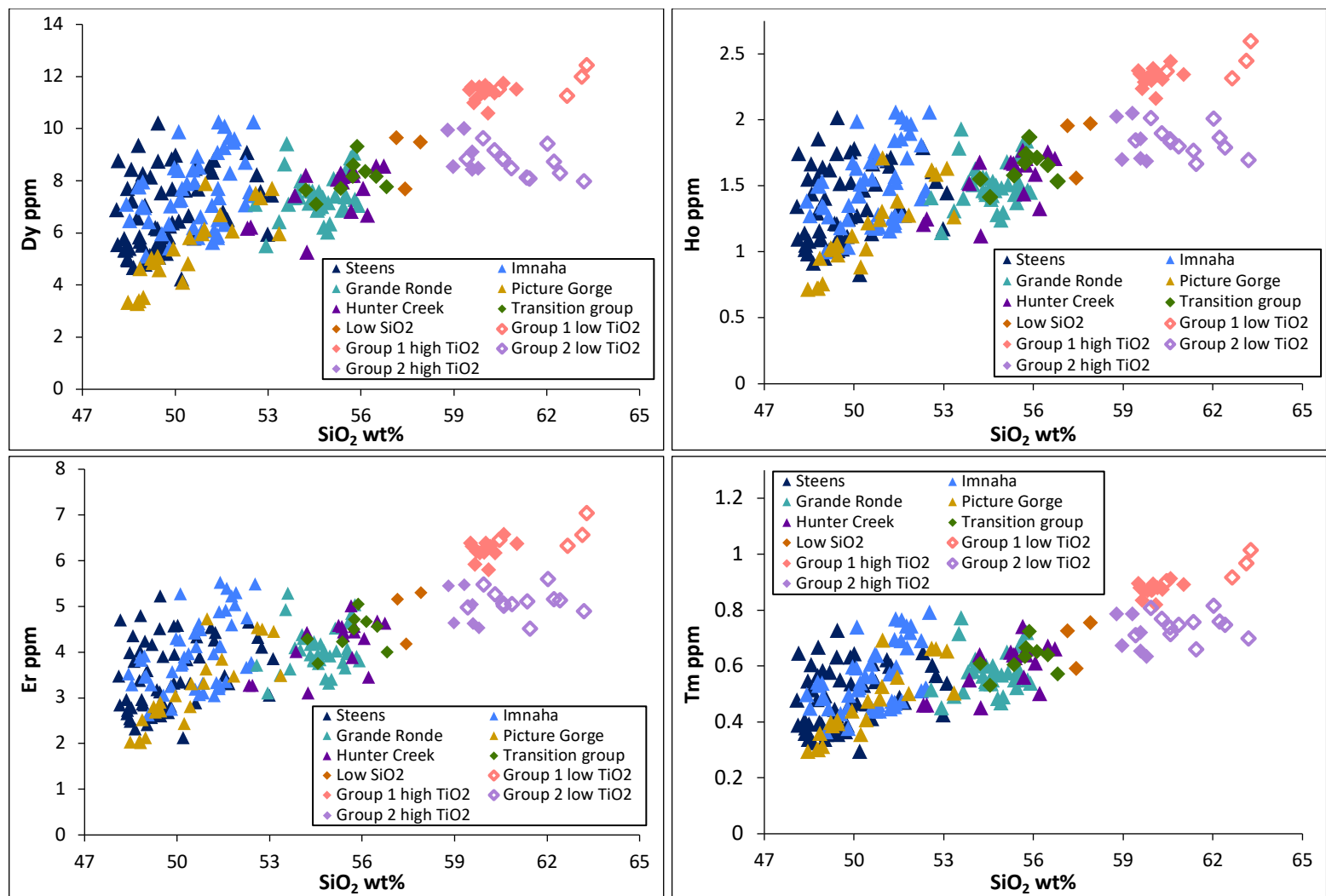
Figure 22. Plots of rare earth elements (REE) vs. SiO_2 wt% for main phase CRBG members, Hunter Creek Basalt, Picture Gorge Basalt, and icelandites of this study. Data used for these plots can be found in Appendix A.
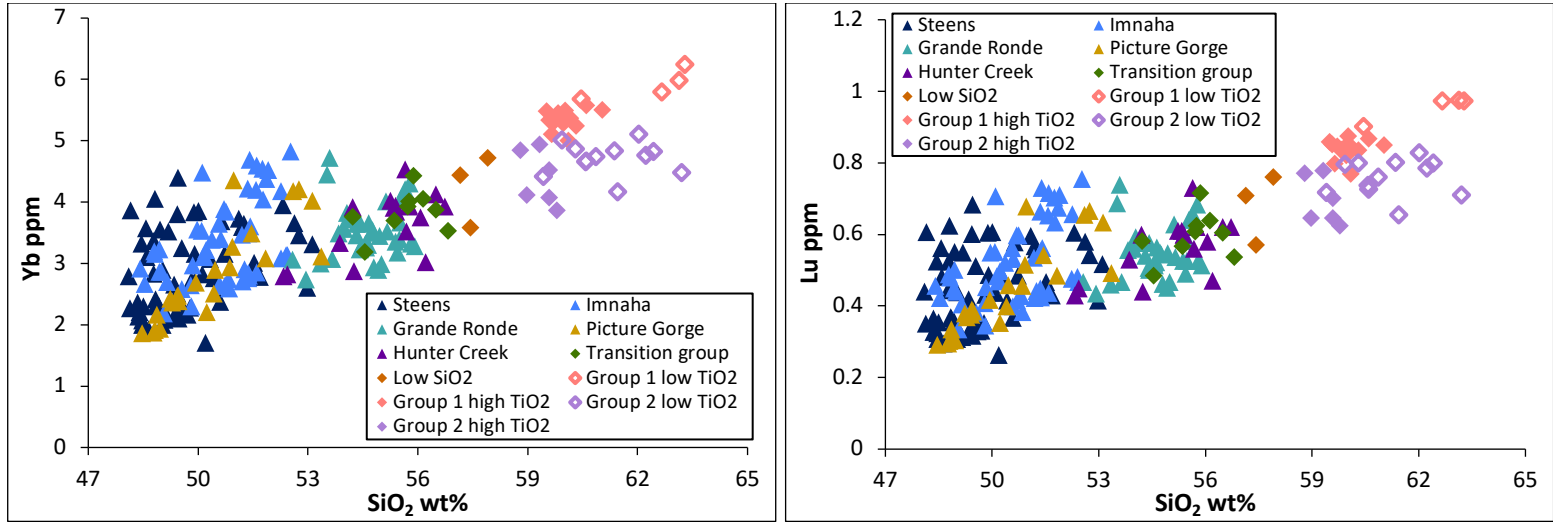
Figure 23. Plots of rare earth elements (REE) vs. SiO_2 wt% for main phase CRBG members, Hunter Creek Basalt, Picture Gorge Basalt, and icelandites of this study. Data used for these plots can be found in Appendix A.

COMPOSITION OF PHENOCRYSTIC MINERALS

Ternary diagrams with SEM data of plagioclase feldspars and clinopyroxenes can be

found in figure 24 and 25. The values that were chosen for plotting in the ternary

diagrams for both the plagioclase feldspar and the clinopyroxene were the closest value

to 100% for each phenocryst. Any values that were below 90% were discarded, the bulk

of plagioclase feldspar compositions from SEM analysis fall into the andesine category,

within a few exceptions that are categorized as labradorite. Overall, plagioclase

compositions show a slight decrease in orthoclase concentration as the ratio of

anorthite to albite increases.
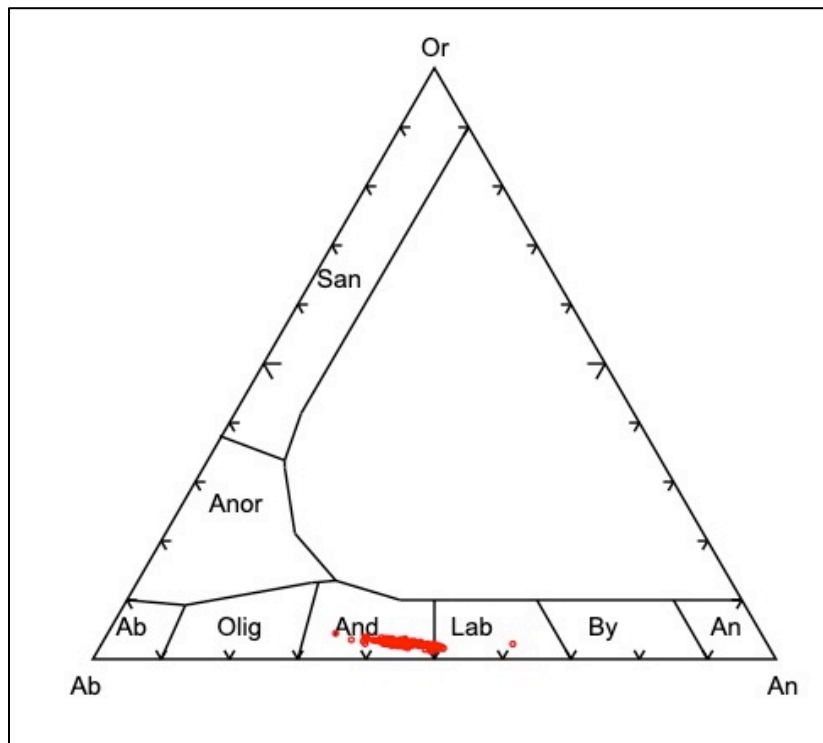
Figure 24. Ternary diagram of representative single point compositions for plagioclase feldspar phenocrysts determined by SEM-EDS analysis. Data used for plot can be found in Appendix C.

The SEM data acquired for clinopyroxene indicate a wide range when plotted on the

enstatite (En)-ferrosillite (Fs)-wollastonite (Wo) ternary diagram (Fig. 25). The analyses

of the clinopyroxene phenocrysts all fall within the augite and pigeonite range. The

samples show some variation in the ratios of enstatite to ferrosillite, but for the majority

of the samples they have roughly even concentrations of the two mineral endmembers.
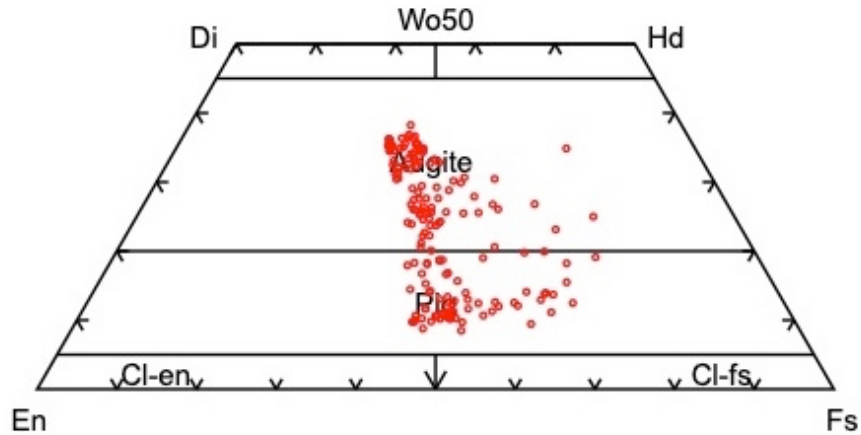
Figure 25. Ternary diagram of the representative single point compositions of clinopyroxene phenocrysts determined by SEM-EDS analysis. Data used for plot can be found in Appendix C.

Several of the phenocrysts selected for analysis turned out to be apatite (Figure 26).

Crystal sizes among these analyzed phenocrystic apatite ranged from 71 to 102 µm.
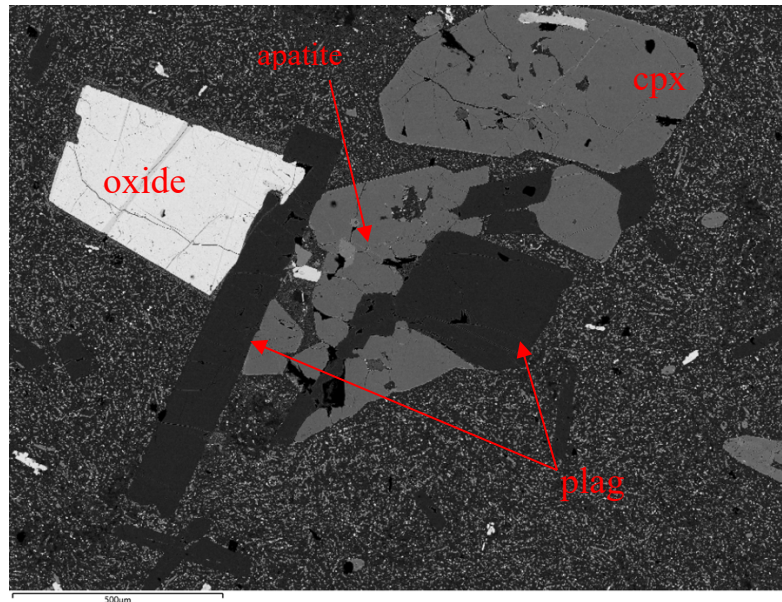
Figure 26. Electron image of site 4 containing apatite microphenocryst within phenocryst of clinopyroxene from sample MAC-17-16.

Discussion

Geochemical Modeling

I evaluated the generation of the two icelandite compositional groups with two

petrogenetic modeling approaches. The first one evaluated the evolution of the

icelandites via fractional crystallization from a basaltic/basaltic andesitic parent. The

second tested the scenario of a mixing origin of icelandite magma.

Table 3. Mineral proportions used for icelandite groups in fractional crystallization model.

Mineral phase	Plagioclase (An70Ab30)	Olivine (Fo76Fa24)	Clinopyroxene (Di9Hed9)	Ti-Fe oxide (Mag50Il50)	Bulk Mineral
Group 1	0.49	0.1	0.23	0.18	1.00
Group 2	0.61	0.12	0.14	0.13	1.00

Table 4. Estimated mineral chemistry for major rock forming minerals of mid-Miocene icelandites and calculated bulk mineral used for crystalization models of group 1 and 2 icelandites.

Mineral phase	Plagioclase (An70Ab30)	Olivine (Fo76Fa24)	Clinopyroxene (Di9Hed9)	Ti-Fe oxide (Mag50Il50)	Bulk Mineral Group 1	Bulk Mineral Group 2
SiO2	50.83	39.03	52.15	0.19	40.84	43.01
TiO2		0.05	0.14	24.45	4.44	3.20
Al2O3	31.39		1.79	0.38	15.86	19.44
FeO*	0.07	18.22	5.81	70.59	15.90	12.22
MnO		0.23	0.05	0.18	0.07	0.06
MgO	0.01	42.91	14.43	0.28	7.66	7.21
CaO	13.75	0.02	24.15	0.33	12.35	11.81
Na2O	3.37		0.38		1.74	2.11
K2O	0.08				0.04	0.05
P2O5					0.00	0.00
Total	99.50	100.45	98.89	96.39	98.89	99.12

The bulk mineral composition and modes used for the geochemical models were based

on the composition and mineral abundances in andesites and tholeiitic basalts of the

CRBG (e.g. the ferro-andesites of the Grande Ronde Basalt studied by Lambert et al.,

1995) and known mineral assemblages of other icelandites including Thingmuli

(Carmichael, 1964), North Shore Volcanic Group (Green and Fitz, 1993 and Vervoort and

Green, 1997), and Heiðarsporður Ridge (Mancini et al., 2015 and Jónasson, 2005).

Phenocrystic phases that were found to be common to all the known icelandite mineral

assemblages were plagioclase feldspar, clinopyroxene, iron rich olivine, and Fe-Ti oxides.

In addition, the ferro-andesites of Lambert et al. (1995) also contained apatite, and

chlorophaeite, an alteration product of olivine. Apatite as accessory minerals was not

included in the geochemical models as it is likely to have begun crystallizing very late in

the solidification process at crystallization amounts of >60% which is at the upper end of

the modeling range.

I chose potential parents from the CRBG that are compositionally closest to the

icelandites, and these are Grande Ronde Basalt samples (including those from the

Hunter Creek Basalt, Figure 10-15). Furthermore, the selection of which two Grande

Ronde/Hunter Creek Basalt samples are taken as potential parent magmas for Group 1

and Group 2 icelandites, respectively, is based on which samples are deemed suitable

based on trendlines for incompatibly behaving trace elements (e.g., Th vs SiO2, Figure

19). From the clusters of suitable samples, averages for a slightly enriched Group 1

parent and a slightly depleted Group 2 parent were calculated (see Appendix).

Detailed results of the Rayleigh fractional crystallization model can be found in appendix

D. The Rayleigh model results show that the two groups of icelandites are unlikely to

have formed by fractional crystallization alone. The formation of the group 1 icelandites

by fractional crystallization is not possible (Figure 29, 31) in terms of major elemental

constraints but is possible in context of incompatible trace elements including REE. The

group 2 icelandites yielded similar results in with the formation of group 2 (Figure 30, 32) being possible via fractional crystallization for incompatible trace elements but is less feasible for major elements.
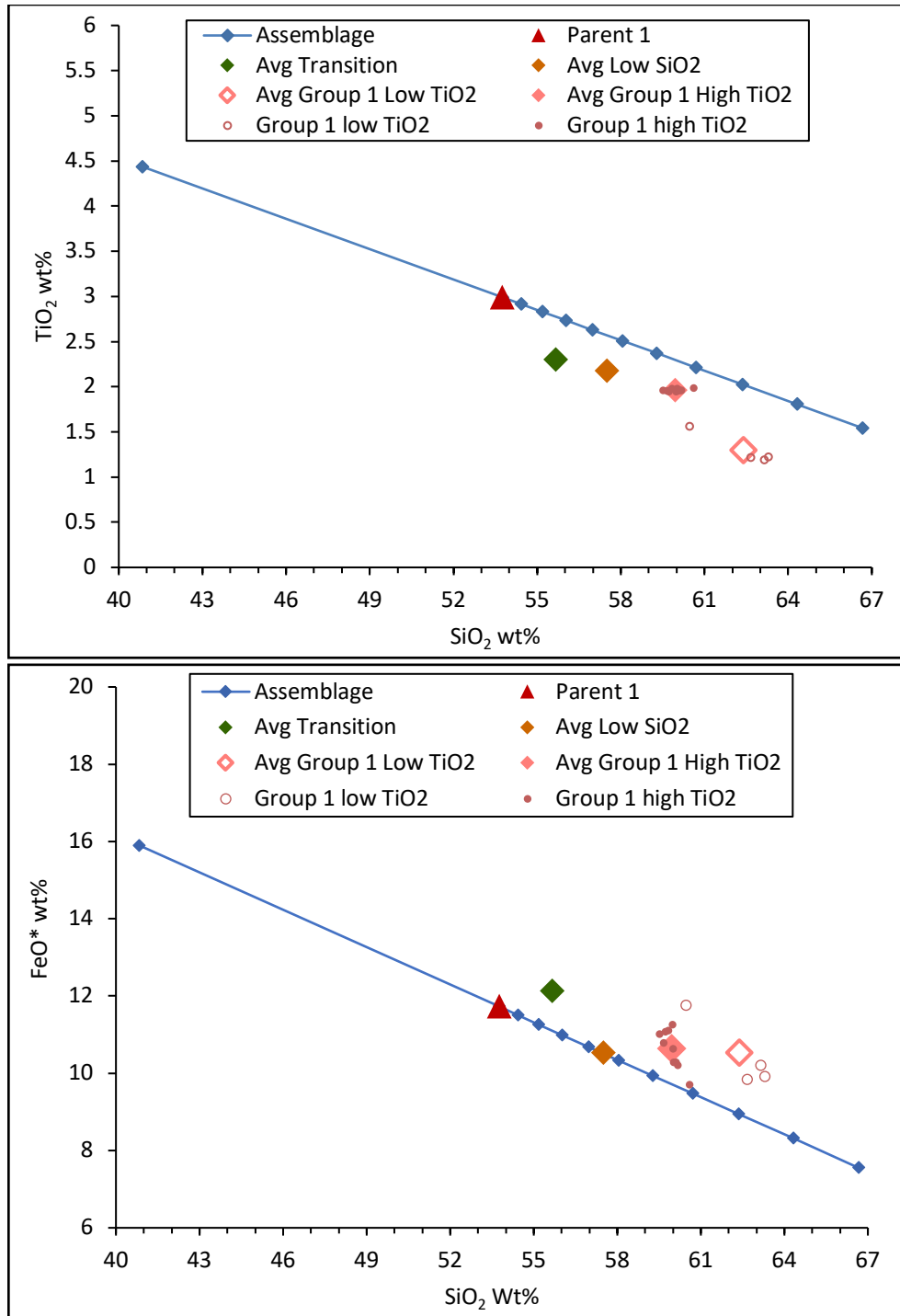
Figure 27. Variation diagrams of Group 1 icelandites and mass balance modeling results for the two important major elements, Fe and Ti. The blue line is the calculated crystallization path using the calculated assemblage beginning at 42% SiO_2 (blue diamond) from the mafic parent magma (red triangle), each tick mark (blue diamonds) along the crystallization line represents crystallization increments of 5%. Labeled points include the samples of group 1 as well as averages of the transition, low SiO_2, and group 1 icelandites. Detailed results of the mass balance model can be found in appendix D.
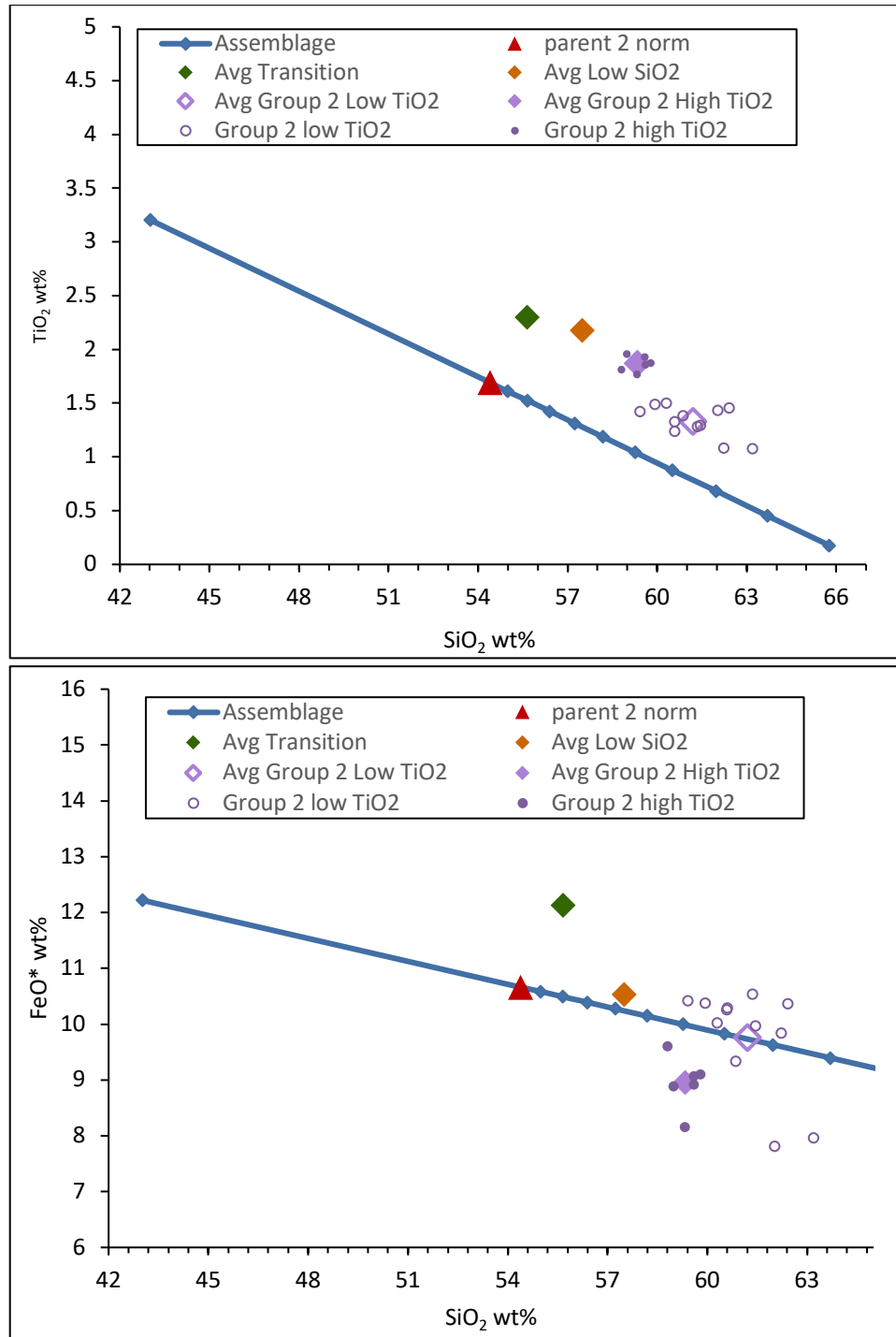
Figure 28. Variation diagrams of Group 2 icelandites and mass balance modeling results for the two important major elements, Fe and Ti. The blue line is the calculated crystallization path using the calculated assemblage beginning at 43% SiO_2 (blue diamond) from the mafic parent magma (red triangle), each tick mark (blue diamonds) along the crystallization line represents crystallization increments of 5%. Labeled points include the samples of group 1 as well as averages of the transition, low SiO_2, and Group 2 icelandites**.** Detailed results of the mass balance model can be found in appendix D.

Results of the fractional crystallization models were plotted for two of the most important major element oxides, TiO_2 and FeO (Figure 27 and 28). The blue line in both diagrams displays the projected crystallization path from the estimated parent magmas. The trajectory of the blue line is defined by the composition of the parent magmas and the composition of the "bulk" mineral crystallizing as estimated from modal proportions. The calculated composition trend from the parent magma towards the icelandites does not reproduce the observed compositions (figure 27). The group 1 icelandites could have formed by fractional crystallization processes if the concentration of FeO were higher and the concentration of TiO_2 were lower in the parent. For group 2, somewhat the opposite compositional systematics to group 1 would be required to be consistent with fractional crystallization. This means, the concentration of TiO_2 of parent to generate group 2 would need to be higher. Observed FeO* concentrations create a more difficult scenario and could only be reconciled if bulk mineral and parent would both be higher in FeO* leading to a steeper trend line than shown on (Fig. 28).
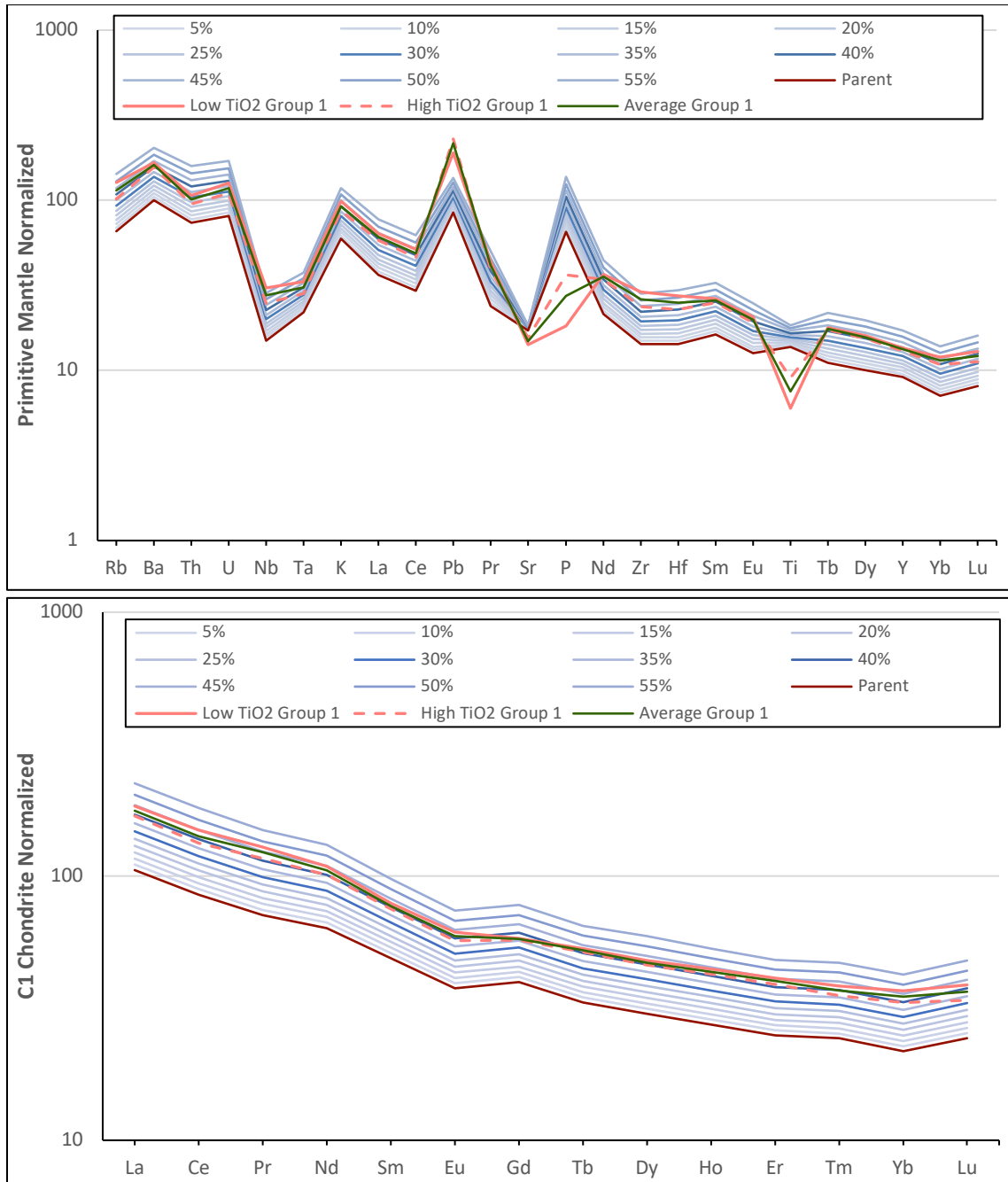
Figure 29. Spider diagram and REE diagram with fractional crystallization models, estimated parent, and observed Group 1 compositions.
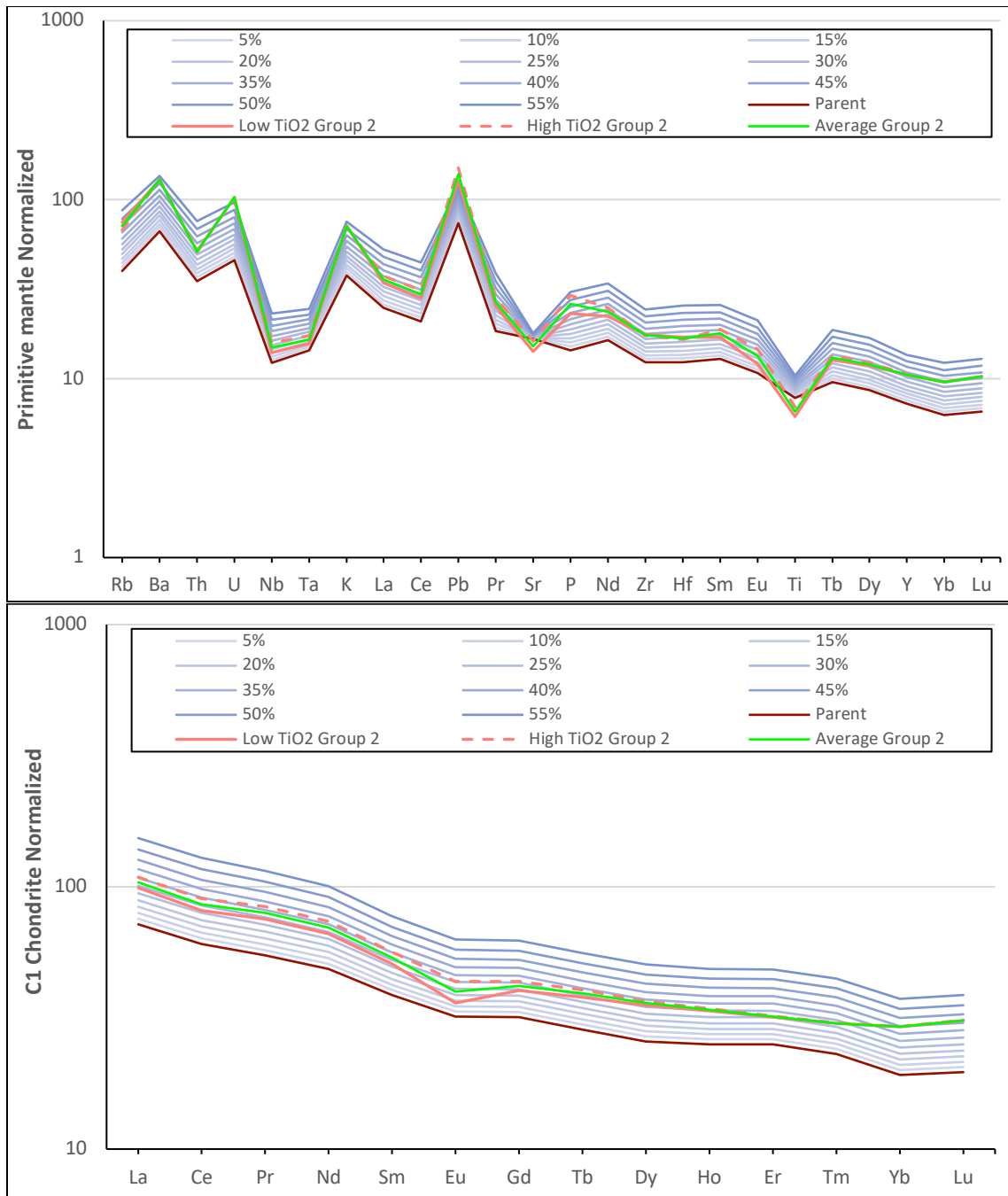
Figure 30. Spider diagram and REE diagram with fractional crystallization models, estimated parent, and observed Group 2 compositions.

The Rayleigh fractional crystallization model for group 1 and 2 in trace elements and REE

produced a different outcome that that of the major element oxides (see Figures 29 and

30). One can see that unlike the major element model, it is possible to generate a

magma that is similar to group 1 and 2 icelandites with Rayleigh crystallization models.

Within both groups, strontium and titanium are the elements that do not result in

concentrations similar to those of the icelandites using this type of model. Additionally,

one cannot reach the high concentration level observed in phosphorus in group 1 using

just Rayleigh fractionation.

Magma Mixing

The mass balance and Rayleigh fractionation models were not able to produce the

distinct geochemical signature that we see in the icelandites of groups 1 and 2. The

trace and the REE did show however that some degree of fractionation is likely involved

in the generation of the icelandites, but it is not the sole process involved. The next

most likely process that could have been operating to generate these magmas is mixing

between a mafic endmember and a felsic endmember,

I used as mafic endmembers the same two composition that I used as parent magmas

for the fractional crystallization models. As silicic end members I used an average

composition of the upper Littlefield rhyolite and averages of the 4 units of the Dinner

Creek Tuff. The selection is again based on suitable incompatible trace element

systematics observed in scatter diagrams (Figures 17-23). The differing composition of

the mafic endmember are meant to account for the differing concentrations of the two

icelandite groups. The mixing of ~63% of a slightly more enriched mafic endmember

with ~37% of the Upper Littlefield Rhyolite as the rhyolitic endmember successfully

produces the geochemical signature of the Group 1 icelandite (Figure 31). The fit of the

mixing model between a slightly more enriched mafic endmember with the Upper

Littlefield Rhyolite only has misfits with P and Ti in trace elements and a slight misfit in

Eu for REE (Figure 31).
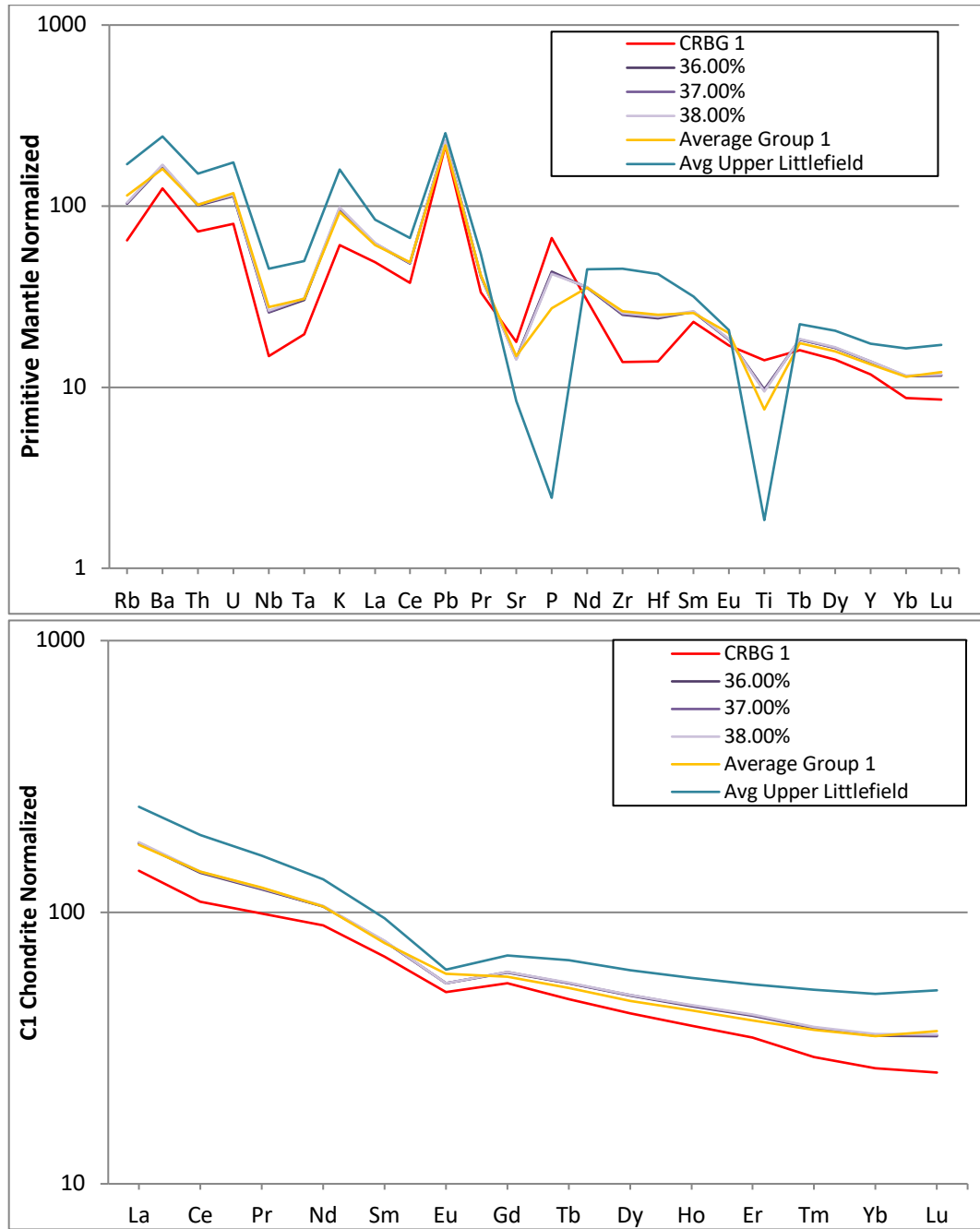
Figure 31. Primitive mantle normalized (Sun and McDonough, 1989) trace element diagram and C1 chondrite normalized REE (McDonough and Sun, 1995) diagram for results of mixing of averaged group 1 CRBG mafic endmember (determined by linear regression of group 1 icelandite concentrations) with Upper Littlefield Rhyolite. These values and the calculations for the mixing model can be found in Appendix E.
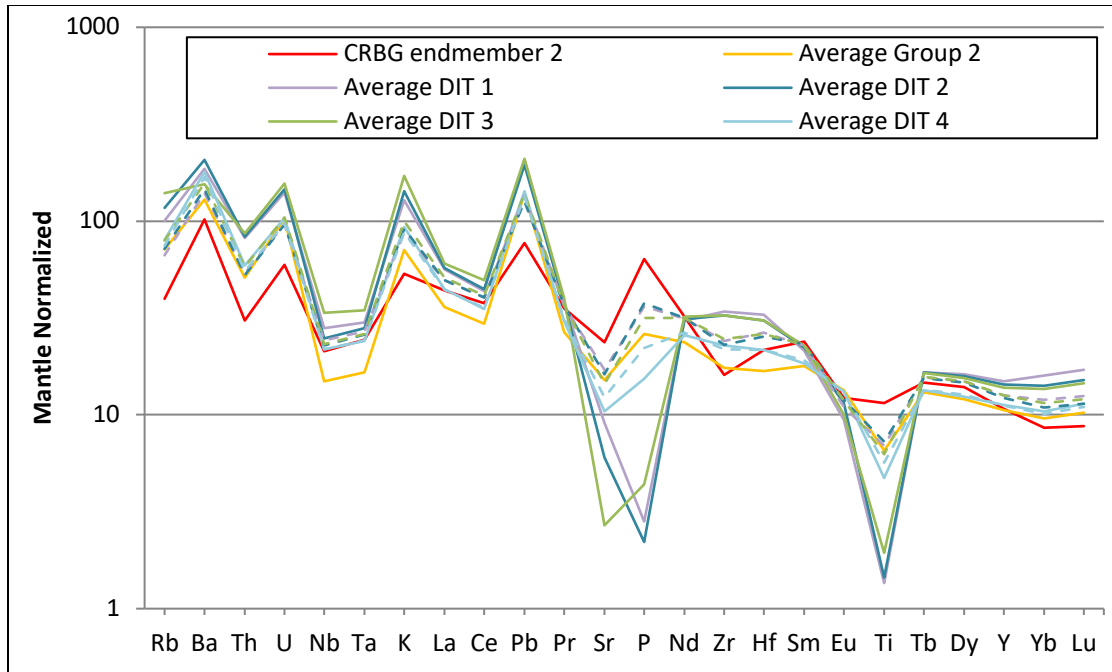
Figure 32. Primitive mantle normalized (Sun and McDonough, 1989) trace element diagram and C1 chondrite (McDonough and Sun, 1995) normalized REE diagram for mixing results of CRBG mafic endmember (determined by linear regression of group 2 icelandite concentrations) with DIT units 1 through 4 to generate group 2 compositions. (see Appendix E for compositions of mixing model)

The trace element mixing model of a group 2 CRBG-like endmember was generated with Dinner Creek Tuff (DIT) units 1-4 as the rhyolitic endmember (Figure 32). DIT units 1 and 2 were very quickly determined to not be the best candidate for producing the group 2 icelandites through mixing (see Appendix E). It is evident that a more depleted GRB like mafic endmember would be needed in order to produce the geochemical signature that we see with group 2.
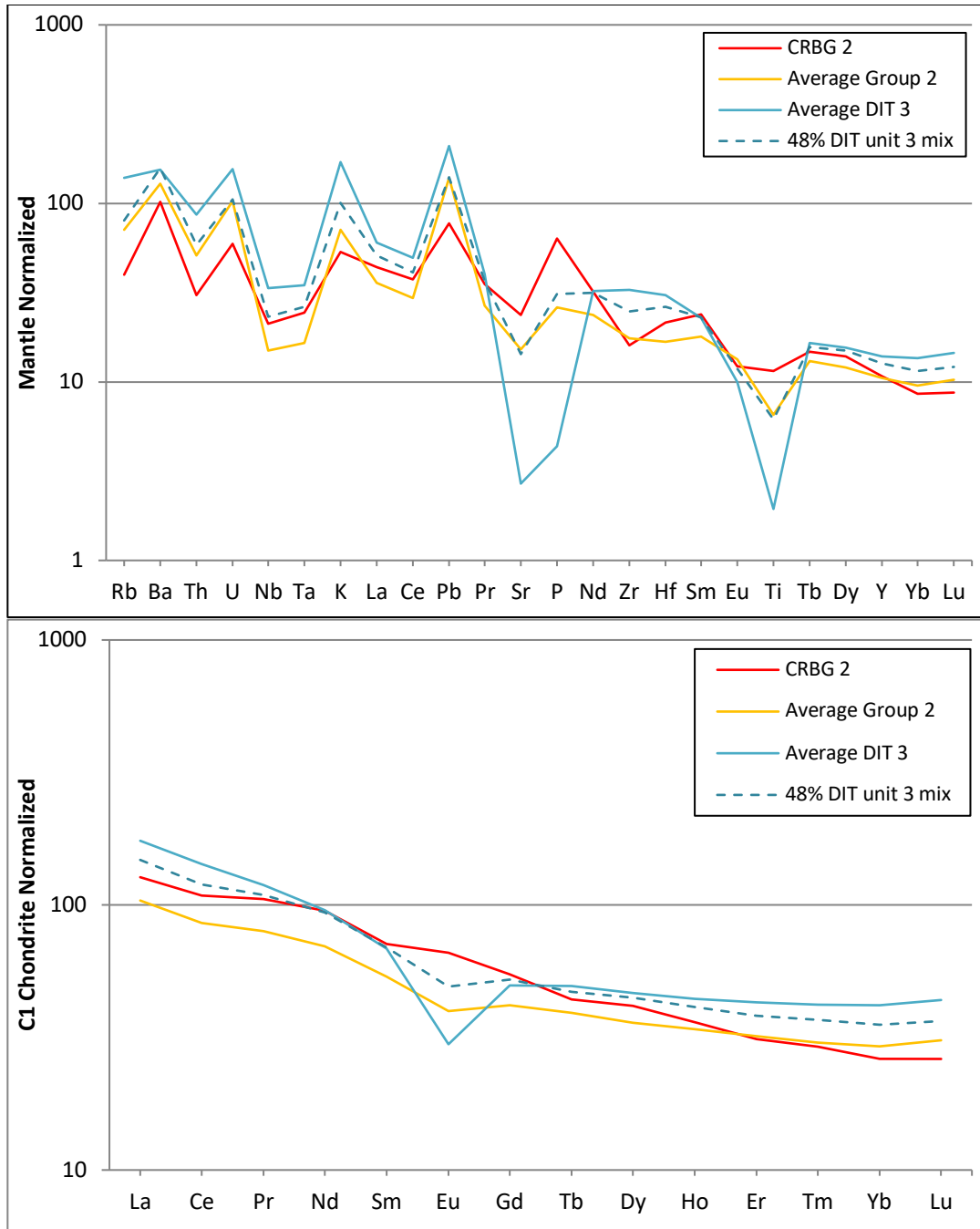
Figure 33. Primitive mantle normalized (Sun and McDonough, 1989) trace element diagram and C1 chondrite (McDonough and Sun, 1995) normalized REE diagram for mixing results of CRBG mafic endmember (determined by linear regression of group 2 icelandite concentrations) with DIT unit 3 to generate group 2 compositions. (see Appendix E for compositions of mixing model)

The mixing percent for the two DIT units that came the closest to the geochemistry of

the icelandites are 52% of a depleted Grande Ronde mafic endmember and ~48%

58

Dinner Creek Unit 3 (Figure 33 and 34). ~77% DIT unit 4 would need to mix with the

depleted Grande Ronde type mafic endmember to produce the group 2 icelandites. DIT

Unit 3 gets closer to the geochemical of the icelandites than DIT units 1 or 2 but still has

a number of misfits in trace and REE (Figure 33) as well as having an overall too high

level of enrichment. Dinner Creek Unit 4 has the most ideal match to the trace and REE

geochemical signature of the icelandites when ~77% percent DIT unit 4 is mixed with

23% of the GRB endmember for group 2 (Figure 34).
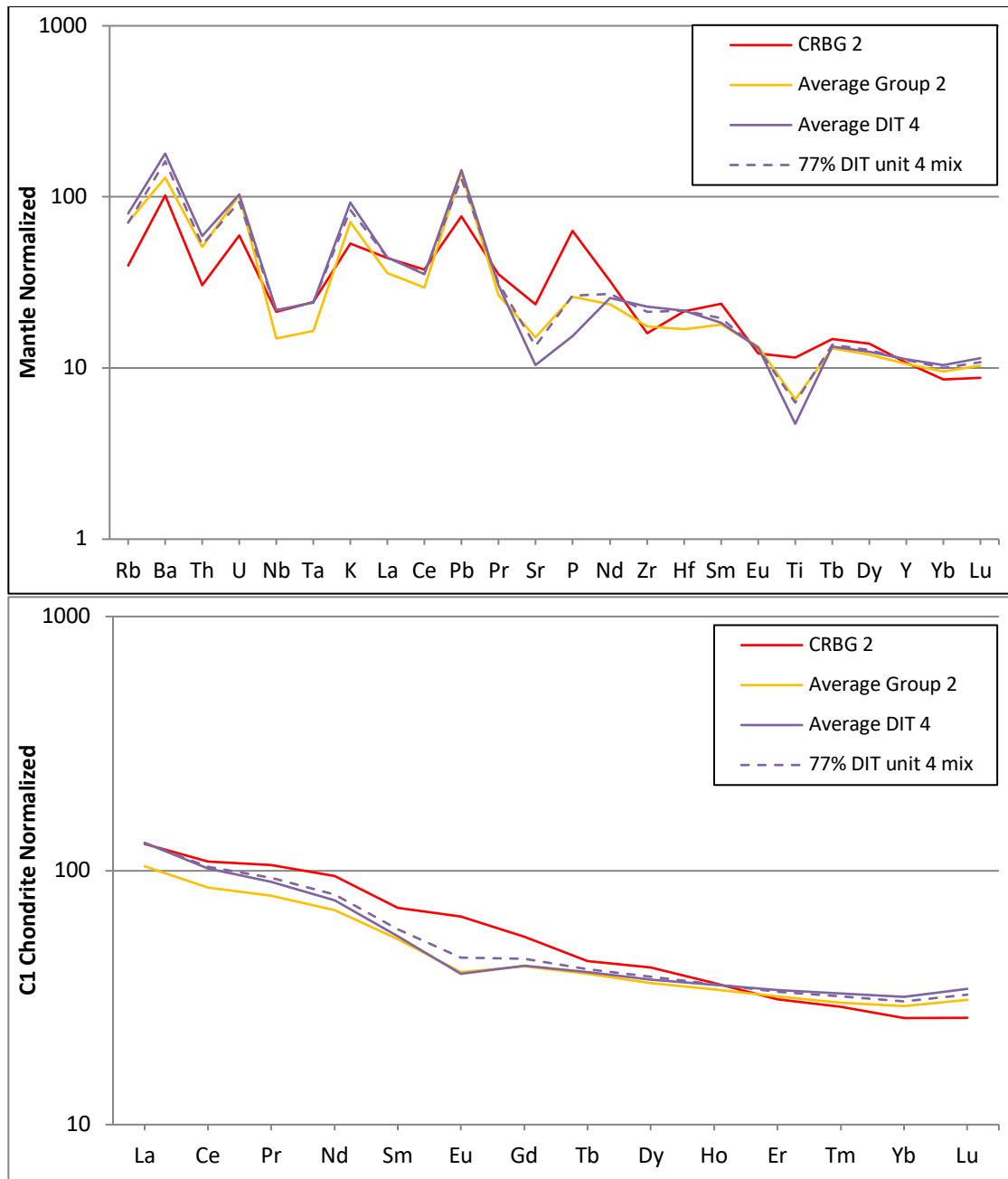
Figure 34. Primitive mantle normalized (Sun and McDonough, 1989) trace element diagram and C1 chondrite (McDonough and Sun, 1995) normalized REE diagram for mixing results of CRBG mafic endmember (determined by linear regression of group 2 icelandite concentrations) with DIT unit 4 to generate group 2 compositions. (see Appendix E for compositions of mixing model)

This requires a high level of felsic material to have mixed with the Grande Ronde type

mafic endmember in order to produce the icelandites which is not likely to occur

naturally. The major element concentrations that are produced by the mixing of the

60

Group 2 mafic endmember with Dinner Creek Unit 4 quickly exceeded the 59-63% range

of SiO$_2$ prior to achieving the necessary trace element enrichment levels of group 2. The

fit also has several misfits in important elements including Ba, Nb-Ta, Zr-Hf, and rare

earth elements La-Nd as well as the major element concentrations produced from the

model. These factors led to the determination that DIT unit 4 was also not the most

likely endmember to have mixed with a mafic endmember and produce the group 2

icelandites and that Dinner Creek Tuff unit 3 has the highest probability to have mixed

with the group 2 mafic endmember to produce the group 2 icelandites.

REGIONAL DISTRIBUTION

Geochemical data acquired from previous work and the data produced from this study

have shown that mid Miocene icelandites are closely related in space and time to the

Grande Ronde Basalt main phase member of the CRBG. The data produced in this study

also support the idea that the Hunter Creek Basalt is equivalent to late-stage Grande

Ronde lavas in the Malheur River Gorge and vicinity. Both, Webb (2017) and Cruz

(2017), posited sources of the erupted icelandite lavas in their geographic study areas

(Figure 35). It is feasible that both of these source regions in the Malheur Gorge and

Ironside Mountain for the icelandites are possible. The mixing models between the

mafic and rhyolitic members have shown that the two groups of icelandites had slightly

different mafic endmembers and that they also required different rhyolitic endmembers

in order to achieve a mixture that resembled the geochemical signature seen in the

data. In the area around Castle Rock Caldera and Ironside Mountain, the majority of the

icelandite rocks are found stratigraphically above Dinner Creek Tuff unit 2 and below

Dinner Creek Unit 4.

The model for the mixing of the GRB-type basaltic endmember for group 2 with the

Dinner Creek Tuff unit 3 rhyolitic endmember is the closest match for producing the

icelandites of group 2. This is supported by the stratigraphic positioning of the

icelandites in the vicinity of Ironside Mountain which was proposed by Cruz (2017) and a

possible source region of the icelandites. This idea could also be applied to generation of

the group 1 icelandites from mixing of the GRB-type basaltic endmember for group 1

and Upper Littlefield Rhyolite. In this case the icelandites reside stratigraphically above

the lower Littlefield Rhyolite and below the upper Littlefield rhyolite.

It has been previously shown that the Grande Ronde Basalt and Hunter Creek Basalt

share a connection with the Littlefield rhyolite and Dinner Creek Tuff through

stratigraphic position within the areas of emplacement shared between the units and

the shared timing of emplacement (Streck et al., 2015; Webb et al, 2018). The

geochronological and stratigraphic information on icelandites shows that icelandites

erupted at the end of Grande Ronde Basalt activity around 16 Ma to slightly later

around >15 Ma (Table 5). The ages of icelanditic components that were recorded as

eruptive components of the Buchanan Tuff (15.1 Ma), Dinner Creek Tuff Unit 4 and

Wildcat Creek Tuff (15.5 Ma) also lend support to the idea that these icelandites

emplaced at some point before these units were erupted.

Other studies have revealed the existence of mid Miocene icelandites south of the studied area and thus should be included in the total distribution area of mid Miocene icelandites.

Table 5. Selected ages of mid-Miocene icelanditic units and components.

Unit	Reported Age (Ma)	Stratigraphic Age	Source of age
Icelanditic component of Buchanan Tuff	15.1		Vranizan and Streck, GSA Cordilleran 2018
Icelanditic component of Dinner Creek Unit 4	15.2		Streck and McIntosh, unpubl.
Icelanditic component of Wildcat Creek Tuff	15.5		Sales, 2017
Icelandite of Alder Creek	>16.05 and <16.1		Webb et al., 2018
Icelandites at Ironside Mountain		>15.5	Cruz, 2017
Icelandites at Castle Rock		>15.5	Cruz, 2017
Fiddler's Hell icelandite of Indian Rock	15.54 ± 0.10		Ferns and McConnell, 2005
tholeiitic andesite capping flows at Lambing Canyon	15.17±0.18		Brueseke and Hart, 2007
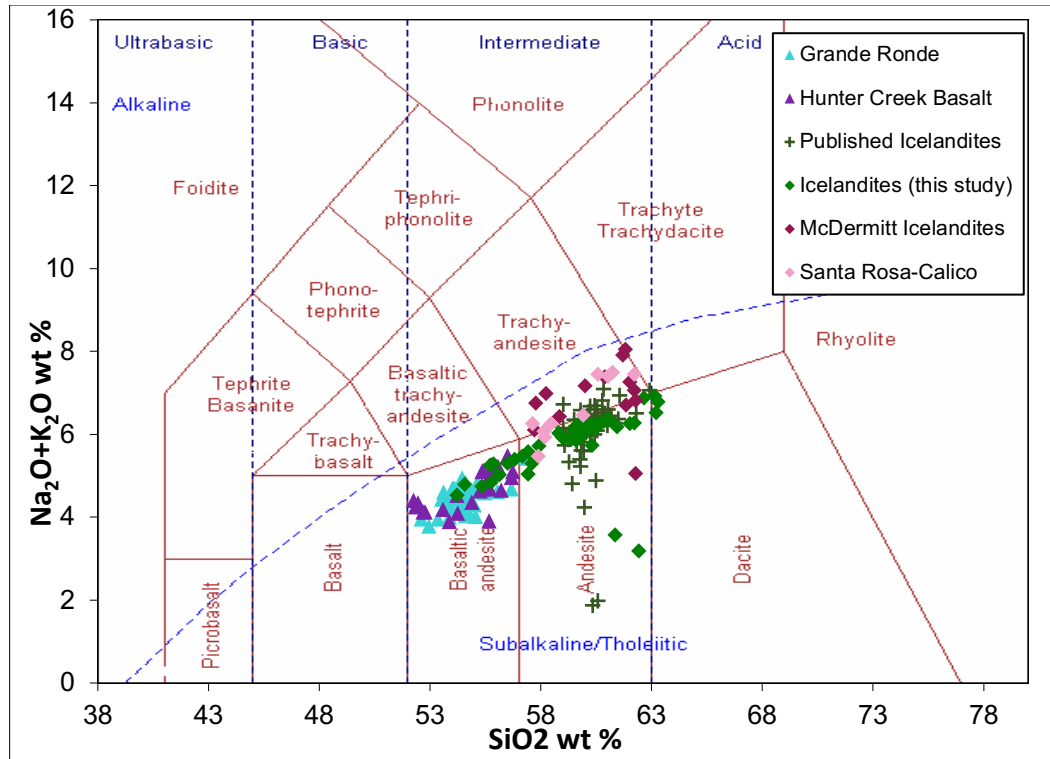
Figure 35. Plot of total alkali versus silica content mid-Miocene icelandites of this study, capping andesites of Folly Farm West, icelanditic rocks of the McDermitt Volcanic Field, and icelanditic rocks of the Santa Rosa-Calico Volcanic Field. Analyses are from this study, Brueseke and Hart (2007) and Brueseke et al. (2009), and Starkel (2014).
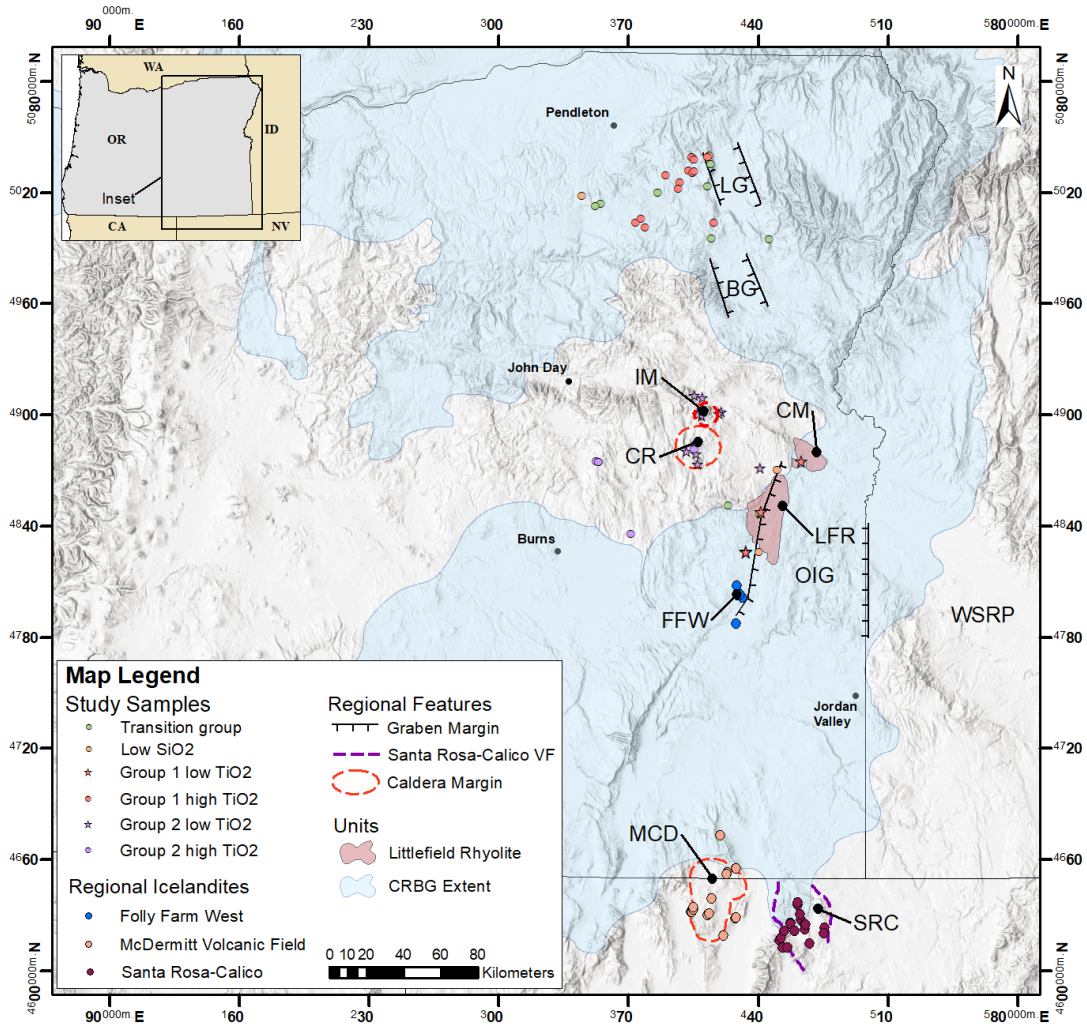
Figure 36. Regional distribution of icelandites including those of this study, FFW—tholeiitic andesites of Folly Farm West in Lambing Canyon, MCD—icelandites of the McDermitt Volcanic Field, SRC—icelandites of Santa Rosa-Calico Volcanic Field**.** Regional features are as follows: WA—Washington; OR—Oregon; ID—Idaho; LG—La Grande graben; BG—Baker graben; OIG—Oregon-Idaho graben; CR—Castle Rock Caldera; SM—Strawberry Volcanics; IM—Ironside Mountain; LFR—Littlefield Rhyolite; CM—Rhyolite of Cottonwood Mountain; WSRP—Western Snake River Plain.

The extended distribution of icelandites includes the tholeiitic capping andesites at

Lambing Canyon in Folly Farm West of Brueseke and Hart (2007). The capping andesites

of Lambing Canyon have a similar icelanditic geochemical signature to the icelandites of

this study, and the age of the unit (Figures 35, 37-39) (Table 3) is also similar to those of

this study. Additionally, reports of similar rocks to those found at the top of Lambing

65
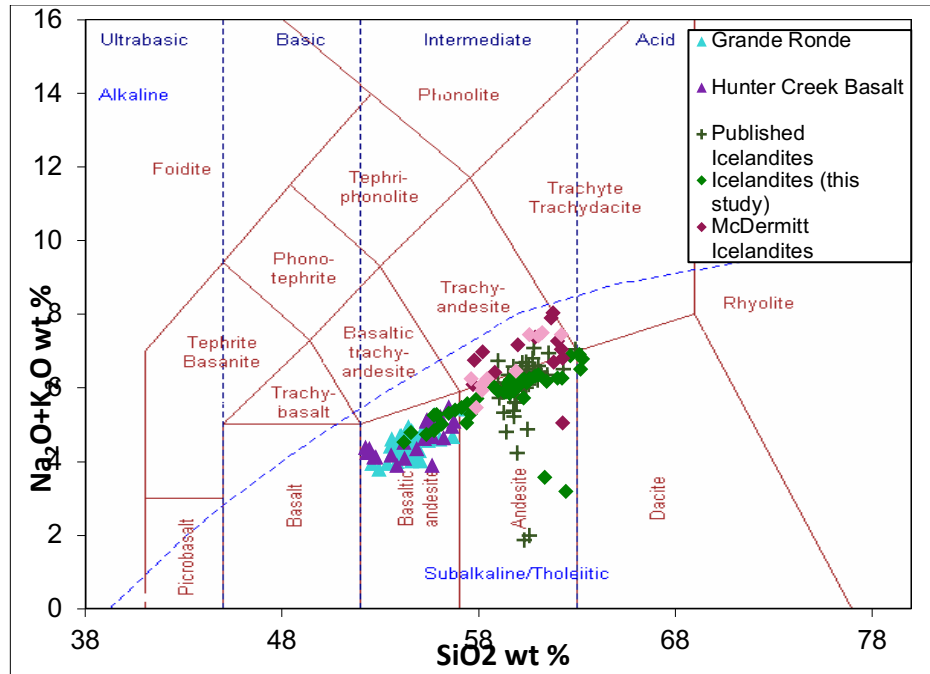
Figure 37. Plot of total alkali versus silica content mid-Miocene icelandites of this study, capping andesites of Folly Farm West, icelanditic rocks of the McDermitt Volcanic Field, and icelanditic rocks of the Santa Rosa-Calico Volcanic Field. Analyses are from this study, Brueseke and Hart (2007) and Brueseke et al. (2009), and Starkel (2014).
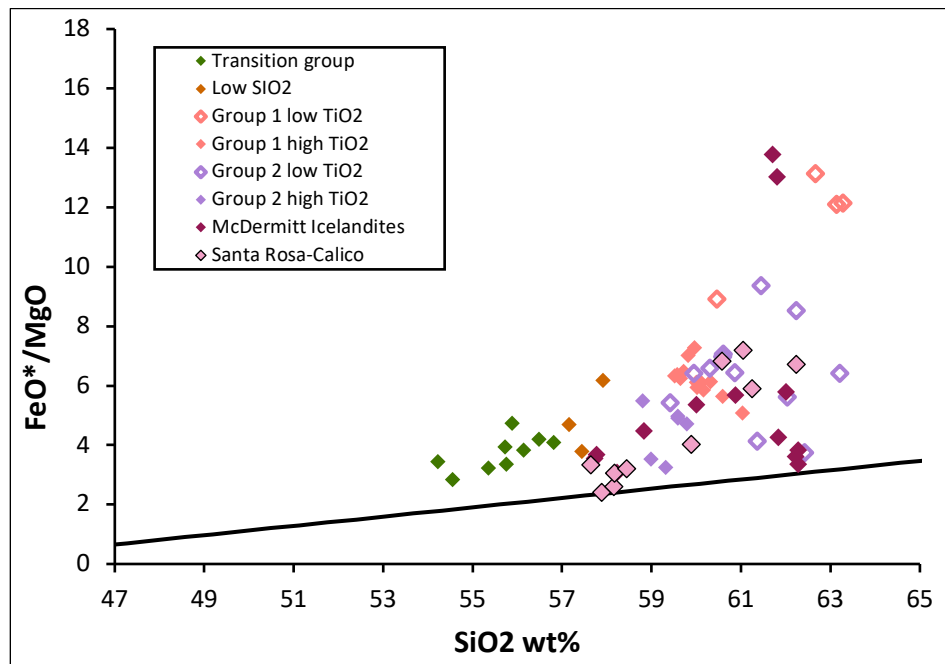
Figure 38. Plot of FeO*/MgO ratio versus silica content mid-Miocene icelandites of this study, capping andesites of Folly Farm West, icelanditic rocks of the McDermitt Volcanic Field, and icelanditic rocks of the Santa Rosa-Calico Volcanic Field. Analyses are from this study, Brueseke and Hart (2007) and Brueseke et al. (2009), and Starkel (2014).
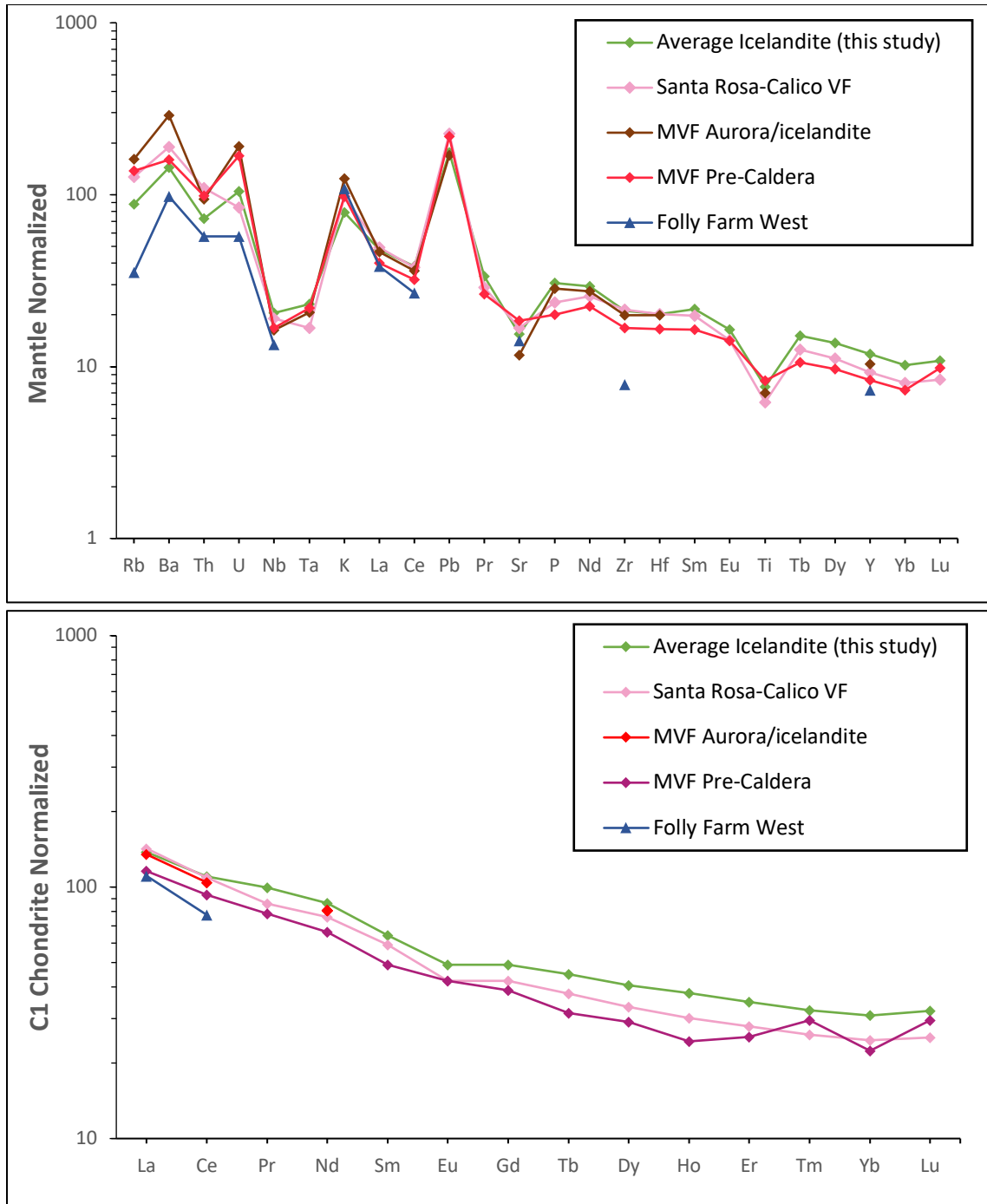
Figure 39. Primitive mantle normalized (Sun and McDonough, 1989) trace element diagram and C1 chondrite (McDonough and Sun, 1995) normalized REE diagram of averaged values of Grande Ronde Basalt, Hunter Creek basalt, icelandites of this study, and icelanditic rocks of the Santa Rosa-Calico Volcanic Field, McDermitt Volcanic Field and tholeiitic andesites of Lambing Canyon in Folly Farm West.

canyon can also be found in the surrounding area of Steens Mountain and just to the

east in the Sheepshead Mountains (M. Brueseke, personal communication). Other

icelanditic rocks have been reported by Brueseke et al. (2009) in the Santa Rosa-Calico

Volcanic Field. Also, Starkel (2014) reported additional icelanditic rocks, the post caldera

Aurora icelandites and lavas as well as several pre caldera intermediate units, in the

Mcdermitt Volcanic Field (Figure 37).

Conclusions

This study focuses on the distribution, petrology, and geochemistry of mid-Miocene icelandites in eastern Oregon and examines their connection to the Columbia River Basalt Group magmas. Existing research of these rocks is limited and has been restricted to icelandites of the La Grande graben in the northern end of the La Grande-Owyhee eruptive axis and the Oregon-Idaho graben in the south with no work completed in the region in between the two grabens.

The mid-Miocene icelandites discussed in this study erupted of a large part of eastern Oregon and generally correspond to the area from the towns of John Day in the NW, Burns in the SW, La Grande in the NE and Vale in the SE. This area is centered on where all main phase CRBG members overlap along the Malheur Gorge between the towns of Juntura and Vale. This distribution of mid Miocene icelandites is much larger than previously reported. Lithologically, the icelandites of the Fiddlers Hell unit within the La Grande graben, Alder Creek icelandites and the Hunter Creek basalt in the Malheur Gorge are extremely similar when viewed on a macroscopic scale. With the inclusion of other regional mid-Miocene icelandites of Starkel (2015) in McDermitt Volcanic field and those of Brueseke and Hart (2007) and Brueseke et al. (2009), the southern distribution area of mid Miocene icelandites extends into Nevada.

The geochemical signatures of icelandites are distinctly different to main phase CRBG and therefore they should not be incorporated as part of other units as prior work has done with the exception of the Fiddlers Hell unit, but instead these rocks should be treated as its own unit. The icelandites themselves form two groups with each forming 2

subgroups based on the concentration of numerous trace elements including REE as well as the major elements Al and Ti. Group 1 consists of samples that are more enriched in incompatible trace elements while Group 2 samples are less enriched. Both Groups indicate a high and lower Ti group. The preferred petrologic models to explain icelandites is mixing between a Grande Ronde-like mafic endmember with a rhyolitic endmember, although group 1 and 2 require different mafic and silicic endmembers. Group 1 icelandites require a more enriched mafic and silicic endmember, while Group 2 require less enriched endmembers. The results of the group 1 model show that the upper Littlefield rhyolite has the highest probability of having mixed with the mafic endmember to create the group 1 icelandites. The results of the group 2 model show a high probability of having been the result of a mixture with Dinner Creek Tuff Unit 4. The results of the mixing models also lend support to the idea that the icelandites had at least two main eruptive centers.

This study also shed more light on the mineralogy of these rocks that was not well known compared to the mineralogy of the main phase members of the CRBG. The icelandites are generally aphanitic texturally but they can vary in phenocryst abundance. Previous reports also do not note the presence of apatite in the mineralogy

In addition to the spatial proximity among icelandites, CRBG units and mid Miocene rhyolites, this study has also shown a strong geochemical connection between mid-Miocene rhyolites of eastern Oregon and the Grande Ronde basalt of the CRBG.

References

Bailey, D.G., 1990, Geochemistry and Petrogenesis of Miocene Volcanic Rocks in the

Powder River Volcanic Field, Northeastern Oregon [Ph.D. dissertation]: Pullman,

Washington, Washington State University, 341 p.

Bailey, M.M., 1989, Revisions to stratigraphic nomenclature of the Picture Gorge Basalt

Subgroup, Columbia River Basalt Group, in Reidel, S.P, and Hooper, P.R., eds.,

Volcanism and Tectonism in the Columbia River Flood Basalt Province: Geological

Society of America Special Paper 239, p. 67–84.

Barry, T.L., Kelley, S.P., Reidel, S.P., Camp, V.E., Self, S., Jarboe, N.A., Duncan, R.A., and

Renne, P.R., 2013, Eruption chronology of the Columbia River Basalt Group, in

Reidel, S.P., et al., eds., The Columbia River Flood Basalt Province: Geological

Society of America Special Paper 497, p. 45–66, doi: 10 .1130 /2013 .2497 (02).

Binger, G.B., 1997, The Volcanic Stratigraphy of the Juntura Region, Eastern Oregon

[M.S. thesis]: Pullman, Washington, Washington State University, 206 p.

Bougault, H., and Hekinian, R., 1974, Rift Valley in the Atlantic Ocean near 36°50′ N:

petrology and geochemistry of basaltic rocks. Earth and Planetary Science

Letters, 24(2), 249–261. https://doi.org/10.1016/0012-821X(74)90103-4

Brooks, H.C., 2006, Preliminary geologic and mineral resources map of the Mormon

basin quadrangle, Baker and Malheur Counties, Oregon: Oregon Department of

Geology and Mineral Industries Open-File O–06–25, scale 1:24,000.

Brooks, H.C., 1992. Preliminary geologic map of the Copeland Reservoir quadrangle.

    Malheur County, Oregon: Oregon Department of Geology and Mineral Industries

    Open-File Report O-93-3, scale, 1, pp.24-000.

Brooks, H.C., and O'Brien, J.P., 1992a, Geology and mineral resources map of the Little

    Valley quadrangle, Malheur County, Oregon: Oregon Department of Geology and

    Mineral Industries Geologic Map Series GMS-72, 1 sheet, scale 1:24,000.

Brooks, H.C., and O'Brien, J.P., 1992b, Geology and mineral resources map of the

    Westfall quadrangle, Malheur County, Oregon: Oregon Department of Geology

    and Mineral Industries Geologic Map Series GMS-71, 1 sheet, scale 1:24,000.

Brueseke, M.E. and Hart, W.K., 2009, Intermediate composition magma production in an

    intracontinental setting: Unusual andesites and dacites of the mid-Miocene

    Santa Rosa–Calico volcanic field, northern Nevada. Journal of Volcanology and

    Geothermal Research, 188(1-3), pp.197-213.

Brueseke, M.E., Heizler, M.T., Hart, W.K., and Mertzman, S.A., 2007, Distribution and

    geochronology of Oregon Plateau (U.S.A.) flood basalt volcanism: The Steens

    Basalt revisited: Journal of Volcanology and Geothermal Research, v. 161, no. 3,

    p. 187–214, doi:10.1016/j.jvolgeores.2006.12.004.

Brunet, F., and Chazot, G., 2001, Partitioning of phosphorus between olivine,

    clinopyroxene and silicate glass in a spinel lherzolite xenolith from Yemen.

Chemical Geology, 176(1–4), 51–72. https://doi.org/10.1016/S0009-2541(00)00351-X

Cahoon, E.B., 2020. Distribution, Geochronology, and Petrogenesis of the Picture Gorge Basalt with Special Focus on Petrological Relationships to the Main Columbia River Basalt Group. [Ph.D Dissertation]: Portland, Oregon, Portland State University, 181 p.

Camp, V.E., 2013, Origin of Columbia River Basalt: Passive rise of shallow mantle, or active upwelling of a deep-mantle plume?, in Reidel, S.P., Camp, V.E., Ross, M.E., Wolff, J.A., Martin, B.S., Tolan, T.L., and Wells, R.E., eds., The Columbia River Flood Basalt Province, Volume 497, Geological Society of America Special Paper, p. 181-199.

Camp, V.E., and Ross, M.E., 2004, Mantle dynamics and genesis of mafic magmatism in the intermontane Pacific Northwest: Journal of Geophysical Research, v. 109, 14p.

Camp, V.E., Ross, M.E., and Hanson, W.E., 2003, Genesis of flood basalts and Basin and Range volcanic rocks from Steens Mountain to the Malheur River Gorge, Oregon: Geological Society of America Bulletin, v. 115, no. 1, p. 105–128.

Carlson, R.W., and Hart, W.K., 1987, Crustal genesis on the Oregon Plateau: Journal of Geophysical Research, v. 92, no. B7, 6191–6206, doi:10.1029/JB092iB07p06191.

Carmichael, I. S. E., 1964, The petrology of Thingmuli, a Tertiary volcano in eastern

Iceland: Journal of Petrology, v. 5, part 3, p. 435-460.

Cruz, M., 2017. Field Mapping Investigation and Geochemical Analysis of Volcanic Units

within the Dinner Creek Tuff Eruptive Center, Malheur County, Eastern Oregon.

[Master's Thesis]: Portland, Oregon, Portland State University, 217 p.

Cummings, M.L., Evans, J.G., Ferns, M.L., and Lees, K.R., 2000, Stratigraphic and

structural evolution of the middle Miocene synvolcanic Oregon-Idaho graben:

Geological Society of America Bulletin, v. 112, p. 668–682.

Dunn, T., and Sen, C., 1994, Mineral/matrix partition coefficients for orthopyroxene,

plagioclase, and olivine in basaltic to andesitic systems: A combined analytical

and experimental study. Geochimica et Cosmochimica Acta, 58(2), 717–733.

https://doi.org/10.1016/0016-7037(94)90501-0

Edwards, J.H., 2013, Structural Controls of the Neal Hot Springs Geothermal System,

Eastern Oregon [M.S. Thesis]: University of Nevada, Reno, Nevada, 92 p.

ESRI. (2020, May 12). ArcGIS 10.8.1.

Ewart, A., and Griffin, W.L., 1994, Application of proton-microprobe data to trace-

element partitioning in volcanic rocks: Chemical Geology, v. 117, p. 251–284,

doi:10.1016/0009-2541(94)90131-7.

Evans, J.G., and Binger, G.B., 1999c, Geologic map of the Alder Creek quadrangle,

Malheur County, Oregon: U.S. Geological Survey Open-File Report 98-494, 12 p.,

1 sheet, scale 1:24,000, https:// doi .org /10 .3133 /ofr98494 .

Ferns, M.L., Streck, M.J. and McClaughry, J.D., 2017. Field-trip guide to Columbia River

flood basalts, associated rhyolites, and diverse post-plume volcanism in eastern

Oregon (No. 2017-5022-O). US Geological Survey.

Ferns, M.L., and McClaughry, J.D., 2013, Stratigraphy and volcanic evolution of the

middle Miocene to Pliocene La Grande–Owyhee eruptive axis in eastern Oregon,

in Reidel, S.P., et al., eds., The Columbia River Flood Basalt Province: Geological

Society of America Special Paper 497, p. 401–427, doi: 10 .1130 /2013 .2497

(16).

Ferns, M.L., McConnell, V.S., Madin, I.P., and Johnson, J.J., 2010, Geology of the Upper

Grande Ronde Basin, Union County, Oregon: Oregon Department of Geology and

Mineral Industries Bulletin 107, map scale 1:100,000.

Ferns, M.L., and McConnell, V.S., 2005, Geoanalytical Information Layer for Oregon,

Release 1: Oregon Department of Geology and Mineral Industries Digital Data

Series GILO-1 (on CD-ROM).

Ferns, M.L., and O'Brien, J.P., 1992a, Geology and mineral resources map of the Namorf

quadrangle, Malheur County, Oregon: Oregon Department of Geology and

Mineral Industries Geologic Map Series GMS-74, 1 sheet, scale 1:24,000.

Ferns, M.L., and O'Brien, J.P., 1992b, Geology and mineral resources map of the Harper

    quadrangle, Malheur County, Oregon: Oregon Department of Geology and

    Mineral Industries Geologic Map Series GMS-69, 1 sheet, scale 1:24,000.

Ferns, M.L., 1989a, Geology and mineral resources map of the Graveyard Point

    quadrangle, Malheur County, Oregon, and Owyhee County, Idaho: Oregon

    Department of Geology and Mineral Industries Geological Map Series GMS–54,

    scale 1:24,000.

Ferns, M.L., 1989b, Geology and mineral resources map of the Owyhee Ridge

    quadrangle, Malheur County, Oregon: Oregon Department of Geology and

    Mineral Industries Geological Map Series GMS–53, scale 1:24,000.

Fujimaki, H., 1986, Partition coefficients of Hf, Zr, and REE between zircon, apatite, and

    liquid. Contributions to Mineralogy and Petrology, 94(1), pp.42-45.

Gill, 1981, "Orogenic andesites and plate tectonics": Berlin-New York, Springer-Verlag, p.

    160-163.

Green, T.H., Blundy, J.D., Adam, J., and Yaxley, G.M., 2000, SIMS determination of trace

    element partition coefficients between garnet, clinopyroxene and hydrous

    basaltic liquids at 2-7.5 GPa and 1080-1200°C: Lithos, v. 53, p. 165–187,

    doi:10.1016/S0024-4937(00)00023-2.

Green, J.C. and Fitz III, T.J., 1993. Extensive felsic lavas and rheoignimbrites in the

Keweenawan Midcontinent Rift plateau volcanics, Minnesota: petrographic and

field recognition. Journal of Volcanology and Geothermal Research, 54(3-4),

pp.177-196.

Green, T.H., Sie, S.H., Ryan, C.G., and Cousens, D.R., 1989, Proton microprobe-

determined partitioning of Nb, Ta, Zr, Sr and Y between garnet, clinopyroxene

and basaltic magma at high pressure and temperature: Chemical Geology, v. 74,

p. 201–216, doi:10.1016/0009-2541(89)90032-6.

Hart, Stanley R., and Todd Dunn., 1993, "Experimental Cpx/Melt Partitioning of 24 Trace

Elements." Contributions to Mineralogy and Petrology 113 (1): 1–8.

Hooper, P.R., Binger, B.G., and Lees, K.L., 2002, Vale Project Analyses: Whole Rock Major

and Trace Element Analysis by XRF. GeoAnalytical Laboratory, Washington State

University. (Samples collected by Jim Evans, Mark Ferns, Howard Brooks, Jenda

Johnson, Kate Lees, Mandi Francis, Ben Binger, Chris Hawkesworth, and Peter

Hooper.)

Hooper, P.R., Binger, G.G., and Lees, K.R., 2002a, Ages of the Steens and Columbia River

flood basalts and their relationship to extension-related calc-alkalic volcanism in

eastern Oregon: Geological Society of America Bulletin, v. 114, no. 1, p. 43–50,

doi:10.1130/0016-7606(2002) 114<0043:AOTSAC>2.0.CO;2.

Hooper, P. R., 2000, Chemical discrimination of Columbia River basalt flows:

Geochemistry, Geophysics, and Geosystems, v. 1, no. 6, 1024,

doi:10.1029/2000GC000040.

Hooper P. R., Hawkesworth C. J., 1993, Isotopic and geochemical constraints on the

origin and evolution of the Columbia River Basalt: Journal of Petrology, v. 34, p.

203-1246.

Hooper, P.R., and Swanson, D.A., 1990, The Columbia River Basalt Group and associated

volcanic rocks of the Blue Mountains Province, in Walker, G.W., ed., Geology of

the Blue Mountains Region of Oregon, Idaho, and Washington: Cenozoic Geology

of the Blue Mountains Region: U.S. Geological Survey Professional Paper 1437, p.

63–99.

Irvine, T.N., and Baragar, W.R.A., 1971, A guide to the chemical classification of the

common volcanic rocks: Canadian Journal of Earth Sciences, v. 8, p. 523-548.

Jang, Y.D., and Naslund, H.R., 2003, Major and trace element variation in ilmenite in the

Skaergaard Intrusion: Petrologic implications: Chemical Geology, v. 193, p. 109–

125, doi:10.1016/S0009-2541(02)00224-3.

Jarboe, N.A., Coe, R.S., Renne, P.R., and Glen, J.M.G., 2010, The age of the Steens

reversal and the Columbia River Basalt Group: Chemical Geology, v. 274, p. 159-

168.

Jónasson, K., Holm, P.M., and Pedersen, A.K., 1992. Petrogenesis of silicic rocks from the Króksfjördur central volcano, NW Iceland. Journal of Petrology, 33(6), pp.1345-1369.

Kittleman, L.R., Green, A.R., Haddock, G.H., Hagood, A.R., Johnson, A.M., McMurray, J.M., Russell, R.G., and Weeden, D.A., 1967, Geologic map of the Owyhee region, Malheur County, Oregon: Eugene, University of Oregon Museum of Natural History Bulletin 8, scale 1:125 000.

Kittleman, L.R., Green, A.R., Hagood, A.R., Johnson, A.M., McMurray, J.M., Russell, R.G., and Weeden, D.A., 1965, Cenozoic stratigraphy of the Owyhee region, southeastern Oregon: Eugene, University of Oregon Museum of Natural History Bulletin 1, 45 p.

Klemme, S., Günther, D., Hametner, K., Prowatke, S., and Zack, T., 2006, The partitioning of trace elements between ilmenite, ulvospinel, armalcolite and silicate melts with implications for the early differentiation of the moon. Chemical Geology, 234(3–4), 251–263. https://doi.org/10.1016/j.chemgeo.2006.05.005

Kloeck, W. and Palme, H., 1988, Proceedings of the Lunar and Planetary Science Conference. In Proceedings of the Lunar and Planetary Science Conference (Vol. 18, pp. 471-483).

Korosec, M.A., 1987, Geologic map of the Hood River Quadrangle, Washington and Oregon, doi:10.2172/6464338.

Lambert, R.S., Chamberlain, V.E. and Holland, J.G., 1995. Ferro-andesites in the Grande Ronde Basalt: their composition and significance in studies of the origin of the Columbia River Basalt Group. Canadian Journal of Earth Sciences, 32(4), pp.424-436.

Langmuir, C.H., Vocke Jr, R.D., Hanson, G.N. and Hart, S.R., 1978, A general mixing equation with applications to Icelandic basalts. Earth and Planetary Science Letters, 37(3), pp.380-392.

Laubier, M., Grove, T.L., and Langmuir, C.H., 2014, Trace element mineral/melt partitioning for basaltic and basaltic andesitic melts: An experimental and laser ICP-MS study with application to the oxidation state of mantle source regions: Earth and Planetary Science Letters, v. 392, p. 265–278, doi:10.1016/j.epsl.2014.01.053.

Le Bas, M.J., Le Maitre, R.W., Streckeisen, A., and Zanettin, B., 1986, A chemical classification of volcanic rocks based on the total alkali – silica diagram: Journal of Petrology, v. 27, p. 745–750.

Lemarchand, F., Villemant, B. and Calas, G., 1987, Trace element distribution coefficients in alkaline series. Geochimica et Cosmochimica Acta, 51(5), pp.1071-1081.

Lees, K.R., 1994, Magmatic and Tectonic Changes through Time in the Neogene Volcanic Rocks of the Vale Area, Oregon, Northwestern USA [Ph.D. thesis]: Milton Keynes, UK, The Open University–Milton Keynes, 282 p.

Ma, L., Madin, I.P., Olson, K.V., and Watzig, R.J., 2009, Oregon Geological Data

Compilation: Oregon Department of Geology and Mineral Industries, v. 5.

MacLeod, N.S., 1990a, Geology and mineral resources map of the Mahogany Gap

Quadrangle, Malheur County, Oregon: Oregon Department of Geology and

Mineral Industries Geological Map Series GMS-65, scale 1:24 000.

Madin, I.P., 1997, Geologic Map of the Tucker Flat Quadrangle, Union and Baker

Counties, Oregon: Oregon Department of Geology and Mineral Industries

Geological Map Series GMS-110, 9 p., scale 1:24,000.

Mancini, A., Mattsson, H.B. and Bachmann, O., 2015. Origin of the compositional

diversity in the basalt-to-dacite series erupted along the Heiðarsporður ridge, NE

Iceland. Journal of Volcanology and Geothermal Research, 301, pp.116-127.

Matsui, Y., N. Onuma, H. Nagasawa, H. Higuchi, and S. Banno., 1977, "Crystal Structure

Control in Trace Element Partition between Crystal and Magma." Bulletin de La

Societe Francaise de Mineralogie et de Cristallographie 100 (6): 315–24.

McDonough, W.F., and Sun, S.S., 1995, The composition of the Earth: Chemica Geology,

v. 120, p. 223-253.

McKay, Gordon A., Jerry Wagstaff, and S. R. Yang., 1986, "Zirconium, Hafnium, and Rare

    Earth Element Partition Coefficients for Ilmenite and Other Minerals in High-Ti

    Lunar Mare Basalts; an Experimental Study." Journal of Geophysical Research 91

    (B4): D229–37. doi:10.1029/JB091iB04p0D229.

McKenzie, Dan, and R. K. O'Nions., 1991, "Partial Melt Distributions from Inversion of

    Rare Earth Element Concentrations." Journal of Petrology 32 (5): 1021–91.

Mysen, B. O., 1978, "Experimental Determination of Nickel Partition Coefficients

    between Liquid, Pargasite, and Garnet Peridotite Minerals and Concentration

    Limits of Behavior According to Henry's Law at High Pressure and Temperature."

    American Journal of Science 278 (2): 217–43.

Nielsen, R. L., Gallahan, W. E., and Newberger, F., 1992, Experimentally determined

    mineral-melt partition coefficients for Sc, Y and REE for olivine, orthopyroxene,

    pigeonite, magnetite and ilmenite. Contributions to Mineralogy and Petrology,

    110(4), 488–499. https://doi.org/10.1007/BF00344083

Norman, M., Garcia, M.O. and Pietruszka, A.J., 2005, Trace-element distribution

    coefficients for pyroxenes, plagioclase, and olivine in evolved tholeiites from the

    1955 eruption of Kilauea Volcano, Hawai'i, and petrogenesis of differentiated

    rift-zone lavas. American Mineralogist, 90(5-6), pp.888-899.

Okamoto, K., 1979, Geochemical approach on the magmatic differentiation of Asama

    volcano and Cs/Rb ratios of calc-alkaline rocks in island arcs.

Oxford Instruments, 2013, AZtec EDS Software

Paster, T.P., Schauwecker, D.S., and Haskin, L.A., 1974, The behavior of some trace

elements during solidification of the Skaergaard layered series: Geochimica et

Cosmochimica Acta, v. 38, p. 1549–1577, doi:10.1016/0016-7037(74)90174-4.

Philpotts, J.A., and Schnetzler, C.C., 1970, Phenocryst-matrix partition coefficients for K,

Rb, Sr and Ba, with applications to anorthosite and basalt genesis: Geochimica et

Cosmochimica Acta, v. 34, p. 307–322, doi:10.1016/0016-7037(70)90108-0.

Reidel, S.P., Camp, V.E., Tolan, T.L., and Martin, B.S., 2013, The Columbia River flood

basalt province: Stratigraphy, areal extent, volume, and physical volcanology, in

Reidel, S.P., Camp, V.E., Ross, M.E., Wolff, J.A., Martin, B.S., Tolan, T.L, and Wells,

R.E., eds., The Columbia River Flood Basalt Province: Geological Society of

America Special Paper 497, doi:10.1130/2013.2497(01).

Reidel, S.P., and Tolan, T.L., 2013, The Grande Ronde Basalt, Columbia River Basalt

Group, in Reidel, S.P., et al., eds., The Columbia River Flood Basalt Province:

Geological Society of America Special Paper 497, p. 117–153, doi: 10 .1130 /2013

.2497 (05).

Reidel, S. P. 1998, Emplacement of Columbia River flood basalt: Journal of Geophysical

Research, v. 103, issue. B11, p. 27393–27410, doi:10.1029/97JB03671.

Ringwood, A. E., 1970, "Petrogenesis of Apollo 11 Basalts and Implications for Lunar

   Origin." Journal of Geophysical Research 75 (32): 6453–79.

Sales, H.J., 2018, The Wildcat Creek Tuff, Eastern Oregon: Co-eruption of Crystal-poor

   Rhyolite and Fe-rich Andesite with Implication for Mafic Underpinnings to

   Voluminous A-type Rhyolites, [M.S. thesis]: Portland, Oregon, Portland State

   University, 151p.

Starkel, W.S., 2014, Mapping, geologic evolution and petrogenesis of the McDermitt

   caldera center, northern Nevada and southern Oregon, USA [Ph.D. thesis]:

   Pullman, Washington State University, 393 p.

Streck, M.J., Ferns, M.L., and McIntosh, W.C., 2015, Large, persistent rhyolitic magma

   reservoirs above Columbia River Basalt storage sites: The Dinner Creek Tuff

   Eruptive Center, eastern Oregon: Geosphere, v. 11, n. 2, p. 1-10.

Sun, S.S. and McDonough, W.F., 1989, Chemical and isotopic systematics of oceanic

   basalts: implications for mantle composition and processes: Geological Society,

   London, Special Publications, v. 42, p. 313-3445.

Swanson, D.A., Wright, T.L., Hooper, P.R., and Bentley, R.D., 1979a, Revisions in

   Stratigraphic Nomenclature of the Columbia River Basalt Group: U.S. Geological

   Survey Bulletin 1457-G, 59 p.

Vervoort, J.D. and Green, J.C., 1997. Origin of evolved magmas in the Midcontinent rift

system, northeast Minnesota: Nd-isotope evidence for melting of Archean crust.

Canadian Journal of Earth Sciences, 34(4), pp.521-535.

Vranizan, L, Streck, MJ, McIntosh, WC and Sales, H 2019, 'Composition of mafic fiamme

of the rhyolitic Buchanan Tuff, eastern Oregon; understanding magmas that

drive silicic magmatism', *Abstracts with Programs - Geological Society of*

America, vol. 51, no. 4, p. Abstract no. 11-17

Webb, B.M., Streck, M.J., McIntosh, W.C., and Ferns, M.L., 2019. The Littlefield Rhyolite

and associated mafic lavas: Bimodal volcanism of the Columbia River magmatic

province, with constraints on age and storage sites of Grande Ronde Basalt

magmas. *Geosphere*, *15*(1), pp.60-84.

Webb, B.M., 2017, The Littlefield Rhyolite, eastern Oregon: Distinct flow units and their

constraints on age and storage sites of Grande Ronde Basalt magmas [M.S.

thesis]: Portland, Oregon, Portland State University, 164 p., https:// doi .org /10

.15760 /etd .5906 .

Wolff, J.A., and Ramos, F.C., 2013, Source materials for the main phase of the Columbia

River Basalt Group: Geochemical evidence and implications for magma storage

and transport: Geological Society of America Special Paper 497, p. 273-291.

Wolff, J.A., Ramos, F.C., Hart, G.L., Patterson, J.D., and Brandon, A.D., 2008, Columbia River flood basalts from a centralized crustal magmatic system: Nature Geoscience, doi:10.1038/ngeo124.

Wright, T.L., Black, K.N., Swanson, D.A., and O'Hearn, T., 1980, Columbia River Basalt; 1978-1979 sample data and chemical analyses, doi:10.3133/OFR80921.

Wright, T.L., 1979. Major oxide, trace element, and glass chemistry of Columbia River basalt samples collected between 1971 and 1977 (Vol. 79, No. 711). US Geological Survey.

Zimmerman, B.S., 1991, Geology and Geochemistry of Epithermal Gold Mineralization in the Lake Owyhee Volcanic Field–Western Snake River Plain Region of Eastern Oregon and Western Idaho [Ph.D. thesis]: Pullman, Washington, Washington State University, 262 p.

Appendix A: Whole Rock Geochemical Data

Table A-1. XRF and ICP-MS geochemical data.

Sample ID	MAC-17-02	MAC-17-03	MAC-17-04a	MAC-17-05	MAC-17-06
Dataset	Carley, 2017	Carley, 2017	Carley, 2017	Carley, 2017	Carley, 2017
Unit	Fiddler's Hell	Fiddler's Hell	Fiddlers Hell	Fiddler's Hell	Fiddler's Hell
Icelandite Group	Transition	Transition	Group 1 high TiO2	Group 1 high TiO2	Group 1 high TiO2
Quad	Granite Meadows	Ukiah	Sullivan's Gulch	Sullivan's Gulch	Sullivan's Gulch
Easting (m)	354745.94	352029.02	373668.06	378729.88	376393.40
Northing (m)	5013971.89	5012429.15	5003693.36	5000957.13	5005731.80
XRF Normalized Wt. %					
SiO2	55.35	55.75	60.16	59.65	60.10
TiO2	2.24	2.36	1.97	1.96	1.96
Al2O3	13.85	13.61	13.35	13.23	13.33
FeO*	11.77	11.80	10.20	10.78	10.29
MnO	0.21	0.22	0.23	0.28	0.22
MgO	3.65	3.51	1.74	1.72	1.68
CaO	7.79	7.45	5.36	5.35	5.39
Na2O	3.20	3.18	3.52	3.36	3.41
K2O	1.54	1.66	2.68	2.88	2.84
P2O5	0.41	0.476	0.798	0.792	0.784
XRF Trace (ppm)					
Ni	8	9	4	6	3
Cr	9	7	0	1	0
Sc	35	35	26	26	26
V	327	308	51	49	52
Ba	665	723	1117	1247	1027
Rb	39	41	64	64	65
Sr	331	331	325	333	329
Zr	185	195	263	260	263
Y	41	44	60	56	56
Nb	13.1	13.7	18.6	18.1	17.6
Ga	22	22	23	22	23
Cu	18	14	8	11	7
Zn	143	152	155	163	162
Pb	13	14	14	15	15
La	22	30	40	37	37
Ce	54	62	83	78	81
Th	4	7	9	8	8
Nd	28	32	44	44	43
U	2	3	2	4	2

Sample ID	MAC-17-02	MAC-17-03	MAC-17-04a	MAC-17-05	MAC-17-06
Easting (m)	354745.94	352029.02	373668.06	378729.88	376393.40
Northing (m)	5013971.89	5012429.15	5003693.36	5000957.13	5005731.80
Unit	Fiddler's Hell	Fiddler's Hell	Fiddlers Hell	Fiddler's Hell	Fiddler's Hell
ICP-MS Trace (ppm)					
La ppm	24.99	28.27	40.78	39.13	37.92
Ce ppm	51.55	57.86	82.43	81.26	79.59
Pr ppm	6.80	7.72	10.97	10.57	10.37
Nd ppm	29.13	32.81	46.55	44.75	44.07
Sm ppm	7.10	8.06	11.20	10.75	10.69
Eu ppm	2.31	2.55	3.25	3.16	3.12
Gd ppm	7.57	8.40	11.60	11.04	10.81
Tb ppm	1.27	1.40	1.88	1.79	1.75
Dy ppm	7.71	8.60	11.52	10.99	10.59
Ho ppm	1.58	1.74	2.34	2.24	2.16
Er ppm	4.23	4.71	6.31	5.92	5.80
Tm ppm	0.60	0.66	0.88	0.83	0.82
Yb ppm	3.70	4.02	5.37	5.11	5.00
Lu ppm	0.57	0.62	0.84	0.80	0.77
Ba ppm	656	716	1114	1251	1002
Th ppm	4.88	5.08	8.13	8.09	7.94
Nb ppm	12.60	13.48	18.01	17.82	17.47
Y ppm	41.11	44.70	60.86	56.83	55.06
Hf ppm	4.91	5.17	7.04	7.08	6.92
Ta ppm	0.83	0.88	1.17	1.16	1.14
U ppm	1.38	1.48	2.33	2.29	2.25
Pb ppm	12.21	12.82	13.92	14.39	14.36
Rb ppm	38.6	40.8	65.4	64.6	64.1
Cs ppm	1.11	1.24	1.92	1.93	1.94
Sr ppm	337	337	327	337	323
Sc ppm	35.3	35.0	26.7	26.1	26.0
Zr ppm	186	197	268	266	262

Sample ID	MAC-17-08	MAC-17-09	MAC-17-10	MAC-17-11	MAC-17-12
Dataset	Carley, 2017	Carley, 2017	Carley, 2017	Carley, 2017	Carley, 2017
Unit	Fiddler's Hell	Fiddler's Hell	Fiddler's Hell	Fiddler's Hell	Fiddler's Hell
Icelandite Group	Group 1 high TiO2	Group 1 high TiO2	Group 1 high TiO2	Group 1 high TiO2	Group 1 high TiO2
Quad	Kamela SE	Huron	Drumhill Ridge	Drumhill Ridge	Drumhill Ridge
Easting (m)	396454.40	402192.78	404359.81	405109.56	404285.70
Northing (m)	5021717.22	5031704.36	5030322.71	5031080.20	5038708.48
XRF Normalized Wt. %					
SiO2	60.31	60.01	59.82	60.59	59.71
TiO2	1.98	1.98	1.98	1.99	1.95
Al2O3	13.35	13.36	13.37	13.41	13.13
FeO*	10.25	10.28	11.10	9.71	11.08
MnO	0.21	0.23	0.23	0.21	0.21
MgO	1.67	1.73	1.58	1.72	1.71
CaO	5.20	5.41	5.20	5.33	5.31
Na2O	3.50	3.41	3.65	3.49	3.74
K2O	2.73	2.80	2.27	2.75	2.37
P2O5	0.794	0.798	0.785	0.805	0.786
XRF Trace (ppm)					
Ni	3	6	3	3	2
Cr	0	1	0	0	0
Sc	27	26	26	27	27
V	49	49	55	52	48
Ba	1104	1127	1280	1415	1005
Rb	65	65	63	66	61
Sr	320	323	332	339	320
Zr	263	263	260	267	262
Y	57	61	58	63	59
Nb	17.4	18.2	18.1	18.2	17.7
Ga	24	22	22	23	23
Cu	6	9	6	6	7
Zn	173	172	174	170	165
Pb	35	16	15	16	15
La	39	38	38	44	42
Ce	84	86	82	87	82
Th	10	8	9	9	8
Nd	48	47	47	48	46
U	4	3	2	3	4

Sample ID	MAC-17-08	MAC-17-09	MAC-17-10	MAC-17-11	MAC-17-12
Easting (m)	396454.40	402192.78	404359.81	405109.56	404285.70
Northing (m)	5021717.22	5031704.36	5030322.71	5031080.20	5038708.48
Unit	Fiddler's Hell	Fiddler's Hell	Fiddler's Hell	Fiddler's Hell	Fiddler's Hell
ICP-MS Trace (ppm)					
La ppm	39.61	41.11	39.39	43.19	39.58
Ce ppm	80.82	83.08	78.93	83.95	82.04
Pr ppm	10.78	11.13	10.75	11.44	10.82
Nd ppm	46.17	47.47	45.97	48.66	45.78
Sm ppm	11.16	11.36	11.10	11.58	10.94
Eu ppm	3.17	3.22	3.22	3.32	3.16
Gd ppm	11.34	11.65	11.48	11.88	11.27
Tb ppm	1.87	1.93	1.89	1.94	1.83
Dy ppm	11.36	11.66	11.60	11.74	11.13
Ho ppm	2.31	2.39	2.32	2.45	2.29
Er ppm	6.17	6.38	6.17	6.57	6.20
Tm ppm	0.87	0.89	0.87	0.91	0.87
Yb ppm	5.24	5.50	5.45	5.58	5.31
Lu ppm	0.83	0.88	0.84	0.87	0.85
Ba ppm	1114	1120	1244	1404	990
Th ppm	8.16	8.14	7.90	8.24	8.12
Nb ppm	17.67	17.52	17.23	17.82	17.54
Y ppm	58.54	60.95	57.75	63.23	59.98
Hf ppm	7.01	6.99	6.80	7.13	7.04
Ta ppm	1.17	1.17	1.13	1.18	1.17
U ppm	2.31	2.31	2.23	2.33	2.30
Pb ppm	36.26	15.57	13.79	14.77	15.53
Rb ppm	65.4	65.5	62.4	65.4	62.1
Cs ppm	1.89	1.87	1.87	1.92	1.74
Sr ppm	324	322	328	339	324
Sc ppm	27.3	27.1	26.9	27.3	27.1
Zr ppm	266	263	257	269	263

Sample ID	MAC-17-13	MAC-17-14	MAC-17-15	MAC-17-16	MAC-17-18
Dataset	Carley, 2017	Carley, 2017	Carley, 2017	Carley, 2017	Carley, 2017
Unit Icelandite Group	Fiddler's Hell Group 1 high TiO2	Fiddler's Hell Group 1 high TiO2	Fiddler's Hell Transition	Fiddler's Hell Group 1 high TiO2	Fiddler's Hell Group 1 high TiO2
Quad	Drumhill Ridge	Drumhill Ridge	La Grande SE	Glass Hill	Summerville
Easting (m)	403972.31	405079.563	412615.46	415699.62	412329.51
Northing (m)	5039089.03	5037800.146	5023348.85	5003692.37	5038786.97

XRF Normalized Wt. %

SiO2	59.57	61.02	54.22	59.96	59.51
TiO2	1.96	2.01	2.14	1.95	1.97
Al2O3	13.21	13.56	13.65	13.19	13.31
FeO*	11.17	8.84	13.19	11.25	11.02
MnO	0.22	0.22	0.23	0.21	0.22
MgO	1.75	1.74	3.83	1.55	1.74
CaO	5.34	5.43	7.82	4.96	5.34
Na2O	3.60	3.45	3.19	3.80	3.57
K2O	2.40	2.91	1.34	2.35	2.54
P2O5	0.783	0.82	0.38	0.788	0.793

XRF Trace (ppm)

Ni	3	3	12	4	3
Cr	0	0	3	0	0
Sc	27	27	37	26	26
V	54	53	397	52	51
Ba	989	1297	606	937	942
Rb	64	69	35	69	62
Sr	319	343	347	313	316
Zr	262	267	169	261	263
Y	60	61	39	58	60
Nb	18.3	18.0	11.1	18.0	17.6
Ga	22	24	22	22	23
Cu	6	8	30	8	7
Zn	157	171	143	156	166
Pb	26	145	10	14	17
La	42	38	24	40	39
Ce	81	81	52	80	83
Th	9	9	6	8	8
Nd	46	46	27	45	46
U	3	3	2	3	2

Sample ID	MAC-17-13	MAC-17-14	MAC-17-15	MAC-17-16	MAC-17-18
Easting (m)	403972.31	405079.563	412615.46	415699.62	412329.51
Northing (m)	5039089.03	5037800.146	5023348.85	5003692.37	5038786.97
Unit	Fiddler's Hell	Fiddler's Hell	Fiddler's Hell	Fiddler's Hell	Fiddler's Hell
ICP-MS Trace (ppm)					
La ppm	42.21	40.81	23.35	38.85	41.13
Ce ppm	82.86	84.95	48.77	78.81	84.29
Pr ppm	11.21	11.00	6.57	10.73	11.07
Nd ppm	47.26	46.89	28.45	46.07	47.02
Sm ppm	11.25	11.09	6.96	11.13	11.49
Eu ppm	3.22	3.25	2.20	3.22	3.25
Gd ppm	11.55	11.53	7.32	11.50	11.55
Tb ppm	1.88	1.90	1.22	1.88	1.89
Dy ppm	11.60	11.50	7.64	11.42	11.49
Ho ppm	2.35	2.34	1.55	2.30	2.38
Er ppm	6.31	6.37	4.28	6.18	6.39
Tm ppm	0.88	0.89	0.61	0.87	0.89
Yb ppm	5.33	5.50	3.76	5.29	5.48
Lu ppm	0.85	0.85	0.58	0.82	0.86
Ba ppm	970	1299	598	935	931
Th ppm	8.12	8.36	3.99	8.11	8.18
Nb ppm	17.54	17.96	11.72	17.60	17.78
Y ppm	60.40	60.94	39.69	58.44	60.58
Hf ppm	6.97	7.24	4.64	7.01	7.08
Ta ppm	1.15	1.19	0.75	1.16	1.18
U ppm	2.31	2.41	1.14	2.29	2.41
Pb ppm	25.21	138.59	11.08	14.68	16.09
Rb ppm	64.0	69.2	34.49	68.2	61.9
Cs ppm	1.89	1.98	0.93	1.84	1.82
Sr ppm	321	344	355	317	319
Sc ppm	26.6	27.5	37.86	27.0	26.9
Zr ppm	264	271	171	263	268

Sample ID	MAC-17-22a	MAC-17-25	MAC-17-26	MAC-17-29	MAC-17-32
Dataset	Carley, 2017	Carley, 2017	Carley, 2017	Carley, 2017	Carley, 2017
Unit	Fiddler's Hell	Fiddler's Hell	Fiddler's Hell	Fiddler's Hell	Hunter Creek
Icelandite Group	Transition	Transition	Transition	Group 1 high TiO2	Group 1 low TiO2
Quad	Summerville	Medical Springs	McIntyre Creek	Meacham Lake	Namorf
Easting (m)	414302.54	445533.44	385608.08	389606.53	441257.00
Northing (m)	5035266.52	4994587.50	5019791.54	5029335.61	4847697.51
XRF Normalized Wt. %					
SiO2	55.87	55.72	56.48	60.00	62.66
TiO2	2.38	2.26	2.23	1.96	1.22
Al2O3	13.32	13.70	13.76	13.21	13.54
FeO*	13.35	12.44	12.02	10.63	9.84
MnO	0.22	0.21	0.18	0.27	0.25
MgO	2.81	3.15	2.86	1.74	0.75
CaO	6.15	6.83	6.71	5.35	4.60
Na2O	3.52	3.51	3.51	3.50	3.56
K2O	1.77	1.75	1.80	2.55	3.31
P2O5	0.61	0.44	0.447	0.799	0.274
XRF Trace (ppm)					
Ni	5	11	9	1	2
Cr	0	0	3	0	3
Sc	32	31	32	26	29
V	235	323	318	50	22
Ba	724	729	750	978	1138
Rb	46	46	51	66	82
Sr	322	320	326	327	311
Zr	216	203	204	263	296
Y	47	42	42	59	57
Nb	14.9	13.4	13.8	18.5	20.8
Ga	22	21	21	23	22
Cu	14	22	20	6	11
Zn	161	145	152	147	165
Pb	17	13	17	11	15
La	29	27	29	37	37
Ce	66	55	61	85	86
Th	7	6	7	8	9
Nd	35	29	31	46	45
U	2	2	3	3	4

Sample ID	MAC-17-22a	MAC-17-25	MAC-17-26	MAC-17-29	MAC-17-32
Easting (m)	414302.54	445533.44	385608.08	389606.53	441257.00
Northing (m)	5035266.52	4994587.50	5019791.54	5029335.61	4847697.51
Unit	Fiddler's Hell	Fiddler's Hell	Fiddler's Hell	Fiddler's Hell	Hunter Creek
ICP-MS Trace (ppm)					
La ppm	30.26	27.50	28.23	40.02	39.41
Ce ppm	64.15	57.95	57.16	83.06	83.09
Pr ppm	8.46	7.57	7.80	10.80	10.89
Nd ppm	36.49	32.50	32.99	45.92	46.09
Sm ppm	8.93	7.78	7.90	10.98	11.17
Eu ppm	2.72	2.35	2.34	3.19	3.53
Gd ppm	9.13	8.05	8.25	11.33	11.05
Tb ppm	1.52	1.33	1.36	1.85	1.85
Dy ppm	9.32	8.16	8.17	11.37	11.27
Ho ppm	1.87	1.67	1.66	2.35	2.32
Er ppm	5.05	4.49	4.56	6.26	6.32
Tm ppm	0.72	0.63	0.64	0.87	0.92
Yb ppm	4.43	3.93	3.87	5.41	5.79
Lu ppm	0.72	0.61	0.60	0.85	0.97
Ba ppm	717	721	740	985	1155
Th ppm	5.99	5.57	5.54	8.26	8.43
Nb ppm	14.87	13.39	13.44	17.74	20.61
Y ppm	46.95	41.63	42.25	60.60	58.18
Hf ppm	5.85	5.45	5.47	7.13	8.01
Ta ppm	0.97	0.88	0.88	1.17	1.26
U ppm	1.70	1.65	1.63	2.34	2.57
Pb ppm	16.27	12.02	15.87	12.27	12.94
Rb ppm	46.3	45.3	49.3	66.3	83.8
Cs ppm	1.01	1.07	1.58	1.94	2.25
Sr ppm	326	321	325	331	315
Sc ppm	33.3	32.2	31.8	27.1	31.7
Zr ppm	220	204	204	266	301

Sample ID	MAC-17-33	MAC-17-34b	MAC-17-37	U34	U38
Dataset	Carley, 2017	Carley, 2017	Carley, 2017	Streck, 2013	Streck, 2013
Unit	Hunter Creek	Hunter Creek	Fiddler's Hell	N/S of Ironside	N/S of Ironside
Icelandite Group	Low SIO2	Transition	Transition	Group 2 low TiO2	Group 2 low TiO2
Quad	Westfall	Jonesboro	Tucker Flat	Eldorado Pass	Rastus Mountain
Easting (m)	449720.11	423693.99	414556.41	419965.06	405411.75
Northing (m)	4870183.00	4850860.25	4995044.26	4901556.78	4910815.25
XRF Normalized Wt. %					
SiO2	57.15	56.13	54.55	61.45	60.86
TiO2	2.39	2.41	2.34	1.29	1.38
Al2O3	13.41	13.71	14.08	14.85	14.83
FeO*	11.38	11.95	11.43	9.97	9.33
MnO	0.53	0.20	0.19	0.14	0.20
MgO	2.43	3.12	4.03	1.06	1.45
CaO	6.47	7.00	8.18	4.52	5.08
Na2O	3.07	3.04	3.05	4.07	3.62
K2O	2.40	1.99	1.74	2.11	2.70
P2O5	0.764	0.453	0.40	0.527	0.543
XRF Trace (ppm)					
Ni	2	6	25	2	3
Cr	0	6	36	1	1
Sc	30	32	31	23	21
V	167	360	313	47	115
Ba	979	946	569	890	1038
Rb	63	50	41	48	60
Sr	342	344	349	300	305
Zr	232	219	191	207	202
Y	49	42	34	44	49
Nb	16.9	14.7	12.4	12.0	10.1
Ga	22	22	20	23	23
Cu	7	12	66	6	6
Zn	153	141	125	177	207
Pb	11	9	9	8	9
La	33	31	21	21	22
Ce	78	62	49	49	56
Th	7	7	6	3	5
Nd	40	32	30	32	31
U	2	3	3	2	4

Sample ID	MAC-17-33	MAC-17-34b	MAC-17-37	U34	U38
Easting (m)	449720.11	423693.99	414556.41	419965.06	405411.75
Northing (m)	4870183.00	4850860.25	4995044.26	4901556.78	4910815.25
Unit	Hunter Creek	Hunter Creek	Fiddler's Hell	N/S of Ironside	N/S of Ironside
ICP-MS Trace (ppm)					
La ppm	34.67	30.34	22.74	22.23	23.42
Ce ppm	73.43	62.84	49.18	46.76	49.81
Pr ppm	9.62	8.11	6.57	7.07	6.79
Nd ppm	40.93	34.06	28.63	30.90	28.95
Sm ppm	9.77	8.07	7.20	7.60	7.15
Eu ppm	2.95	2.37	2.12	2.18	1.69
Gd ppm	9.87	8.27	7.27	7.79	7.73
Tb ppm	1.59	1.38	1.20	1.30	1.34
Dy ppm	9.66	8.35	7.11	8.07	8.47
Ho ppm	1.96	1.71	1.42	1.67	1.80
Er ppm	5.16	4.66	3.75	4.51	5.04
Tm ppm	0.72	0.65	0.53	0.66	0.75
Yb ppm	4.44	4.05	3.19	4.16	4.74
Lu ppm	0.71	0.64	0.49	0.65	0.76
Ba ppm	977	942	559	879	1027
Th ppm	6.84	6.31	4.67	4.14	5.07
Nb ppm	16.49	14.96	12.41	11.28	9.33
Y ppm	49.28	43.21	35.38	43.18	48.75
Hf ppm	6.15	5.84	5.15	5.57	5.51
Ta ppm	1.07	0.99	0.84	0.69	0.61
U ppm	2.01	1.82	1.47	2.02	2.54
Pb ppm	10.88	9.88	9.02	8.21	8.48
Rb ppm	62.3	49.5	40.63	46.8	57.5
Cs ppm	1.81	1.50	1.38	2.50	2.30
Sr ppm	344	348	353	305	311
Sc ppm	31.5	32.3	31.41	26.7	24.3
Zr ppm	235	222	193	211	207

Sample ID	MS-14-17	MS-15-19C	MS-15-23A	MS-15-23B	MS-15-23C
Dataset	Streck, 2014	Streck, 2014	Streck, 2014	Streck, 2014	Streck, 2014
Unit	DIT dacite flow?	thin Buchanan welded fall out tuff	unit 1 mafic pyroclast	unit 2 mafic pyroclast	unit 3 mafic pyroclastic, GR2
Icelandite Group	Group 2 high TiO2	Group 2 high TiO2	Group 2 high TiO2	Group 2 high TiO2	Low SIO2
Quad	Diamond Swamp	Jump-Off Joe Mountain	Jump-Off Joe Mountain	Jump-Off Joe Mountain	Jump-Off Joe Mountain
Easting (m)	352425.23	371204.76	353465.80	353465.80	353466.00
Northing (m)	4874835.48	4835599.21	4874443.83	4874443.83	4874453.05
XRF Normalized Wt. %					
SiO2	59.58	58.98	59.59	59.78	57.91
TiO2	1.93	1.96	1.86	1.87	1.84
Al2O3	15.25	14.96	15.30	15.00	16.09
FeO*	9.07	8.89	8.92	9.10	9.36
MnO	0.17	0.21	0.18	0.17	0.19
MgO	1.84	2.52	1.79	1.93	1.51
CaO	5.10	5.64	5.38	5.19	5.77
Na2O	4.27	3.69	3.87	4.25	4.32
K2O	1.91	2.23	1.99	1.81	1.40
P2O5	0.868	0.925	1.118	0.879	1.623
XRF Trace (ppm)					
Ni	5	4	5	7	8
Cr	12	0	1	0	0
Sc	24	24	23	24	24
V	136	142	114	120	66
Ba	998	1065	1005	1072	1106
Rb	37	38	45	39	12
Sr	409	390	407	416	411
Zr	197	191	196	192	208
Y	47	45	43	42	52
Nb	14.4	13.2	13.4	13.5	15.2
Ga	20	19	19	19	20
Cu	12	6	8	7	10
Zn	145	141	124	133	123
Pb	9	8	6	8	7
La	31	28	27	28	31
Ce	59	56	61	59	67
Th	4	5	4	3	4
Nd	39	35	36	33	40
U	1	1	4	3	3

Sample ID	MS-14-17	MS-15-19C	MS-15-23A	MS-15-23B	MS-15-23C
Easting (m)	352425.23	371204.76	353465.80	353465.80	353466.00
Northing (m)	4874835.48	4835599.21	4874443.83	4874443.83	4874453.05
Unit	DIT dacite flow?	thin Buchanan welded fall-out tuff	unit 1 mafic pyroclastic	unit 2 mafic pyroclastic	unit 3 mafic pyroclastic, GR2
ICP-MS Trace (ppm)					
La ppm	29.62	28.63	28.83	27.82	34.40
Ce ppm	60.43	62.07	63.08	61.22	65.75
Pr ppm	8.88	8.44	8.58	8.41	9.77
Nd ppm	38.26	36.98	36.77	36.44	41.49
Sm ppm	9.18	8.70	8.67	8.61	9.66
Eu ppm	2.93	2.93	2.84	2.88	3.00
Gd ppm	9.50	8.85	8.65	8.49	9.52
Tb ppm	1.51	1.42	1.39	1.38	1.56
Dy ppm	9.10	8.54	8.43	8.47	9.49
Ho ppm	1.86	1.70	1.71	1.69	1.97
Er ppm	5.04	4.63	4.62	4.53	5.30
Tm ppm	0.72	0.67	0.65	0.63	0.75
Yb ppm	4.52	4.12	4.07	3.87	4.72
Lu ppm	0.70	0.65	0.65	0.62	0.76
Ba ppm	1000	1067	1029	1094	1148
Th ppm	3.88	3.63	4.04	3.80	4.16
Nb ppm	13.28	13.59	13.88	13.60	14.88
Y ppm	46.92	45.07	44.03	43.44	52.54
Hf ppm	4.98	4.97	5.22	5.02	5.53
Ta ppm	0.86	0.91	0.92	0.84	0.91
U ppm	1.89	1.66	2.37	1.74	3.53
Pb ppm	7.73	7.62	7.21	7.64	5.87
Rb ppm	35.8	37.2	44.7	37.9	10.8
Cs ppm	1.81	1.80	2.03	2.43	0.40
Sr ppm	410	396	417	431	428
Sc ppm	24.6	24.0	24.0	25.2	25.0
Zr ppm	193	196	202	198	214

Sample ID	MS-15-31	MS-12-34	BW-15-31	BW-15-35	BW-14-37A
Dataset	Streck, 2014	Streck, 2016	Webb, 2015	Webb, 2015	Webb, 2016
Unit	BCT mafic scoria	Hunter at Neal	GR2		Alder Creek Icelandite
Icelandite Group	Group 2 low TiO2	Group 1 low TiO2	Low SIO2	Transition group	Group 1 low TiO2
Quad	Westfall	Hope Butte	Namorf	Namorf	Alder Creek
Easting (m)	441001.68	463326.29	440006.9997	440602.35	433140.00
Northing (m)	4871599.38	4874738.45	4826016.156	4846481.51	4826063.21
XRF Normalized Wt. %					
SiO2	60.30	60.46	57.43	56.81	63.28
TiO2	1.50	1.56	2.30	2.36	1.23
Al2O3	14.79	12.87	13.75	14.54	13.31
FeO*	10.02	11.76	10.87	11.21	9.92
MnO	0.18	0.26	0.26	0.17	0.20
MgO	1.52	1.32	2.86	2.73	0.82
CaO	5.33	5.04	6.39	6.40	4.09
Na2O	3.53	3.49	3.30	3.72	3.76
K2O	2.20	2.65	2.28	1.68	3.03
P2O5	0.620	0.589	0.560	0.384	0.367
XRF Trace (ppm)					
Ni	5	4	8	3	2
Cr	0	0	0	0	0
Sc	29	26	30	32	23
V	65	23	228	323	5
Ba	834	1104	841	703	1198
Rb	46	82	60	38	81
Sr	327	310	342	357	280
Zr	176	293	243	219	357
Y	48	60	48	37	67
Nb	10.0	20.8	15.1	13.9	24.3
Ga	19	22	22	22	23
Cu	10	8	22	11	5
Zn	190	165	137	132	156
Pb	15	13	10	11	14
La	24	44	28	25	45
Ce	53	96	65	56	95
Th	5	8	6	5	10
Nd	33	52	38	31	50
U	2	3	1	3	3

Sample ID	MS-15-31	MS-12--34	BW-15-31	BW-15-35	BW-14-37A
Easting (m)	441001.68	463326.29	440006.9997	440602.35	433140.00
Northing (m)	4871599.38	4874738.45	4826016.156	4846481.51	4826063.21
Unit	BCT mafic scoria	Hunter at Neal	GR2		Alder Creek Icelandite
ICP-MS Trace (ppm)					
La ppm	23.81	42.40	24.30	25.25	46.65
Ce ppm	52.36	92.44	52.92	54.70	94.45
Pr ppm	7.32	11.99	7.00	7.39	12.54
Nd ppm	31.54	50.12	30.23	31.88	51.72
Sm ppm	8.09	11.61	7.58	7.82	12.06
Eu ppm	2.28	3.49	2.36	2.41	3.38
Gd ppm	8.39	11.39	7.69	7.91	12.26
Tb ppm	1.46	1.87	1.28	1.30	2.03
Dy ppm	9.18	11.50	7.68	7.78	12.43
Ho ppm	1.90	2.37	1.56	1.54	2.60
Er ppm	5.26	6.46	4.17	4.00	7.04
Tm ppm	0.77	0.90	0.59	0.57	1.01
Yb ppm	4.86	5.68	3.58	3.53	6.24
Lu ppm	0.80	0.90	0.57	0.54	0.97
Ba ppm	842	1091	691.00	700	1204
Th ppm	4.39	8.35	4.80	5.02	9.76
Nb ppm	10.36	20.11	13.00	13.36	22.77
Y ppm	49.62	59.51	38.50	36.74	67.67
Hf ppm	4.90	7.66	5.68	5.85	9.20
Ta ppm	0.63	1.27	0.89	0.89	1.43
U ppm	2.36	2.47	1.44	1.70	2.80
Pb ppm	14.86	12.30	8.16	10.03	14.31
Rb ppm	46.2	80.3	41.36	37.2	79.5
Cs ppm	2.02	2.16	2.24	1.33	2.57
Sr ppm	341	317	349.00	358	286
Sc ppm	29.3	25.7	30.93	32.0	23.1
Zr ppm	183	290	214.00	220	349

Sample ID	BW-14-37B	MC-15-16	MC-45-16	MC-69-16	MC-94-16
Dataset	Webb, 2016	Cruz, 2016	Cruz, 2017	Cruz, 2017	Cruz, 2017
Unit	Alder Creek Icelandite		icelandite (DIT4)	icelandite (DIT4)	Hunter Creek
Icelandite Group	Group 1 low TiO2	Group 2 low TiO2	Group 2 low TiO2	Group 2 low TiO2	Group 2 low TiO2
Quad	Alder Creek	Castle Rock	Castle Rock	Castle Rock	Eldorado Pass
Easting (m)	433167.00	407222.62	406451.31	401283.06	418812.57
Northing (m)	4826016.21	4873690.51	4879233.75	4880231.16	4900676.68
XRF Normalized Wt. %					
SiO2	63.13	63.20	61.36	62.42	59.93
TiO2	1.19	1.08	1.28	1.46	1.49
Al2O3	13.15	15.13	15.10	14.64	14.57
FeO*	10.20	7.96	10.54	10.36	10.37
MnO	0.21	0.13	0.18	0.16	0.19
MgO	0.84	1.24	2.54	2.76	1.62
CaO	3.99	4.35	5.16	4.61	5.12
Na2O	4.05	3.85	2.12	1.49	4.05
K2O	2.87	2.66	1.45	1.70	2.01
P2O5	0.362	0.402	0.269	0.405	0.653
XRF Trace (ppm)					
Ni	0	3	11	3	2
Cr	0	1	10	0	0
Sc	22	17	27	22	24
V	5	77	182	143	80
Ba	1189	1004	936	822	889
Rb	81	61	29	35	46
Sr	270	297	242	230	310
Zr	356	210	154	185	192
Y	62	45	49	46	51
Nb	24.2	9.8	7.4	9.9	11.0
Ga	23	21	19	18	21
Cu	4	5	15	7	6
Zn	159	181	129	177	174
Pb	14	12	7	10	8
La	41	23	20	20	27
Ce	93	54	36	44	52
Th	10	5	4	4	4
Nd	49	30	24	27	32
U	4	3	2	1	3

Sample ID	BW-14-37B	MC-15-16	MC-45-16	MC-69-16	MC-94-16
Easting (m)	433167.00	407222.62	406451.31	401283.06	418812.57
Northing (m)	4826016.21	4873690.51	4879233.75	4880231.16	4900676.68
Unit	Alder Creek Icelandite		icelandite (DIT4)	icelandite (DIT4)	Hunter Creek
ICP-MS Trace (ppm)					
La ppm	46.34	25.10	20.06	21.97	24.46
Ce ppm	96.52	51.67	38.26	44.48	53.02
Pr ppm	12.38	7.00	5.63	6.34	7.55
Nd ppm	51.07	29.59	23.97	26.97	33.21
Sm ppm	11.96	7.09	5.92	6.57	8.31
Eu ppm	3.45	1.65	1.64	1.96	2.35
Gd ppm	11.64	7.32	6.67	7.28	9.04
Tb ppm	1.95	1.26	1.22	1.28	1.54
Dy ppm	11.99	7.97	8.12	8.28	9.62
Ho ppm	2.45	1.70	1.77	1.79	2.01
Er ppm	6.56	4.89	5.11	5.13	5.48
Tm ppm	0.97	0.70	0.76	0.75	0.81
Yb ppm	5.99	4.49	4.83	4.83	5.01
Lu ppm	0.97	0.71	0.80	0.80	0.80
Ba ppm	1199	1010	950	832	889
Th ppm	9.83	5.35	2.95	3.74	3.99
Nb ppm	23.38	9.29	8.55	9.88	11.13
Y ppm	61.63	44.71	49.46	47.15	51.92
Hf ppm	9.12	5.59	4.38	5.12	5.46
Ta ppm	1.48	0.59	0.57	0.64	0.74
U ppm	2.79	2.52	1.29	1.74	2.01
Pb ppm	14.49	10.81	6.68	8.73	8.84
Rb ppm	78.7	60.0	28.7	35.0	47.3
Cs ppm	1.17	2.35	1.21	4.93	2.45
Sr ppm	280	297	247	233	318
Sc ppm	23.5	17.2	28.0	21.4	25.2
Zr ppm	356	210	161	193	202

Sample ID	MC-98-16	MC-100-16	MC-106-16	MC3C	MC13C
Dataset	Cruz, 2016	Cruz, 2017	Cruz, 2017	Cruz, 2017	Cruz, 2017
Unit		Hunter Creek	Hunter Creek	Hunter Creek	Hunter Creek
Icelandite Group	Group 2 low TiO2	Group 2 low TiO2	Group 2 low TiO2	Group 2 low TiO2	Group 2 low TiO2
Quad	Rastus Mountain	Eldorado Pass	Rastus Mountain	Clevenger Butte	Rastus Mountain
Easting (m)	409980.37	410363.82	409638.45	409254.51	407381.59
Northing (m)	4902902.89	4902342.16	4909351.14	4899480.09	4900317.29
XRF Normalized Wt. %					
SiO2	62.23	60.58	62.02	59.42	60.60
TiO2	1.08	1.32	1.44	1.42	1.24
Al2O3	14.08	14.56	15.45	14.51	14.36
FeO*	9.84	10.25	7.81	10.42	10.29
MnO	0.20	0.20	0.14	0.20	0.21
MgO	1.15	1.47	1.39	1.92	1.46
CaO	4.73	4.84	4.98	5.51	5.11
Na2O	4.01	4.03	3.74	4.00	4.22
K2O	2.26	2.23	2.52	1.95	2.00
P2O5	0.421	0.516	0.509	0.658	0.520
XRF Trace (ppm)					
Ni	2	4	2	6	4
Cr	0	2	0	0	0
Sc	28	30	21	30	32
V	35	67	113	63	46
Ba	873	900	1024	779	824
Rb	47	52	59	44	47
Sr	277	299	323	310	300
Zr	208	192	208	178	192
Y	48	47	52	47	47
Nb	10.1	10.7	10.0	10.1	9.9
Ga	20	20	24	18	20
Cu	4	10	6	8	6
Zn	167	179	223	165	173
Pb	11	9	9	7	8
La	24	24	23	22	26
Ce	58	54	56	52	55
Th	5	5	5	4	4
Nd	32	30	33	31	33
U	2	4	3	1	3

Sample ID	MS-98-16	MC-100-16	MC-106-16	MC3C	MC13C
Easting (m)	409980.37	410363.82	409638.45	409254.51	407381.59
Northing (m)	4902902.89	4902342.16	4909351.14	4899480.09	4900317.29
Unit		Hunter Creek	Hunter Creek	Hunter Creek	Hunter Creek
ICP-MS Trace (ppm)					
La ppm	23.96	23.95	26.23	23.24	23.45
Ce ppm	52.65	52.57	53.39	51.23	52.25
Pr ppm	7.19	7.20	7.56	7.16	7.19
Nd ppm	31.38	31.43	32.42	31.41	31.24
Sm ppm	7.85	7.95	8.11	7.96	7.88
Eu ppm	2.15	2.15	1.86	2.23	2.23
Gd ppm	8.19	8.26	8.57	8.40	8.25
Tb ppm	1.40	1.39	1.49	1.38	1.41
Dy ppm	8.73	8.84	9.43	8.84	8.85
Ho ppm	1.87	1.85	2.01	1.84	1.83
Er ppm	5.15	5.06	5.60	4.97	5.01
Tm ppm	0.76	0.74	0.81	0.71	0.71
Yb ppm	4.77	4.66	5.10	4.42	4.67
Lu ppm	0.79	0.74	0.83	0.72	0.73
Ba ppm	872	919	1040	765	824
Th ppm	4.67	4.56	5.34	4.07	4.29
Nb ppm	10.28	10.41	9.76	9.45	10.11
Y ppm	47.54	47.63	52.21	46.87	46.87
Hf ppm	5.48	5.34	5.77	4.90	5.19
Ta ppm	0.65	0.70	0.67	0.62	0.65
U ppm	2.25	2.27	2.71	1.95	2.10
Pb ppm	9.45	8.45	8.77	7.43	8.03
Rb ppm	47.1	52.3	58.7	43.7	45.2
Cs ppm	2.50	2.37	2.38	1.95	2.10
Sr ppm	275	305	328	315	304
Sc ppm	28.8	30.8	22.1	28.5	32.8
Zr ppm	208	199	217	180	195

Sample ID	MC25A	MC43A
Dataset	Cruz, 2017	Cruz, 2017
Unit	Hunter Creek	Hunter Creek
Icelandite Group	Group 2 high TiO2	Group 2 high TiO2
Quad	Castle Rock	Castle Rock
Easting (m)	405873.30	405271.41
Northing (m)	4884196.71	4881305.80

XRF Normalized Wt. %

SiO2	59.32	58.79
TiO2	1.77	1.81
Al2O3	15.47	15.47
FeO*	8.17	9.61
MnO	0.17	0.15
MgO	2.51	1.75
CaO	5.96	5.61
Na2O	3.79	4.30
K2O	2.09	1.73
P2O5	0.765	0.785

XRF Trace (ppm)

Ni	2	4
Cr	0	0
Sc	24	25
V	132	140
Ba	896	715
Rb	35	36
Sr	358	354
Zr	194	186
Y	53	50
Nb	11.5	11.0
Ga	19	20
Cu	4	5
Zn	158	159
Pb	8	7
La	23	25
Ce	48	53
Th	3	4
Nd	33	36
U	2	2

| Sample ID	MC25A	MC43A
Easting (m)	405873.30	405271.41
Northing (m)	4884196.71	4881305.80
Unit	Hunter Creek	Hunter Creek
ICP-MS Trace (ppm)		
La ppm	25.14	25.57
Ce ppm	53.26	51.23
Pr ppm	7.78	8.11
Nd ppm	34.14	35.99
Sm ppm	8.54	8.92
Eu ppm	2.45	2.59
Gd ppm	9.26	9.69
Tb ppm	1.54	1.60
Dy ppm	10.00	9.95
Ho ppm	2.05	2.03
Er ppm	5.46	5.45
Tm ppm	0.79	0.79
Yb ppm	4.94	4.85
Lu ppm	0.78	0.77
Ba ppm	901	711
Th ppm	3.34	3.20
Nb ppm	11.29	11.00
Y ppm	53.43	50.10
Hf ppm	5.22	5.07
Ta ppm	0.72	0.71
U ppm	1.55	1.47
Pb ppm	6.95	6.73
Rb ppm	33.6	34.3
Cs ppm	1.42	1.63
Sr ppm	356	353
Sc ppm	23.4	23.7
Zr ppm	198	191

Appendix B: SEM-EDS Data
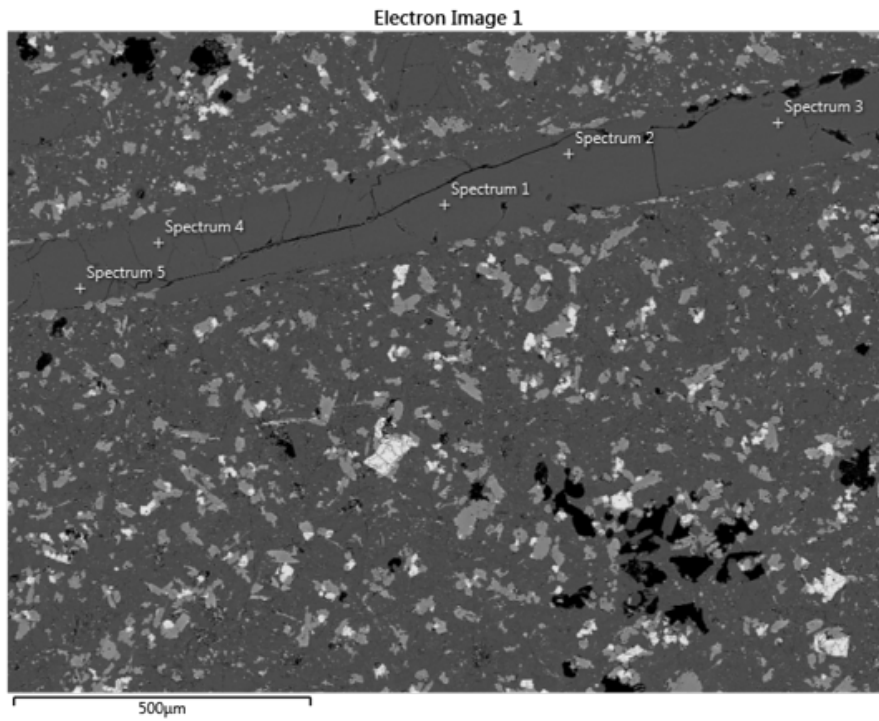
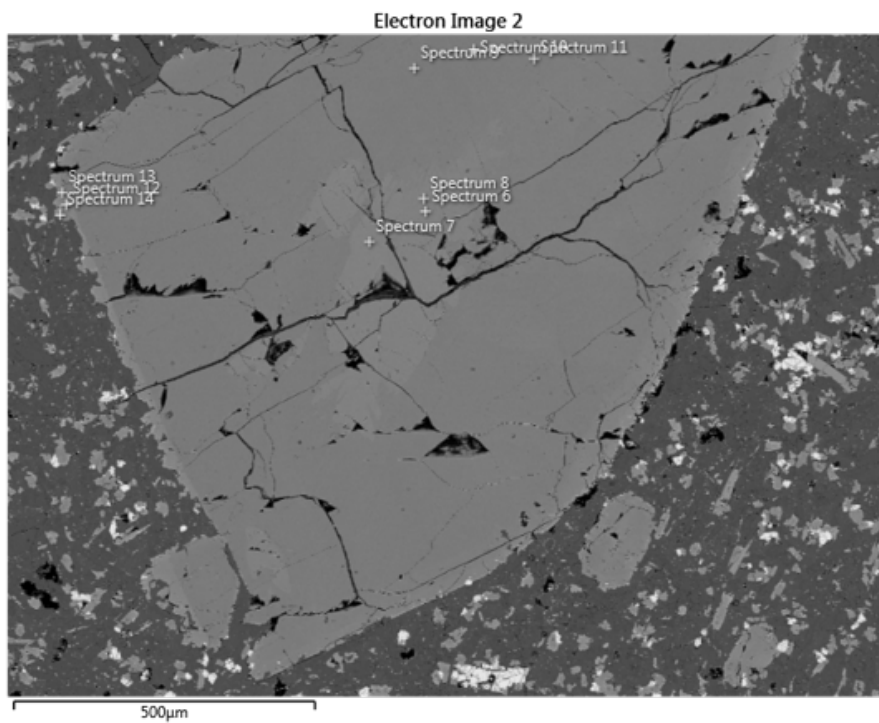**Figure B-1.** Electron images of site 1 of sample MAC-17-04a.

Figure B-2. Electron images of site 2 of sample MAC-17-04a.
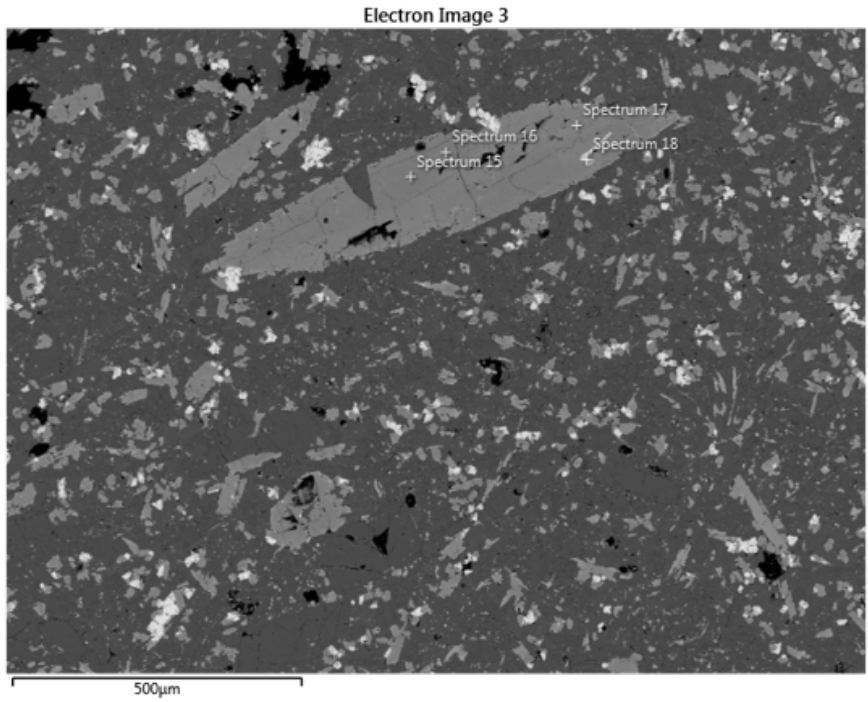
Figure B-3 Electron images of site 3 of sample MAC-17-04a.
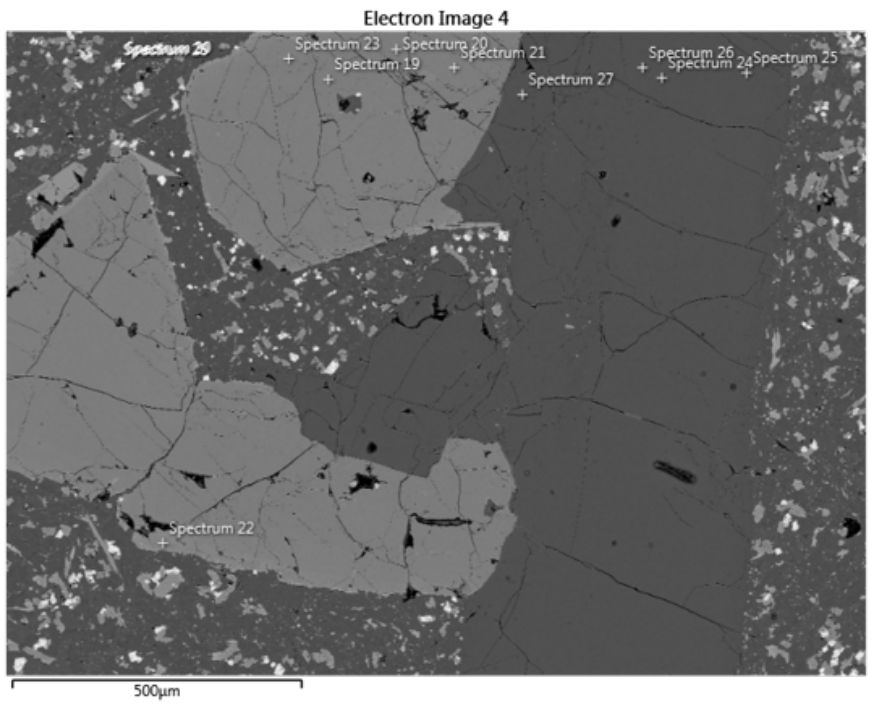

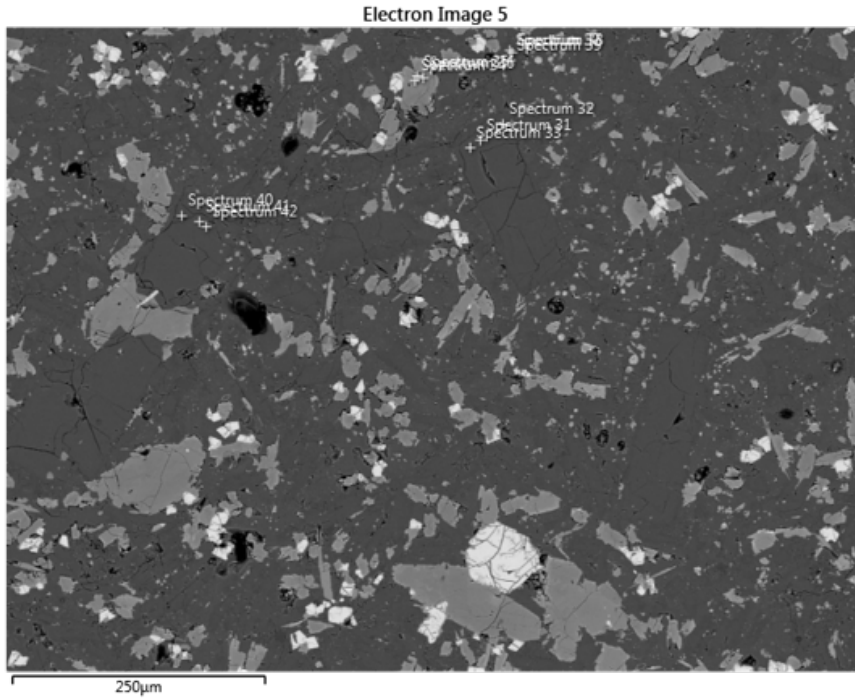**Figure B-4.** Electron images of site 4 of sample MAC-17-04a.

Figure B-5. Electron images of site 5 of sample MAC-17-04a.

Table B-1. Selected EDS spectra for sites 1-5 of MAC-17-04a.

MAC 17-04a	SiO$_2$	TiO$_2$	Al$_2$O$_3$	FeO	MnO	MgO	CaO	Na$_2$O	K$_2$O	P$_2$O$_5$	Total	Phase
Spectrum 1	55.32		27.17	0.35			9.53	5.38	0.22		97.96	Plagioclase
Spectrum 2	55.09		27.21	0.60			9.79	5.12	0.30		98.12	Plagioclase
Spectrum 3	54.62		26.92	0.59			9.68	5.27	0.30		97.39	Plagioclase
Spectrum 4	55.11		26.85	0.49			9.77	5.38	0.35		97.94	Plagioclase
Spectrum 5	55.43		26.68	0.71			9.50	5.55	0.27		98.14	Plagioclase
Spectrum 8	49.74	0.50	1.00	23.05	0.71	15.47	6.77				97.25	Pyroxene
Spectrum 11	49.83	0.82	1.70	16.02	0.59	12.82	16.22	0.32			98.31	Pyroxene
Spectrum 13	49.31	0.53	0.81	26.44	0.88	14.48	5.02	0.22			97.69	Pyroxene
Spectrum 17	48.58	0.73	1.51	21.77	0.63	13.02	11.07	0.24			97.56	Pyroxene
Spectrum 20	50.49	0.68	1.51	15.57	0.67	12.88	16.47	0.26			98.53	Pyroxene
Spectrum 23	49.97	0.75	1.40	17.38	0.59	13.40	14.27	0.32			98.09	Pyroxene
Spectrum 25	55.30		26.75	0.46			9.70	5.43	0.31		97.96	Plagioclase
Spectrum 27	55.32		27.15	0.51			9.70	5.31	0.34		98.33	Plagioclase
Spectrum 28	48.54	0.58	1.04	29.09	0.99	9.54	9.07	0.32			99.17	Pyroxene
Spectrum 32	56.24		26.04	0.64			8.48	5.98	0.41		97.80	Plagioclase
Spectrum 34	49.10	0.67	0.94	27.56	1.03	13.83	4.46				97.59	Pyroxene
Spectrum 38	57.55	0.38	24.68	0.81			7.21	6.66	0.55		97.84	Plagioclase
Spectrum 42	56.26		26.06	0.67			8.42	5.85	0.42		97.68	Plagioclase

Figure B-6. Electron images of site 1 of sample MAC-17-08.

Figure B-7. Electron images of site 2 of sample MAC-17-08.

Figure B-8. Electron images of site 3 of sample MAC-17-08.

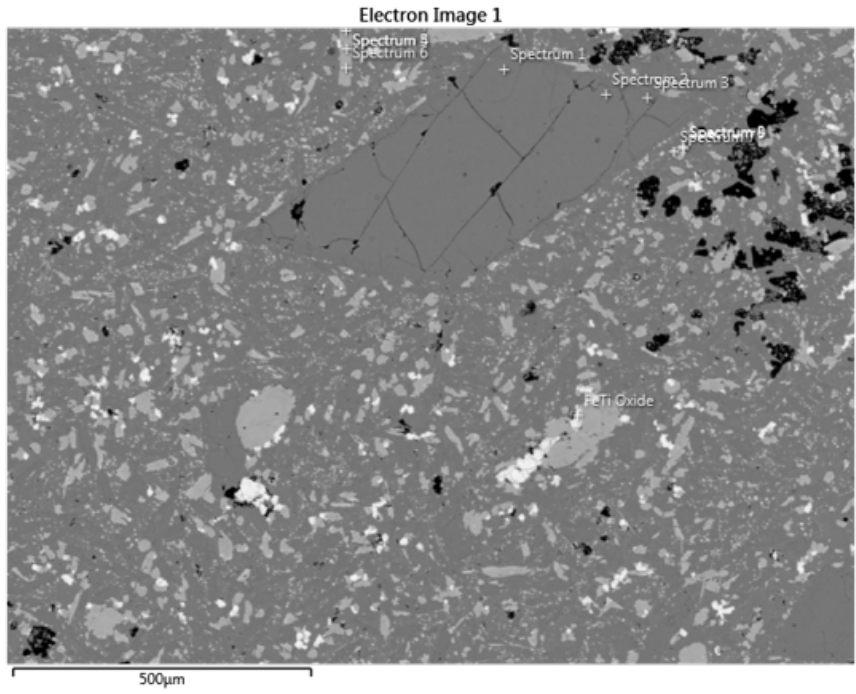**Figure B-9.** Electron images of site 4 of sample MAC-17-08.

Figure B-10. Electron images of site 5 of sample MAC-17-08.
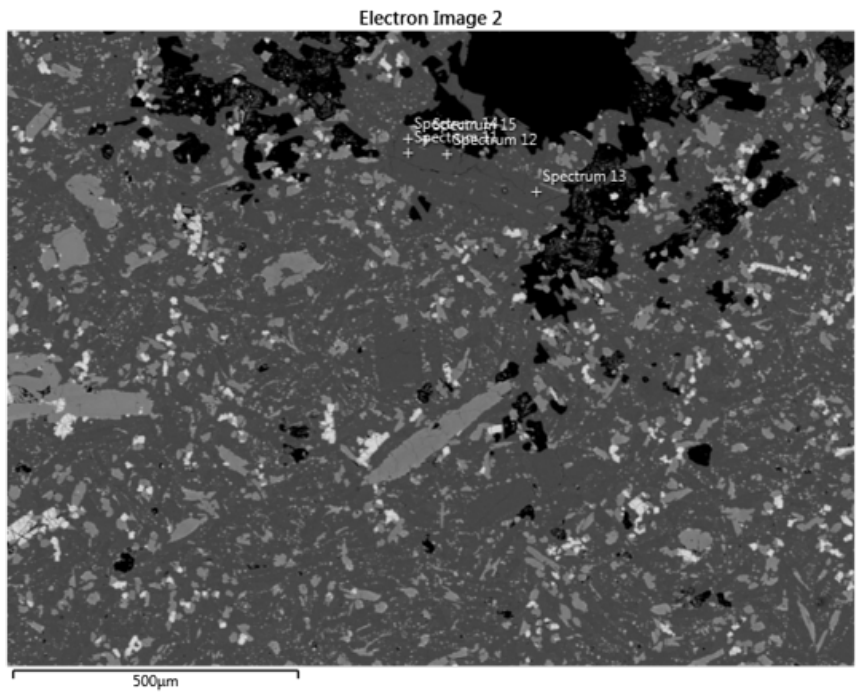

Figure B-11. Electron images of site 6 of sample MAC-17-08.
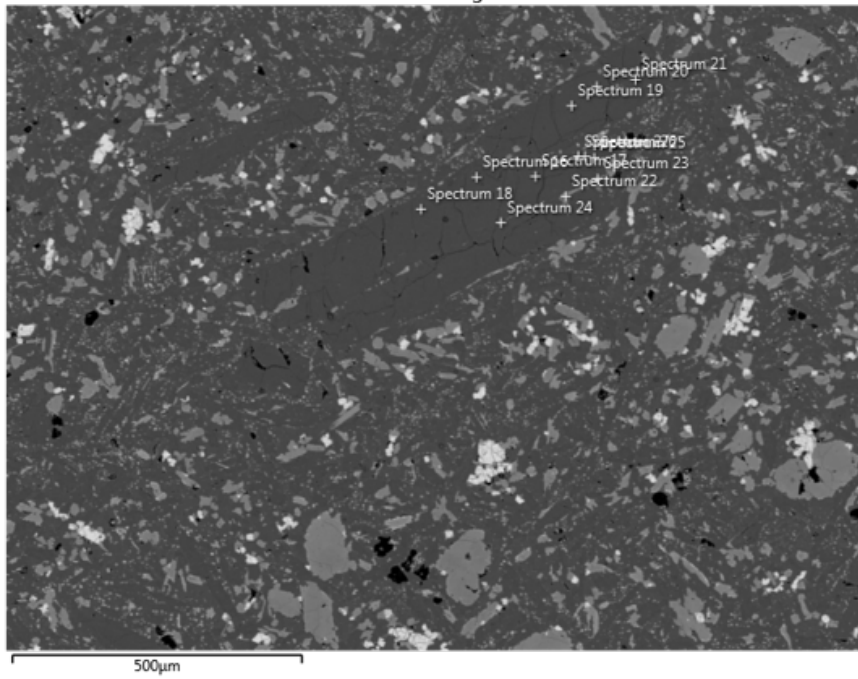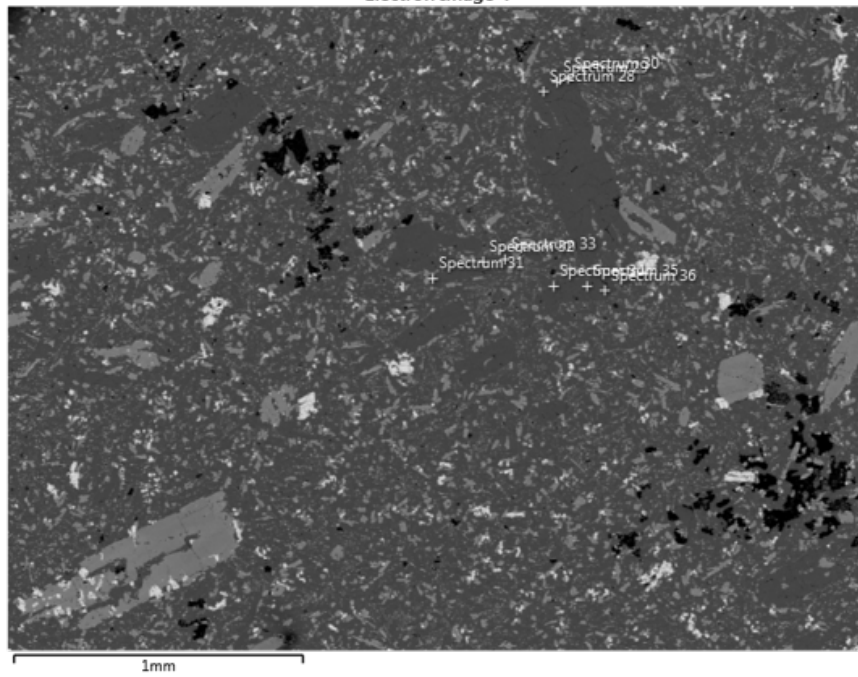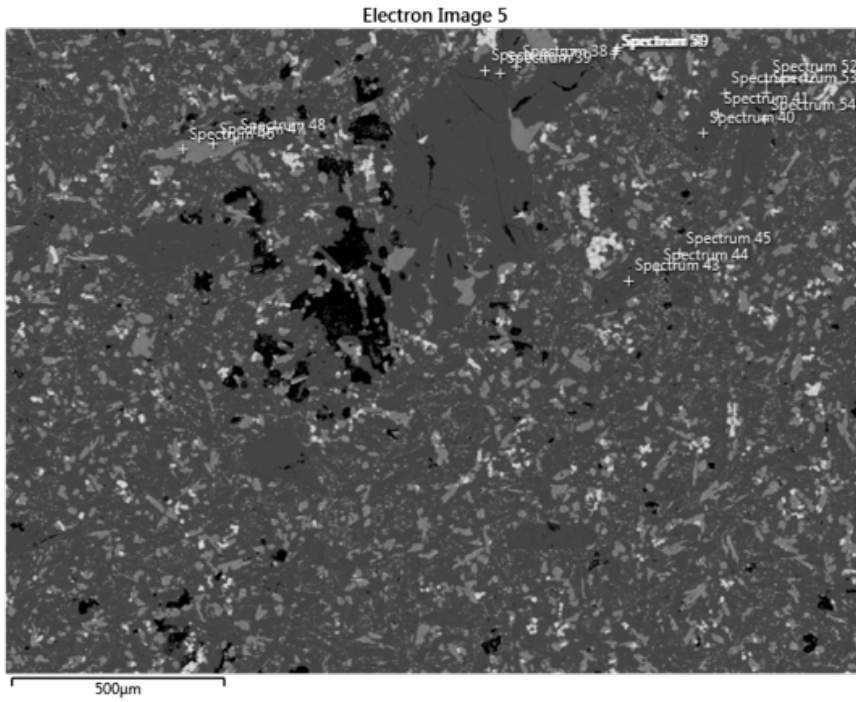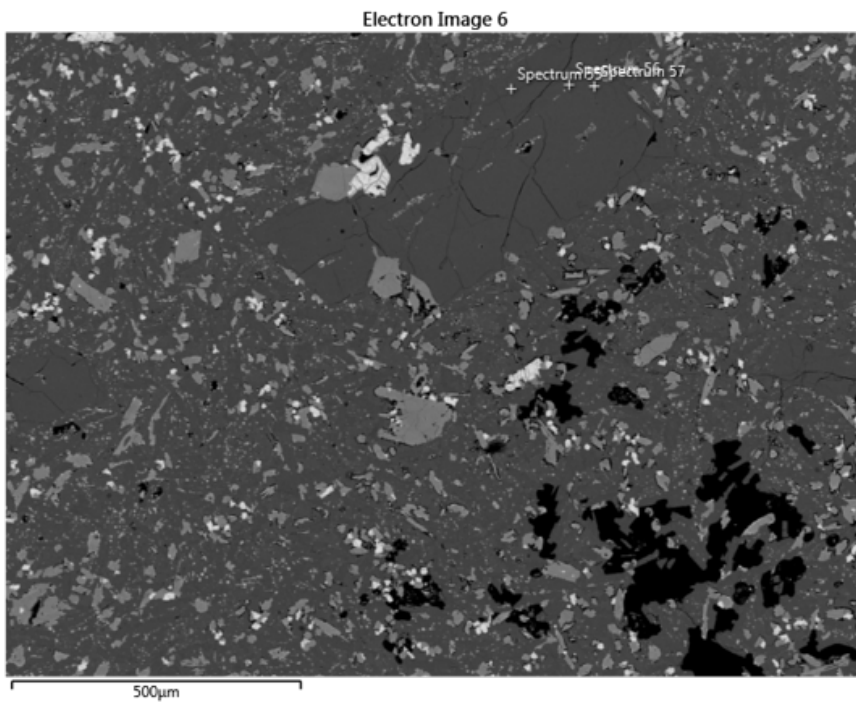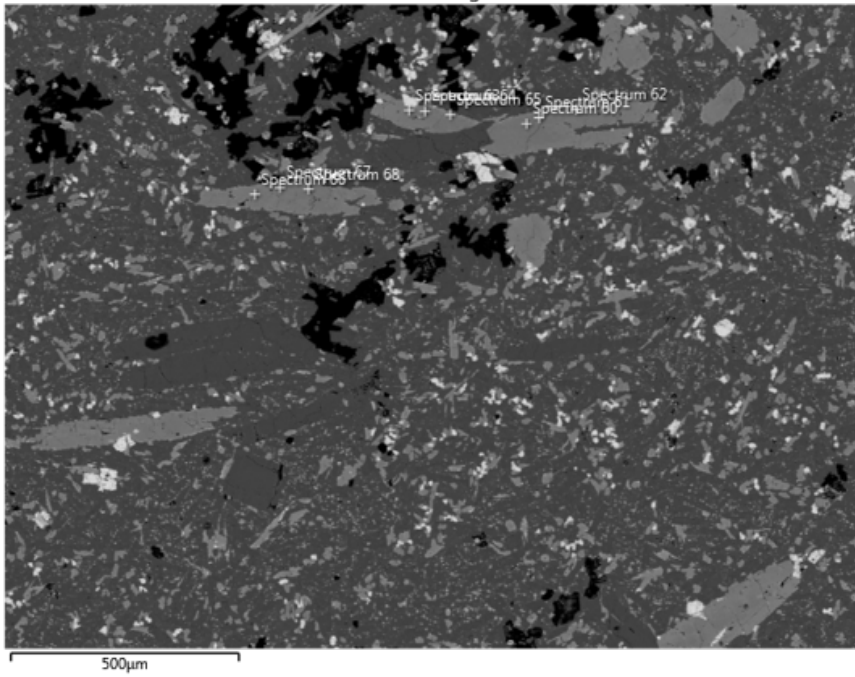
112

Electron Image 8

500μm

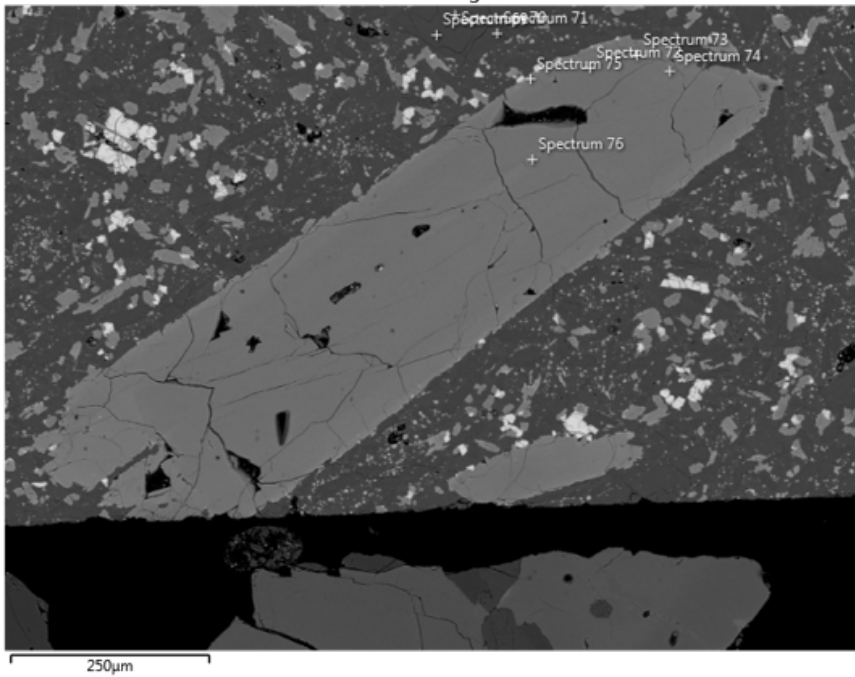**Figure B-12.** Electron images of site 8 of sample MAC-17-08.

Electron Image 9

250μm

Figure B-13. Electron images of site 9 of sample MAC-17-08.

Table B-2. Selected EDS spectra for sites 1-9 of MAC-17-08.

| MAC 17-08	SiO$_2$	TiO$_2$	Al$_2$O$_3$	FeO	MnO	MgO	CaO	Na$_2$O	K$_2$O	P$_2$O$_5$	Total	Phase
Spectrum 1	55.82		27.28	0.69			9.66	5.53	0.36		99.35	Plagioclase
Spectrum 5	49.60	0.73	1.20	20.87	0.81	12.07	13.93	0.37		0.87	100.45	Pyroxene
Spectrum 11	55.90		26.47	0.79			9.06	5.74	0.40		98.38	Plagioclase
Spectrum 12	56.46		25.46	0.49			8.16	6.06	0.48		97.11	Plagioclase
Spectrum 14	56.70		25.55	0.54			8.28	6.05	0.42		97.54	Plagioclase
Spectrum 15	57.40		25.79	0.70			8.11	6.35	0.53		98.90	Plagioclase
Spectrum 19	55.65		26.15	0.58			8.83	5.72	0.31		97.24	Plagioclase
Spectrum 20	56.26		26.18	0.53			8.63	5.92	0.37		97.89	Plagioclase
Spectrum 21	56.54		26.20	0.68			8.52	5.85	0.48		98.27	Plagioclase
Spectrum 42	57.46		26.16	0.66			8.80	6.04	0.46		99.57	Plagioclase
Spectrum 47	49.01	1.22	2.94	18.31	0.45	11.55	16.45				99.94	Pyroxene
Spectrum 49	50.71	0.63	0.81	27.26	0.79	13.20	6.53				99.93	Pyroxene
Spectrum 53	57.04		26.37	0.62			8.84	5.83	0.43		99.14	Plagioclase
Spectrum 56	57.05		26.72	0.64			9.05	6.00	0.36		99.82	Plagioclase
Spectrum 60	50.52	0.76	1.63	17.39		12.19	16.67	0.30			99.46	Pyroxene
Spectrum 64	50.15	0.79	1.71	20.54	0.74	12.75	13.11				99.78	Pyroxene
Spectrum 68	49.84	1.04	2.06	19.76	0.51	12.54	13.89				99.63	Pyroxene
Spectrum 70	56.86		26.95	0.51			9.09	5.85	0.39		99.65	Plagioclase
Spectrum 72	49.81	1.00	1.71	16.45	0.51	12.52	16.44	0.29			98.72	Pyroxene
Spectrum 76	50.45	0.42	0.88	24.93	0.83	16.48	4.65	0.20			98.83	Pyroxene
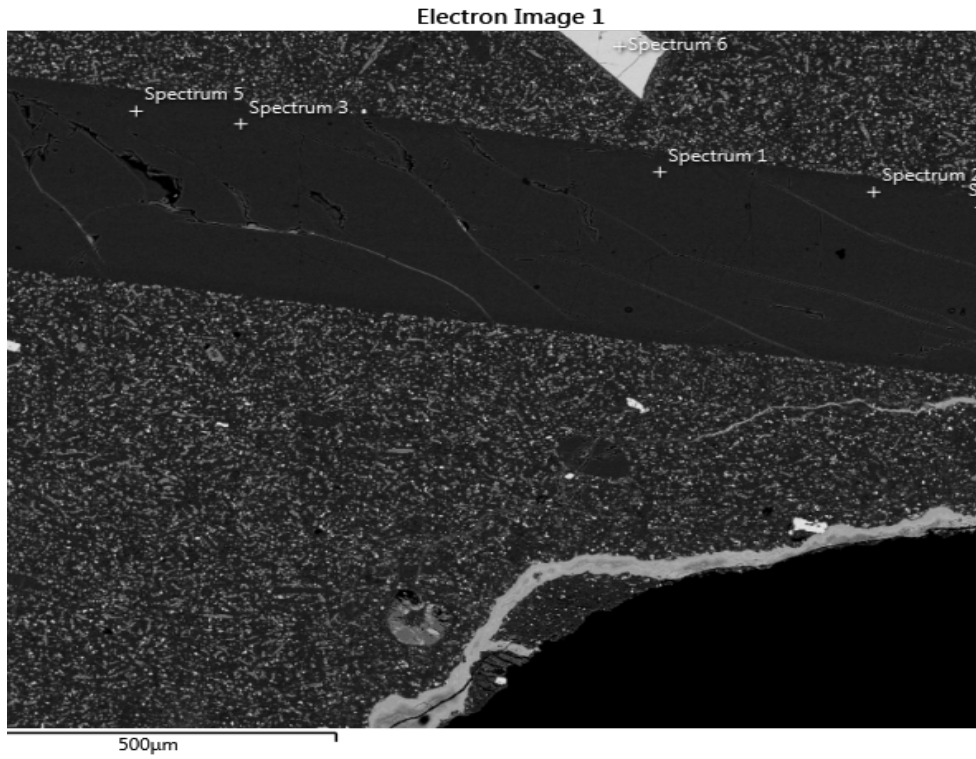
Figure B-14. Electron images of site 1 of sample MAC-17-16.

Figure B-15. Electron images of site 2 of sample MAC-17-16.

Figure B-16. Electron images of site 3 of sample MAC-17-16.

Figure B-17. Electron images of site 4 of sample MAC-17-16.

Table B-3. Selected EDS spectra for sites 1-4 of MAC-17-16.

MAC-17-16	SiO$_2$	TiO$_2$	Al$_2$O$_3$	FeO	MnO	MgO	CaO	Na$_2$O	K$_2$O	P$_2$O$_5$	Total	Phase
Spectrum 1	56.02		27.75	0.62			9.92	5.56	0.34		100.22	Plagioclase
Spectrum 4	55.40		26.77	0.55			9.41	5.65	0.47		98.26	Plagioclase
Spectrum 9	56.75		27.33	0.48			9.56	5.64	0.39		100.15	Plagioclase
Spectrum 22	50.82	0.86	1.19	17.41	0.54	13.55	14.90	0.21			99.48	Pyroxene
Spectrum 23	50.38	0.73	1.39	16.43	0.54	13.06	15.55	0.24			98.30	Pyroxene
Spectrum 27	50.80	0.74	1.30	16.78	0.54	13.39	15.47	0.24			99.27	Pyroxene
Spectrum 28	50.51	0.88	1.34	15.98	0.46	12.93	16.80	0.20			99.11	Pyroxene
Spectrum 33	56.00		26.87	0.64			9.05	5.72	0.40		98.68	Plagioclase
Spectrum 34	0.25		0.10	0.57		0.21	53.41			41.34	95.88	Apatite
Spectrum 35	0.32			0.66		0.21	53.40			41.14	95.73	Apatite
Spectrum 36	0.27		0.10	0.83		0.19	53.33			41.58	96.30	Apatite
Spectrum 38	57.95		26.58	0.69			8.39	6.11	0.46		100.19	Plagioclase
Spectrum 42	55.84		26.87	0.71			9.41	5.65	0.49		98.97	Plagioclase
Spectrum 46	50.39	0.62	1.02	20.78	0.68	13.35	12.07				98.91	Pyroxene
Spectrum 49	50.60	0.62	0.74	23.99	0.84	14.78	7.20	0.13			98.89	Pyroxene
Spectrum 51	50.12	0.43	0.60	26.44	0.71	14.87	4.75				97.91	Pyroxene
Spectrum 53	49.09	0.85	1.32	21.51	0.62	13.31	10.51				97.20	Pyroxene
Spectrum 56	0.28	49.48	0.18	45.77	1.04	0.27	0.27				97.29	FeTi Oxide
Spectrum 58	56.90		26.54	0.68			8.96	5.97	0.55		99.61	Plagioclase
Spectrum 62	56.43		26.62	0.67			8.61	5.86	0.49		98.68	Plagioclase

Electron Image 2

Figure B-18. Electron images of site 1 of sample MAC-17-18.
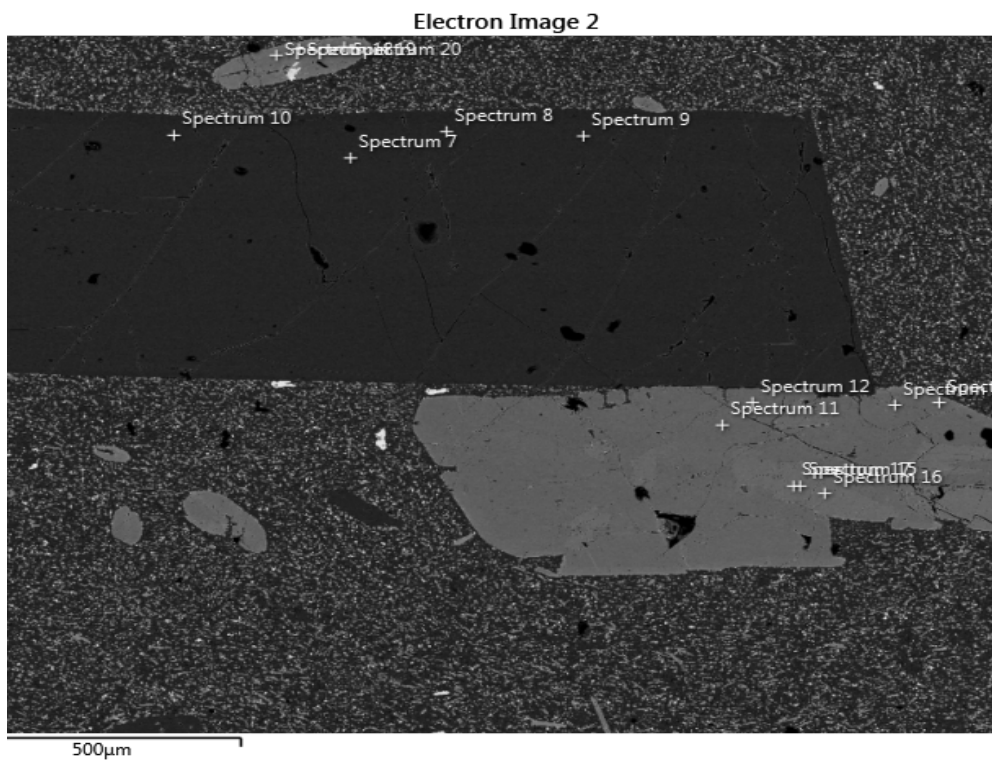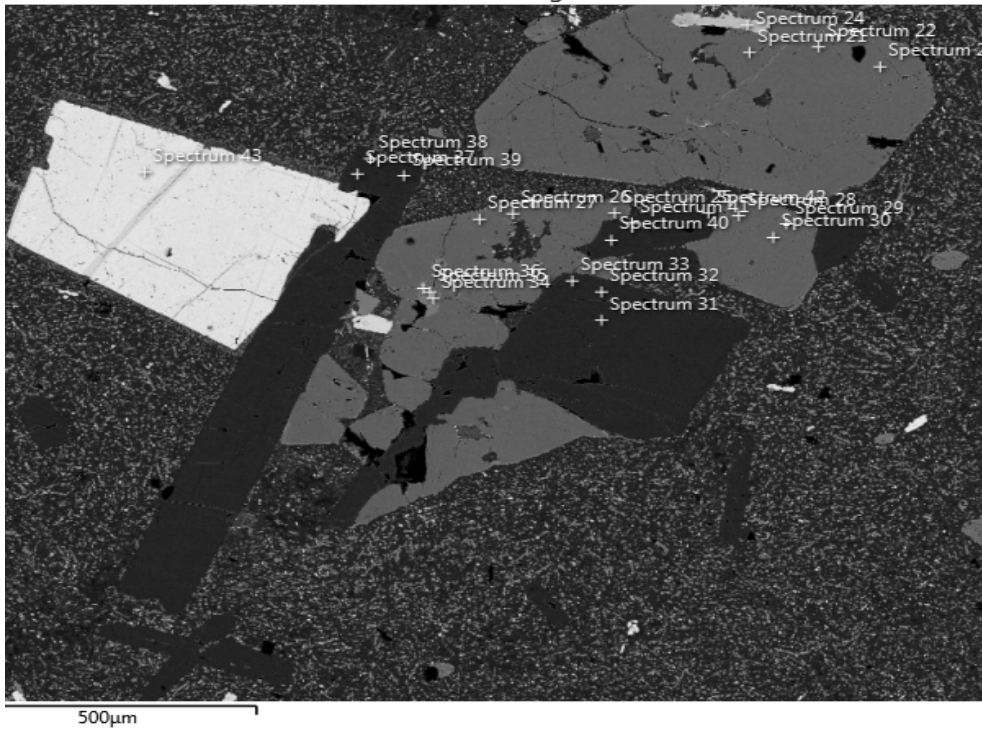
Electron Image 3

Figure B-19. Electron images of site 2 of sample MAC-17-18.

Electron Image 4

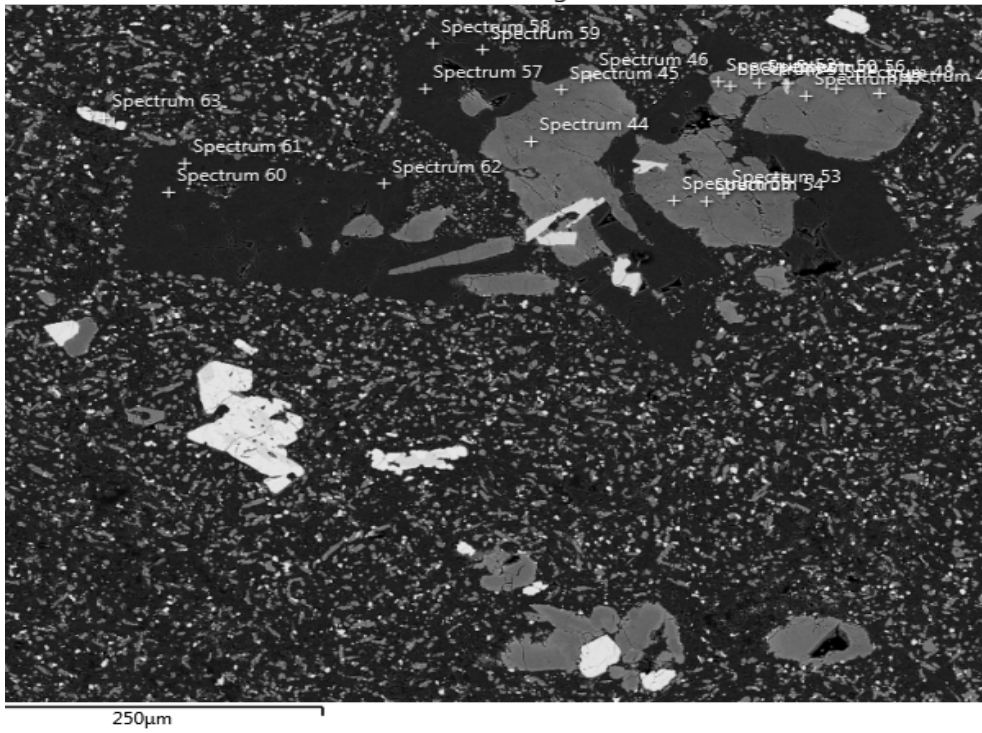**Figure B-20.** Electron images of site 3 of sample MAC-17-18.

Electron Image 5
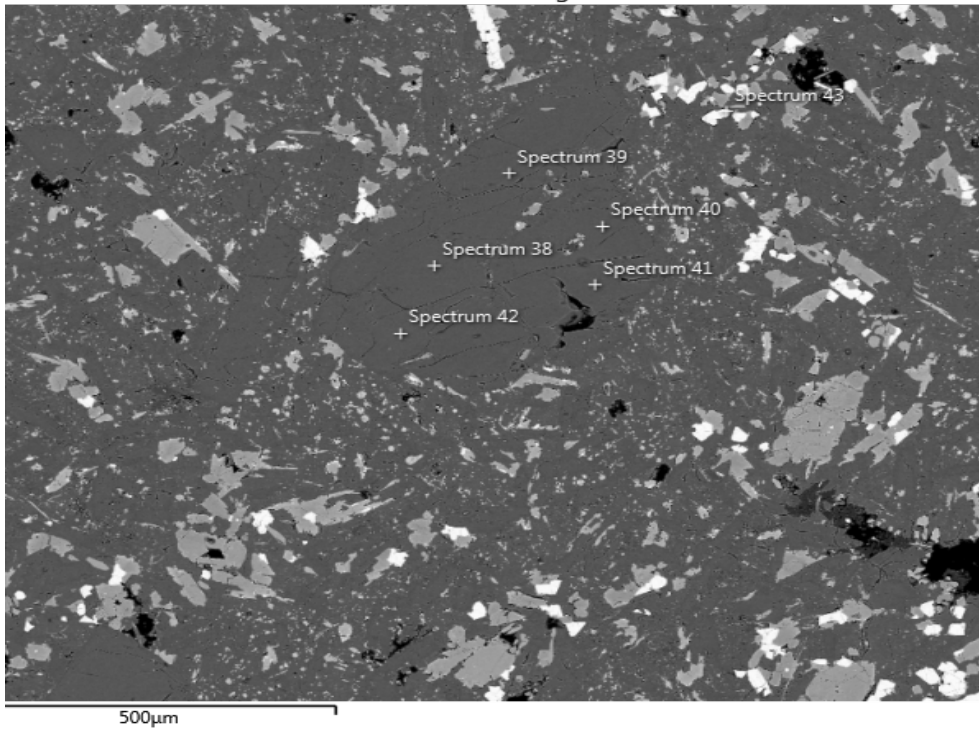
Figure B-21. Electron images of site 4 of sample MAC-17-18.

Electron Image 6
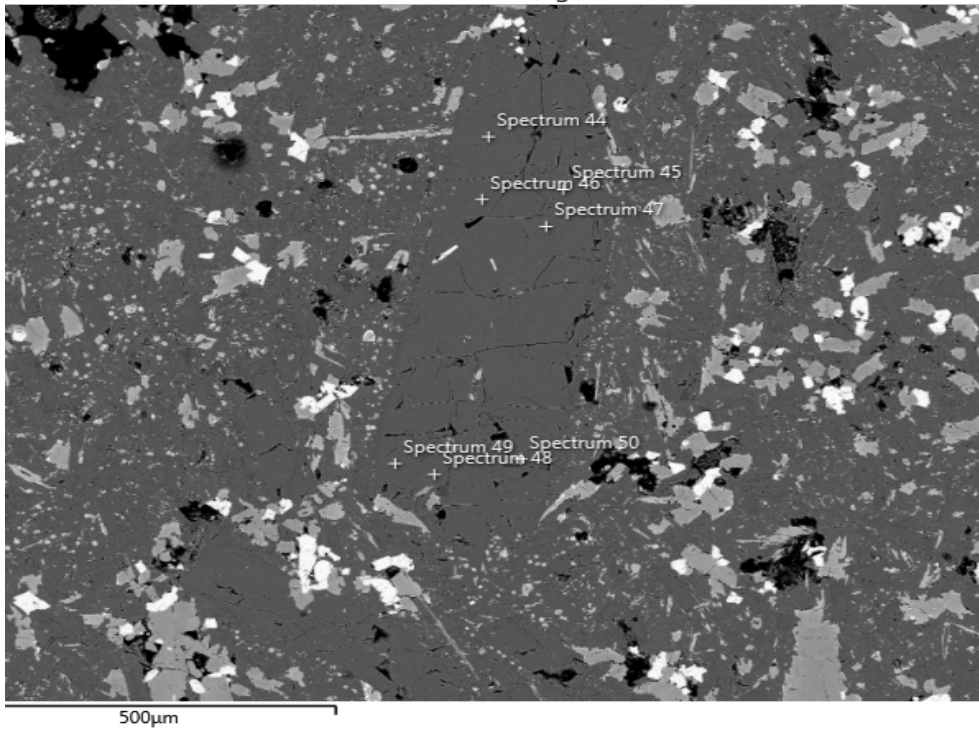
Figure B-22. Electron images of site 5 of sample MAC-17-18.

Electron Image 7
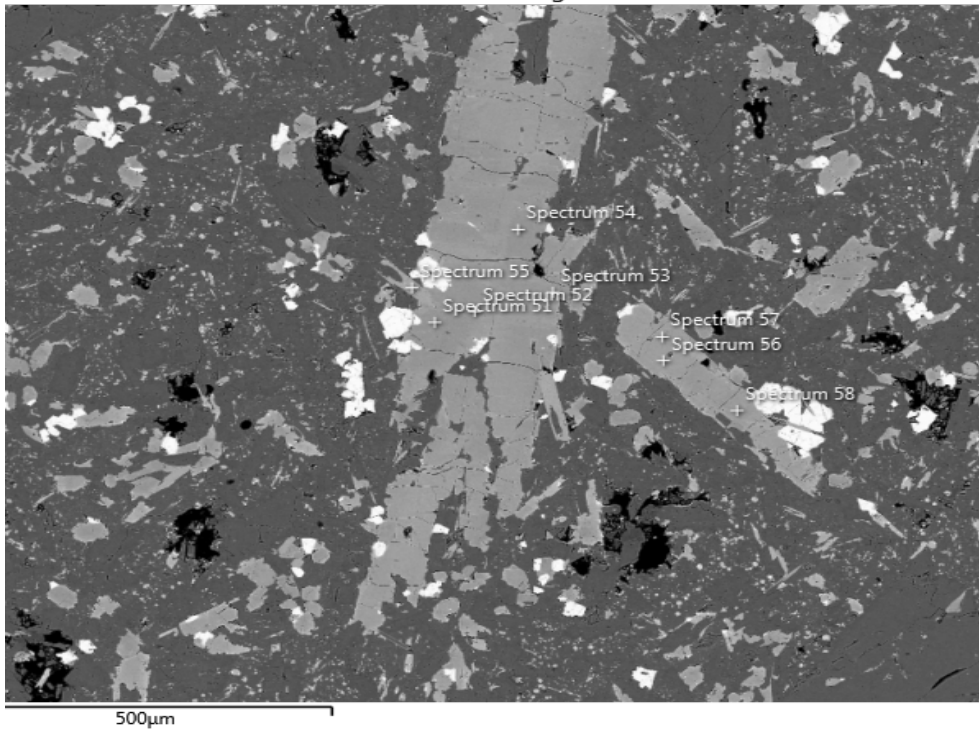
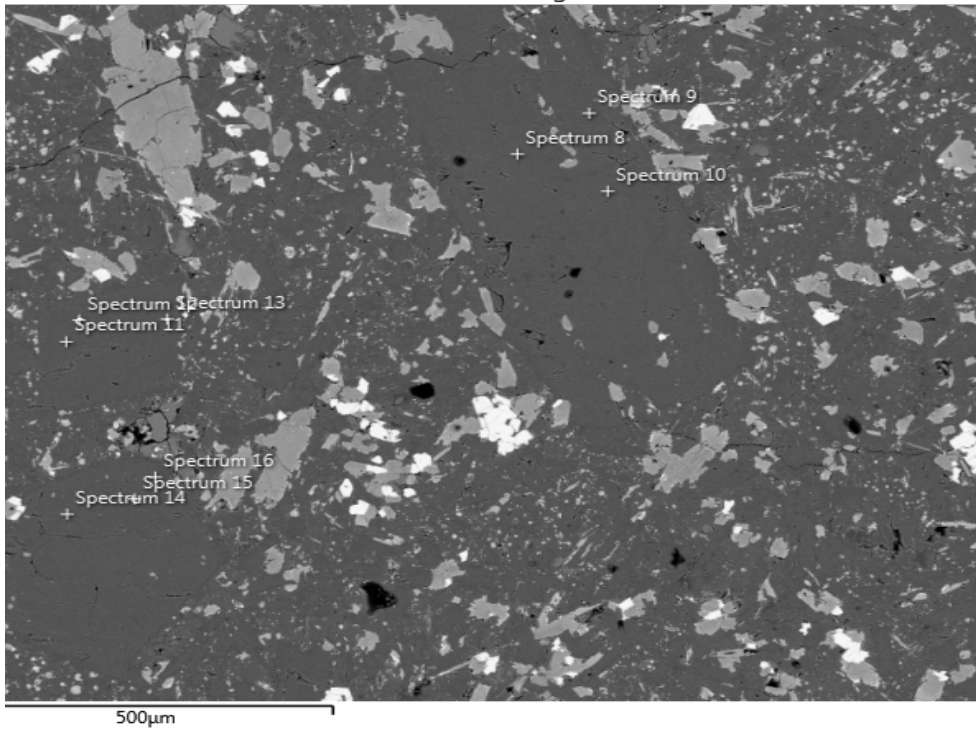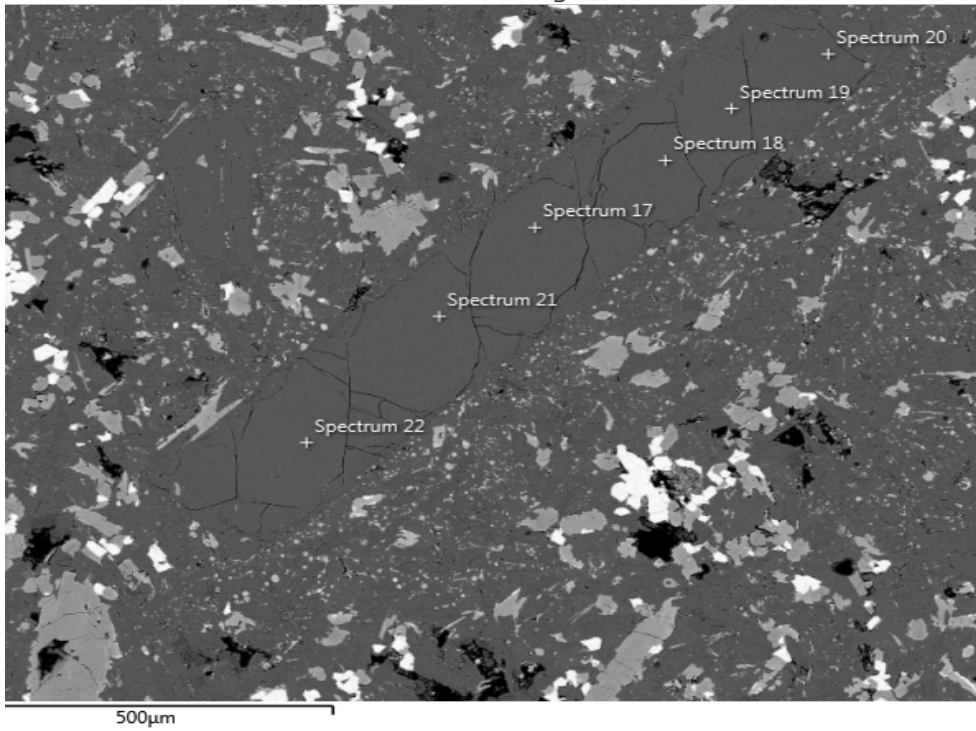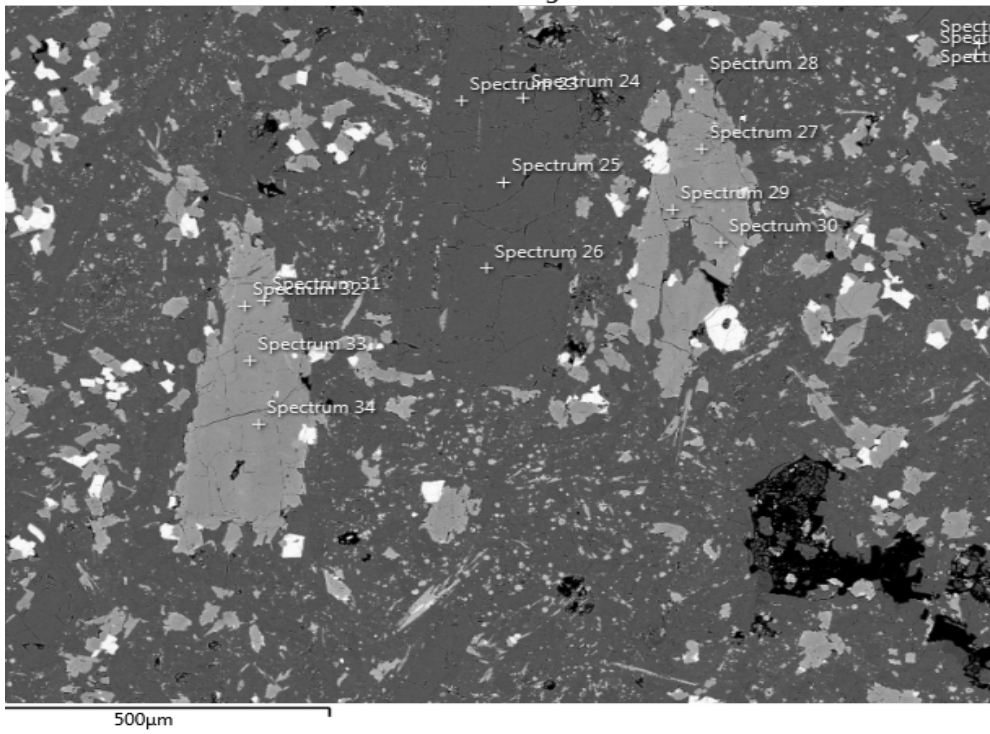**Figure B-23.** Electron images of site 6 of sample MAC-17-18.

Figure B-24. Electron images of site 7 of sample MAC-17-18.

Electron Image 9

Figure B-25. Electron images of site 8 of sample MAC-17-18.

Figure B-26. Electron images of site 9 of sample MAC-17-18.
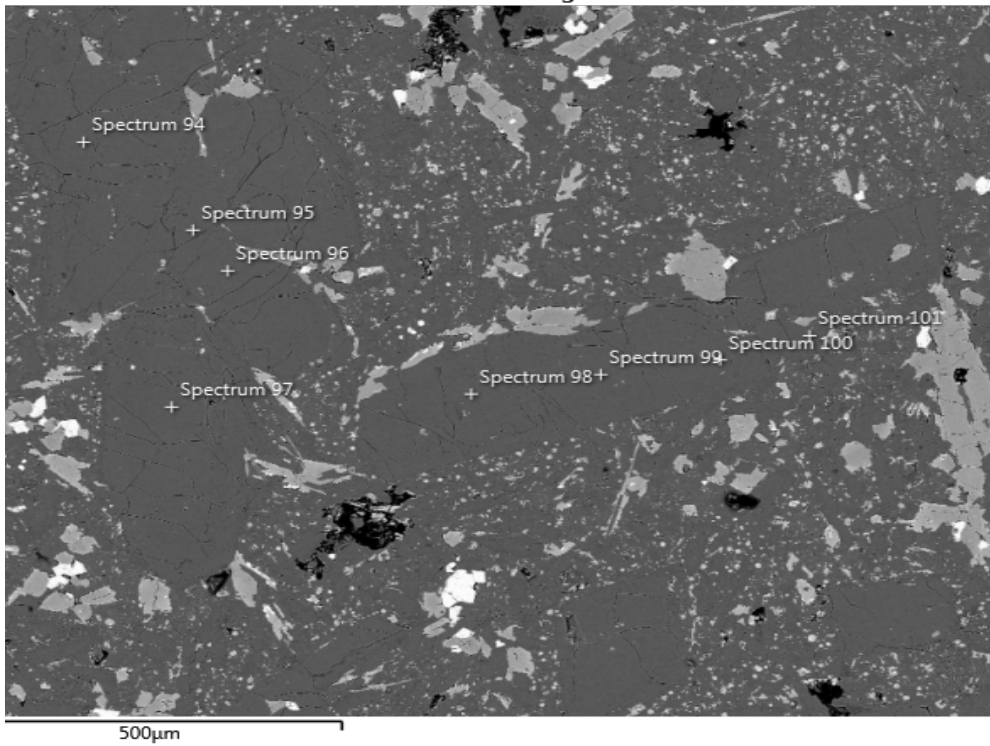
Figure B-27. Electron images of site 10 of sample MAC-17-18.
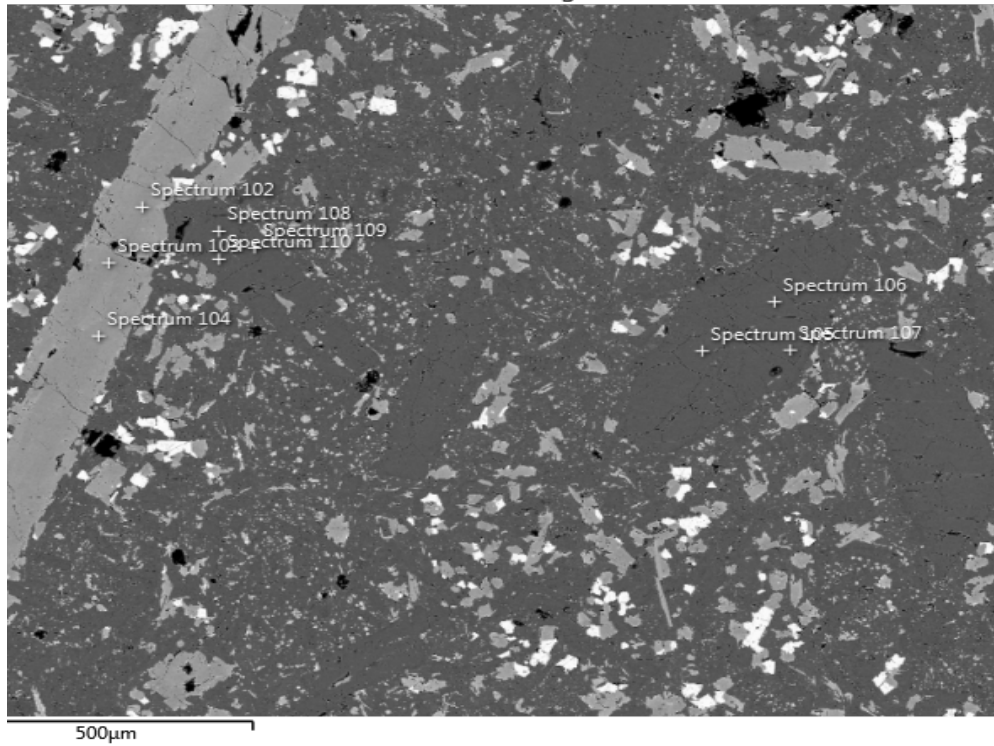
Figure B-28. Electron images of site 11 of sample MAC-17-18.

Table B-4. Selected EDS spectra for sites 1-11 of MAC-17-18.

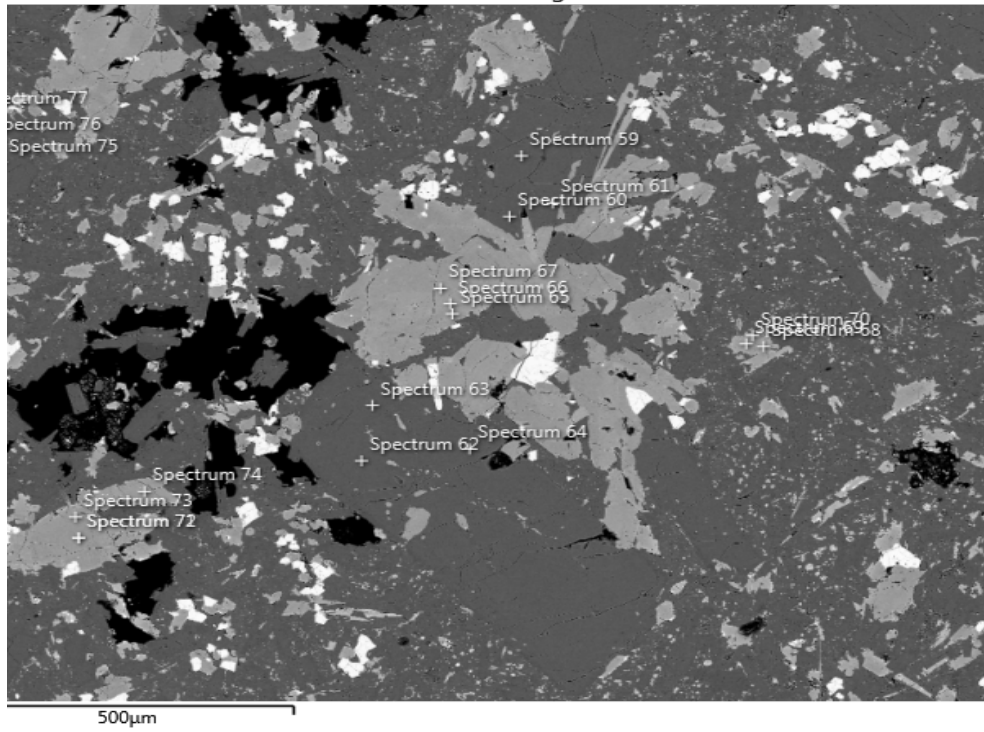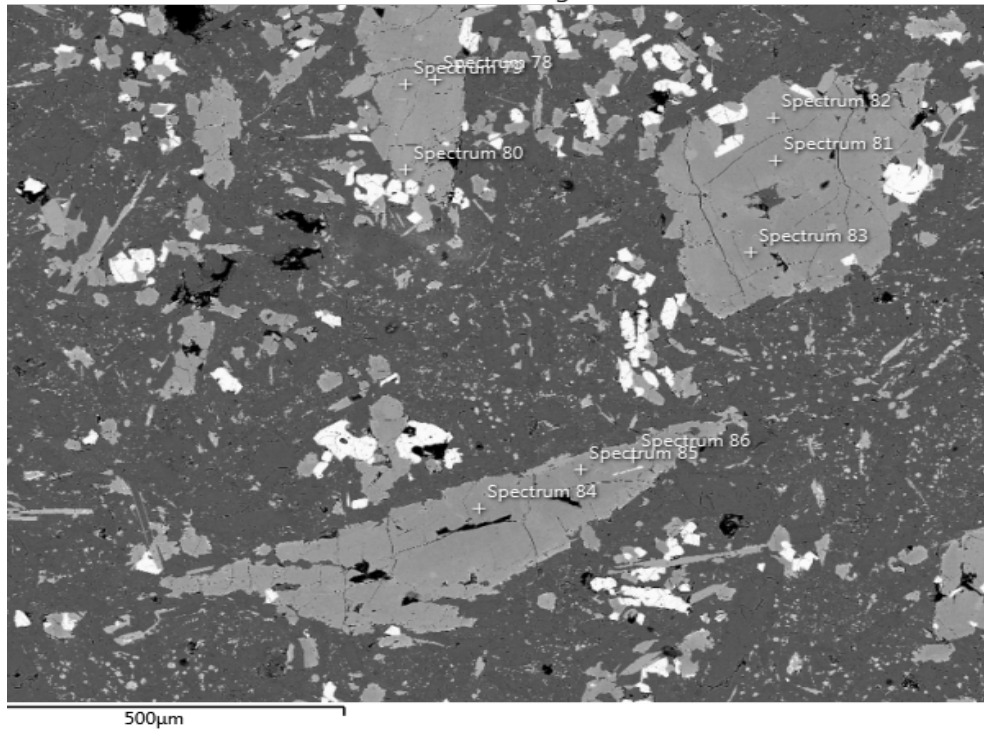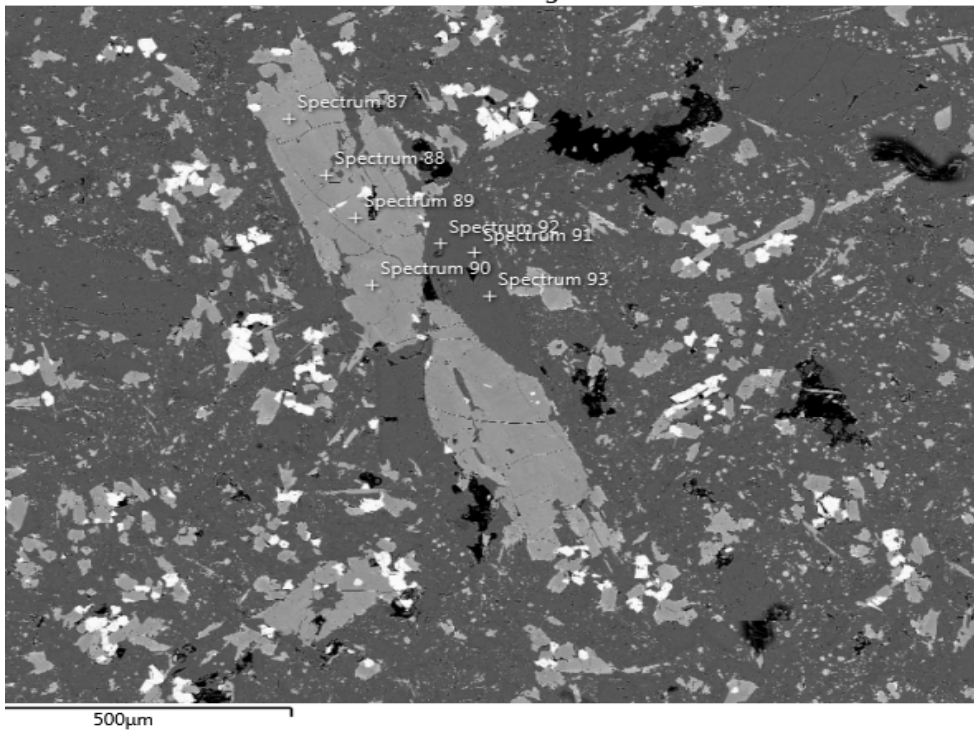| MAC-17-18	SiO$_2$	TiO$_2$	Al$_2$O$_3$	FeO	MnO	MgO	CaO	Na$_2$O	K$_2$O	P$_2$O$_5$	Total	Phase
Spectrum 14	57.94		26.74				8.70	6.06	0.48		99.92	Plagioclase
Spectrum 15	58.40		26.18	0.61			8.52	6.19	0.57		100.48	Plagioclase
Spectrum 22	56.49		27.41	0.53			9.95	5.72	0.37		100.47	Plagioclase
Spectrum 30	50.72	0.93	1.79	19.88	0.46	12.89	13.48	0.29			100.46	Pyroxene
Spectrum 32	50.38	0.62	1.22	24.36	0.61	13.67	8.83	0.17			99.85	Pyroxene
Spectrum 43	0.37	25.12	1.87	71.25	0.79		0.19				99.60	altered Olivine
Spectrum 50	57.58		26.46	0.49			8.69	6.15	0.51		99.89	Plagioclase
Spectrum 55	2.09	0.44	0.47	1.90		0.13	52.69	0.20	0.16	40.45	98.54	Apatite
Spectrum 58	50.35	0.84	1.20	22.42	0.83	13.00	11.26	0.17			100.07	Pyroxene
Spectrum 62	56.58		26.77	0.49			9.31	5.66	0.45		99.26	Plagioclase
Spectrum 64	56.97		26.23	0.57			8.74	5.99	0.51		99.01	Plagioclase
Spectrum 68	50.98	0.58	0.67	26.94	0.94	14.65	5.69				100.45	Pyroxene
Spectrum 73	49.10	0.81	1.42	20.98	0.61	12.46	12.20	0.28			97.87	Pyroxene
Spectrum 74	49.89	0.42	0.52	27.30	0.91	14.77	4.94				98.76	Pyroxene
Spectrum 86	49.65	0.99	1.63	18.41	0.57	12.03	15.49	0.27			99.04	Pyroxene
Spectrum 97	58.07		26.65	0.44			8.97	5.87	0.45		100.46	Plagioclase
Spectrum 98	56.60		26.81	1.72		0.41	8.86	5.65	0.46		100.50	Plagioclase
Spectrum 101	58.60		25.46	1.17			8.09	6.19	0.61		100.11	Plagioclase

Electron Image 2

Figure B-28. Electron images of site 1 of sample MAC-17-29

Electron Image 3
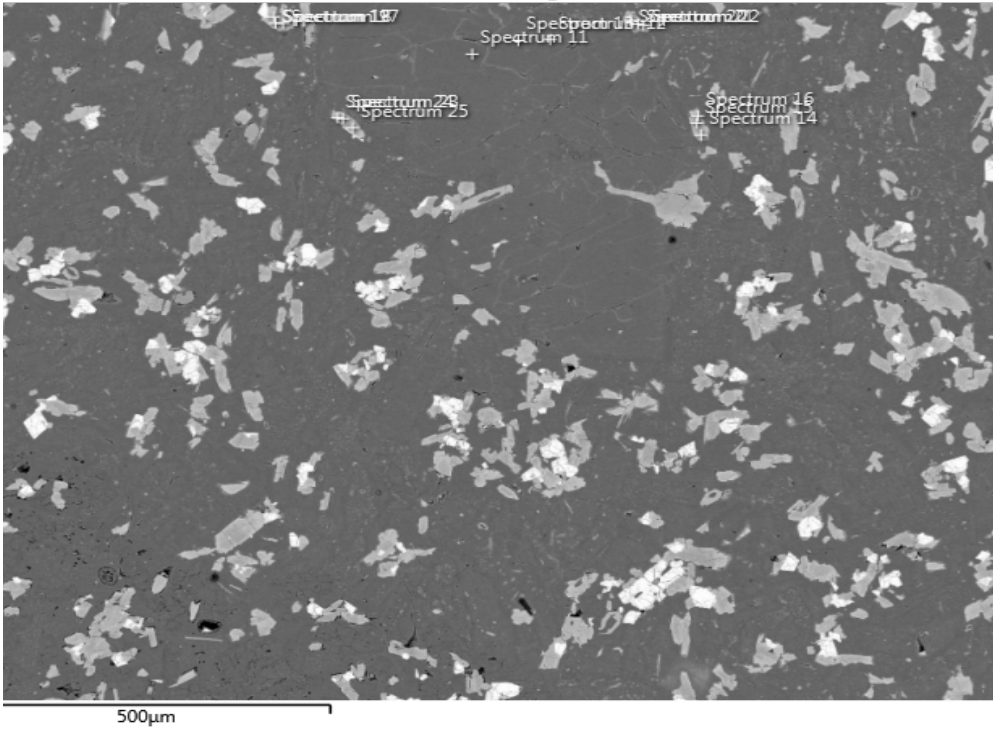
Figure B-29. Electron images of site 2 of sample MAC-17-29

124

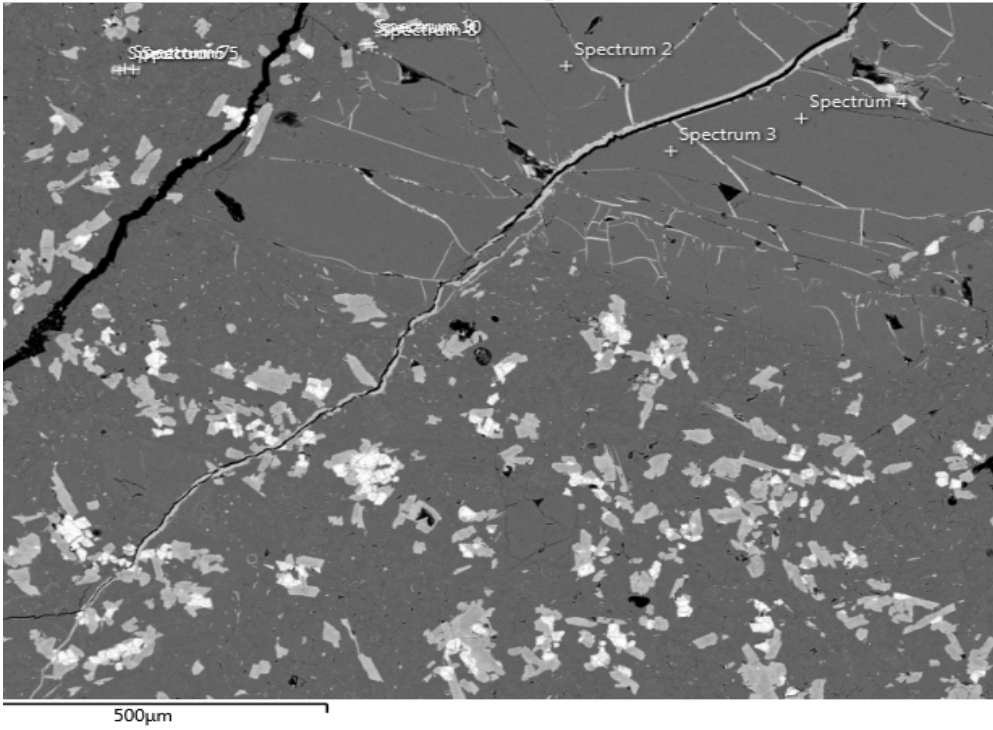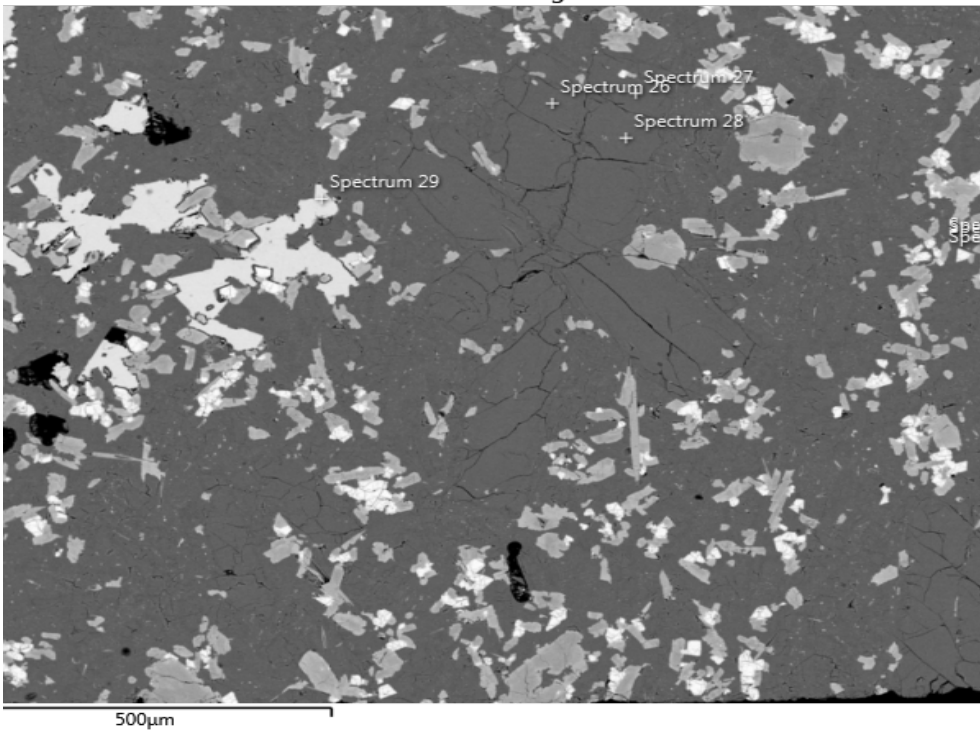**Figure B-30.** Electron images of site 3 of sample MAC-17-29
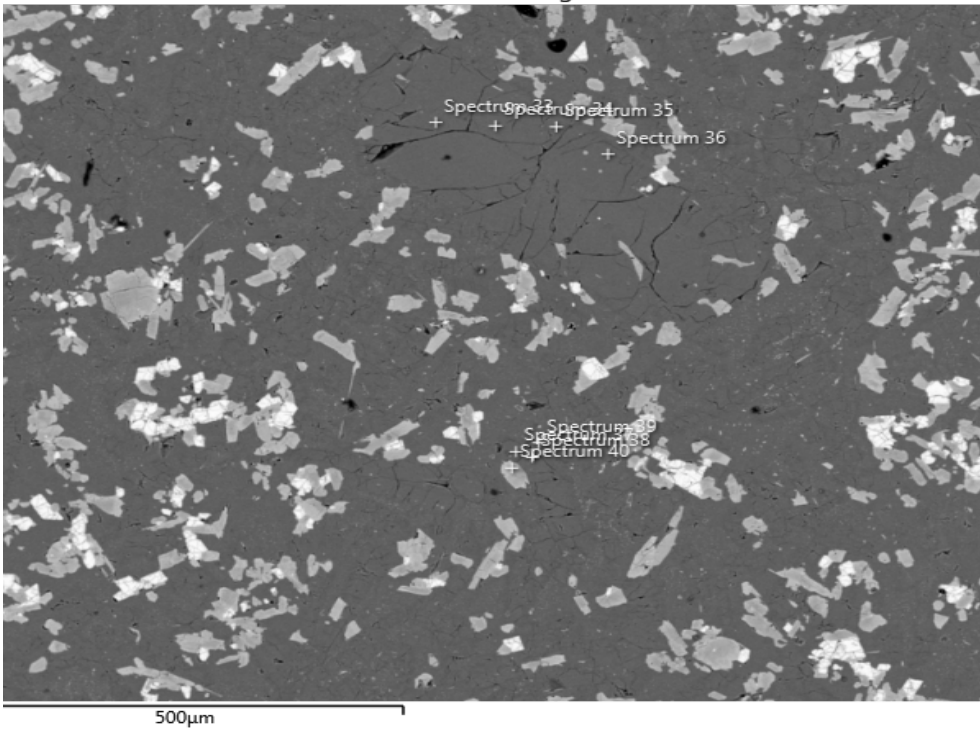
Figure B-31. Electron images of site 4 of sample MAC-17-29
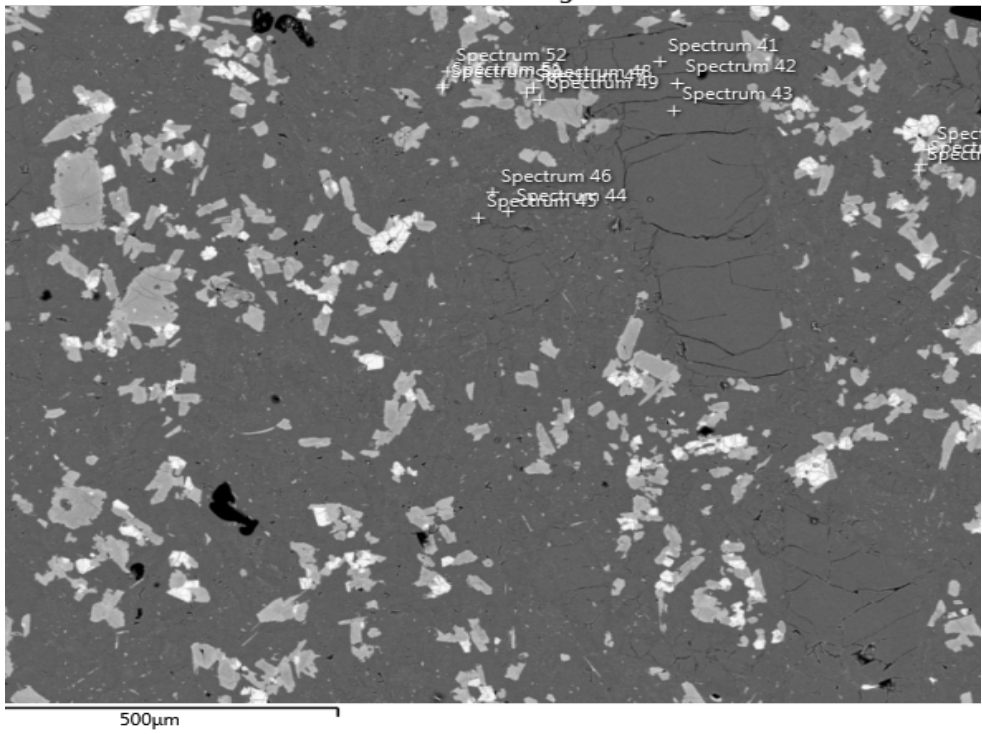
Figure B-32. Electron images of site 5 of sample MAC-17-29
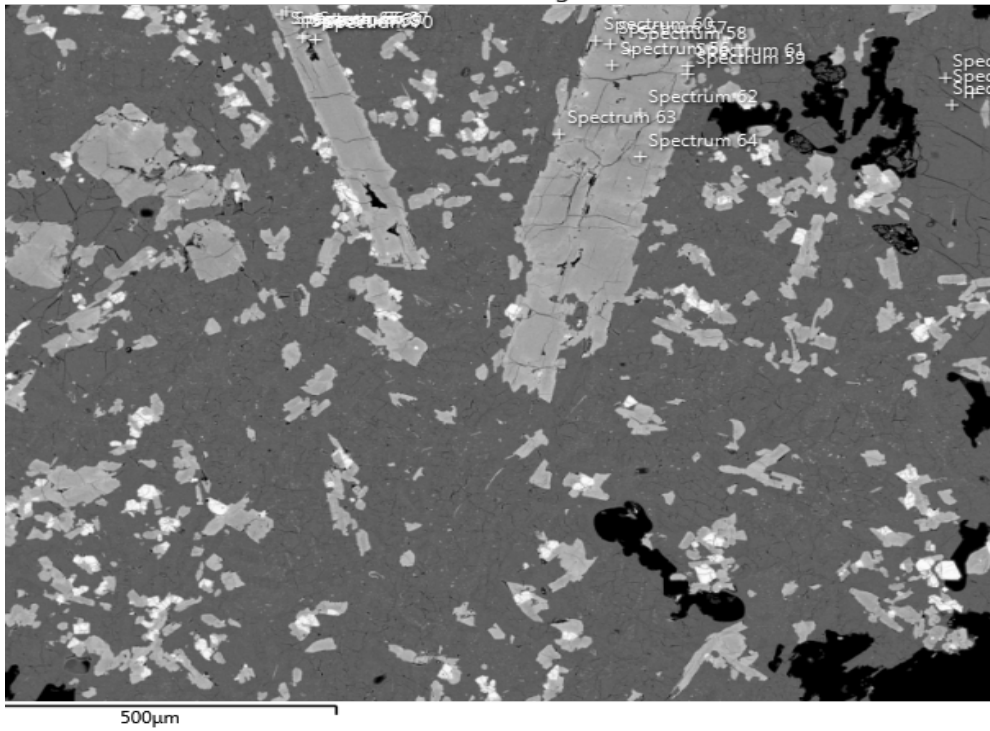
Figure B-33. Electron images of site 6 of sample MAC-17-29

Table B-5. Selected EDS spectra for sites 1-6 of MAC-17-29.

MAC-17-29	SiO$_2$	TiO$_2$	Al$_2$O$_3$	FeO	MnO	MgO	CaO	Na$_2$O	K$_2$O	P$_2$O$_5$	Total	Phase
Spectrum 3	56.08		27.60	0.62			10.16	5.56	0.39		100.41	Plagioclase
Spectrum 4	56.06		27.52	0.63			10.06	5.46	0.40		100.14	Plagioclase
Spectrum 6	49.32	0.60	0.98	25.58	0.74	9.60	11.96	0.20			98.99	Pyroxene
Spectrum 14	49.98	0.52	0.81	27.01	0.95	11.66	8.93	0.10			99.95	Pyroxene
Spectrum 20	49.07	0.57	1.29	31.95	1.09	7.90	8.20	0.12			100.18	Pyroxene
Spectrum 25	50.21	0.49	0.63	30.27	0.92	12.16	5.62				100.31	Pyroxene
Spectrum 28	57.75		26.73	0.48			8.89	6.05	0.44		100.33	Plagioclase
Spectrum 31	49.97	0.43	0.67	26.98	0.76	14.97	5.24				99.02	Pyroxene
Spectrum 33	58.05		26.46	0.57			8.58	6.13	0.50		100.29	Plagioclase
Spectrum 36	58.48		25.79	0.53			7.70	6.58	0.51		99.60	Plagioclase
Spectrum 40	48.73	0.47	0.61	30.85	0.87	11.03	5.51	0.13			98.21	Pyroxene
Spectrum 44	58.08		26.35	0.51			8.30	6.45	0.56		100.25	Plagioclase
Spectrum 46	58.12		25.97	0.64			8.20	6.28	0.51		99.73	Plagioclase
Spectrum 55	50.16	0.76	1.06	19.79	0.65	11.15	15.39	0.18			99.13	Pyroxene
Spectrum 59	52.36		13.27	17.33	0.61	3.11	6.11	4.03	0.40		97.23	Plagioclase?
Spectrum 61	49.35	0.62	0.69	32.47	1.01	10.04	5.96	0.11			100.23	Pyroxene
Spectrum 63	49.40	0.46	0.67	27.95	0.84	7.96	12.29	0.28			99.86	Pyroxene
Spectrum 73	57.12		26.60	0.68			9.00	6.21	0.48		100.08	Plagioclase

Appendix C: Partition Coefficients

Table C-1. Partition coefficients used in crystallization model.

	Plagioclase	Olivine	Clinopyroxene	Magnetite	Ilmenite	Bulk-D value
Sc	0.008	0.235	1.31	0.73	1.8	0.556
Ni	0.06	15.5	2.6	48	3.8	6.839
Cr	0.075	1.18	4.22	153	29.85	17.58
V	0.0071	0.03	3.1	3.435	12	2.109
Rb	0.0172	0.00018	0.011	0.11	0.034	0.0239
Ba	0.21	0.05	0.0002	0.028	0.018	0.1121
Th	0.05	0.0001	0.00026	0.1	0.00165	0.0337
U	0.11	0.0001	0.0036	0.11	0.00695	0.0653
Nb	0.01	0.01	0.00365	0.905	1.225	0.1984
Ta	0.106	0.067	0.01195	1.27	1.73	0.3314
K	0.192	0.006845	0.007	0.045	0.4118	0.1375
La	0.0348	0.008	0.1047	0.015	0.098	0.0521
Ce	0.0278	0.0076	0.1254	0.016	0.11	0.0546
Pb	0.19	0.0001	0.216	2.9	0.117	0.4143
Pr	0.02231	0.006611	0.18958	0.0204	0.1241	0.0682
Sr	1.82	0.0005	0.06	0.11	0.0046	0.9160
P	0.071	0.1	0.05	0.053	0.025	0.0634
Nd	0.0179	0.00575	0.2866	0.026	0.14	0.0902
Zr	0.0094	0.0047	0.131	0.9	0.3315	0.1460
Hf	0.0092	0.0038	0.1208	0.14	0.4135	0.0825
Sm	0.0132	0.0049	0.4774	0.024	0.15	0.1324
Eu	0.0221	0.0052	0.5618	0.025	0.1	0.1518
Ti	0.026	0.00355	0.325	6	0.118	0.6385
Tb	0.0118	0.0071	0.6085	0.019	0.14	0.1608
Dy	0.0112	0.0095	0.622	0.0180	0.1349	0.164
Y	0.0043	0.0131	0.9	0.0039	0.0045	0.2112
Yb	0.0155	0.0468	0.601	0.018	0.1225	0.1632
Lu	0.012	0.053	0.5602	0.023	0.1005	0.1511
Gd	0.0125	0.0053	0.595	0.018	0.14	0.158
Ho	0.0114	0.0157	0.645	0.017	0.13	0.171
Er	0.0116	0.0260	0.67	0.0173	0.1275	0.177
Tm	0.0134	0.0348	0.6346	0.0177	0.1250	0.171

Table C-2. Sources of partition coefficients used in crystallization model

Sources:

Bougault and Hekinian 1974	Klemme et al., 2006	Nielson et al., 1992
Brunet and Chazot, 2001	Kloeck and Palme 1988	Norman et al., 2005
Dunn and Sen, 1994	Laubier et al., 2014	Okamoto, 1979
Ewart and Griffin, 1994	Lemarchand et al. 1987	Paster et al., 1974
Fujimaki et al. 1984	Matsui et al. 1977	Philpotts and Schnetzler, 1970
Green et al. 1989	McKay et al., 1986	Ringwood, 1970
Green et al. 2000	McKenzie and O'nions, 1991	Interpolated values
Hart and Dunn, 1993	Mysen, 1978	
Jang and Nasland, 2003	Nielson, 1992	

Appendix D: Fractional (Rayleigh) Crystallization Model
Table D-1. Major and compatible trace element bulk rock geochemistry for group 1 used in crystallization model.

Major Element Oxide	Norm. Group 1 Parent	Transition	Low SiO2	Low TiO2 Group 1	High TiO2 Group 1	Average Group 1
SiO2	53.75	55.66	57.49	62.38	59.95	61.17
TiO2	2.99	2.30	2.39	1.30	1.97	1.63
Al2O3	14.07	13.80	13.41	13.22	13.29	13.25
FeO*	11.73	12.13	11.38	10.43	10.65	10.54
MnO	0.19	0.20	0.53	0.23	0.23	0.23
MgO	3.32	3.30	2.43	0.93	1.69	1.31
CaO	7.72	7.15	6.47	4.43	5.29	4.86
Na2O	3.03	3.32	3.07	3.71	3.55	3.63
K2O	1.79	1.69	2.40	2.97	2.60	2.78
P2O5	1.42	0.44	0.76	0.40	0.79	0.60
Total	100.00	100.00	100.35	100.00	100.00	100.00
Compatible Trace						
Sc	17	33.13	29.13	26.02	26.82	25.74
Ni	7	9.90	5.97	2.16	3.38	2.72
Cr	37.2	7.08	0.00	0.88	0.23	0.54
V	330	322.66	153.55	13.80	50.87	32.37

Table D-2. Incompatible trace element bulk rock geochemistry for group 1 used in crystallization model.

Incompatible Trace	Norm. Group 1 Parent	Transition	Low SiO2	Low TiO2 Group 1	High TiO2 Group 1	Average Group 1
Rb	41.16	42.46	38.18	80.60	64.60	72.60
Ba	874.00	705.42	938.64	1162.19	1097.67	1125.30
Th	6.140	5.23	5.27	9.09	8.11	8.60
U	1.67	1.55	2.33	2.66	2.31	2.48
Nb	10.60	13.36	14.79	21.72	17.65	19.68
Ta	0.80	0.88	0.96	1.36	1.16	1.26
K	15194	14093	16054.91	24665.98	21638.39	23126.94
La	33.68	26.77	31.12	43.70	40.11	41.97
Ce	67.07	56.02	64.03	91.63	81.74	86.69
Pb	15.31	12.13	8.30	13.51	14.54	15.37
Pr	9.200	7.44	8.80	11.95	10.86	11.42
Sr	374.350	339.99	373.73	299.36	326.77	312.70
P	6337	1937	3910.43	1737.82	3459.37	2597.09
Nd	40.85	31.88	37.55	49.75	46.22	48.03
Zr	154.73	201.81	221.21	324.10	264.56	294.36
Hf	4.28	5.37	5.78	8.50	7.02	7.76
Sm	5.89	7.76	9.00	11.70	11.12	11.42
Eu	2.86	2.38	2.77	3.46	3.21	3.34
Ti	18375	13789	12138.61	7790.07	11784.36	9788.02
Tb	1.73	1.33	1.48	1.92	1.86	1.90
Dy	10.45	8.09	8.94	11.80	11.35	11.59
Y	53.69	41.30	46.77	61.75	59.43	60.59
Yb	4.298	3.83	4.25	5.92	5.35	5.63
Lu	0.632	0.60	0.68	0.96	0.84	0.90
Gd	10.91	8.02	9.03	11.58	11.41	11.50
Ho	2.09	1.64	1.83	2.43	2.32	2.38
Er	5.52	4.42	4.88	6.59	6.22	6.41
Tm	0.724	0.63	0.69	0.95	0.87	0.91

Table D-3. Major and compatible trace element bulk rock geochemistry for group 2 used in crystallization model.

Major Element Oxide	Norm. Group 2 Parent	Transition	Low SiO2	Low TiO2 Group 2	High TiO2 Group 2	Average Group 2
SiO2	53.29	55.66	57.49	61.20	60.70	60.95
TiO2	2.41	2.30	2.39	1.33	1.51	1.42
Al2O3	14.82	13.80	13.41	14.74	14.71	14.72
FeO*	10.56	12.13	11.38	9.76	9.64	9.70
MnO	0.17	0.20	0.53	0.18	0.18	0.18
MgO	3.97	3.30	2.43	1.63	1.51	1.57
CaO	9.07	7.15	6.47	4.94	5.05	5.00
Na2O	2.81	3.32	3.07	3.56	3.94	3.75
K2O	1.55	1.69	2.40	2.15	2.12	2.14
P2O5	1.34	0.44	0.76	0.50	0.64	0.57
Total	100.00	100.00	100.35	100.00	100.00	100.00
Compatible Trace						
Sc	31.00	33.13	29.13	26.25	27.58	26.10
Ni	18.00	9.90	5.97	3.83	4.12	3.97
Cr	36.00	7.08	0.00	1.35	4.01	2.68
V	350.00	322.66	153.55	86.01	78.47	82.24

Table D-4. Incompatible trace element bulk rock geochemistry for group 1 used in crystallization model.

Incompatible Trace	Norm. Group 2 Parent	Transition	Low SiO2	Low TiO2 Group 2	High TiO2 Group 2	Average Group 2
Rb	24.79	42.46	38.18	47.38	43.04	45.21
Ba	713.00	705.42	938.64	904.04	904.61	904.32
Th	2.60	5.23	5.27	4.38	4.31	4.35
U	1.25	1.55	2.33	2.15	2.17	2.16
Nb	15.15	13.36	14.79	9.99	11.31	10.65
Ta	1.00	0.88	0.96	0.64	0.71	0.68
K	13320.35	14093.46	16054.91	17860.30	17651.47	17755.89
La	30.17	26.77	31.12	23.49	25.79	24.64
Ce	66.64	56.02	64.03	49.87	55.15	52.51
Pb	5.47	12.13	8.30	9.06	10.68	9.87
Pr	9.75	7.44	8.80	7.00	7.80	7.40
Sr	498.97	339.99	373.73	298.43	342.22	320.32
P	6039.65	1936.60	3910.43	2197.39	2775.41	2486.40
Nd	43.42	31.88	37.55	30.25	33.73	31.99
Zr	179.46	201.81	221.21	197.14	194.73	195.93
Hf	6.66	5.37	5.78	5.27	5.12	5.19
Sm	10.57	7.76	9.00	7.54	8.38	7.96
Eu	3.71	2.38	2.77	2.03	2.45	2.24
Ti	14937.50	13789.44	12138.61	7983.95	9022.65	8503.30
Tb	1.59	1.33	1.48	1.37	1.46	1.41
Dy	10.22	8.09	8.94	8.70	9.00	8.85
Y	49.02	41.30	46.77	47.99	48.02	48.01
Yb	4.23	3.83	4.25	4.71	4.72	4.71
Lu	0.65	0.60	0.68	0.76	0.76	0.76
Gd	10.91	8.02	9.03	7.99	8.69	8.34
Ho	1.97	1.64	1.83	1.84	1.88	1.86
Er	4.99	4.42	4.88	5.10	5.15	5.13
Tm	0.72	0.63	0.69	0.74	0.75	0.75

Table D-5. Group 1 model calculated values

% melt crystallized	0.05	0.10	0.15	0.20	0.25	0.30	0.35	0.40	0.45	0.50	Group 1 Parent	Assemblage
SiO2	54.43	55.18	56.03	56.98	58.05	59.28	60.70	62.35	64.31	66.66	53.75	40.84
TiO2	2.91	2.83	2.73	2.63	2.51	2.37	2.21	2.03	1.81	1.54	2.99	4.44
Al2O3	13.98	13.87	13.76	13.63	13.48	13.31	13.11	12.88	12.61	12.29	14.07	15.86
FeO	11.51	11.26	10.99	10.68	10.34	9.94	9.48	8.95	8.31	7.56	11.73	15.90
MnO	0.19	0.20	0.21	0.22	0.23	0.24	0.25	0.27	0.28	0.31	0.19	0.07
MgO	3.09	2.84	2.56	2.24	1.88	1.46	0.98	0.43	-0.23	-1.02	3.32	7.66
CaO	7.48	7.21	6.90	6.56	6.18	5.73	5.23	4.63	3.93	3.09	7.72	12.35
Na2O	3.10	3.17	3.26	3.35	3.46	3.58	3.73	3.89	4.09	4.32	3.03	1.74
K2O	1.88	1.98	2.10	2.23	2.37	2.54	2.73	2.95	3.22	3.54	1.79	0.04
P2O5	1.49	1.57	1.67	1.77	1.89	2.02	2.18	2.36	2.58	2.83	1.42	0.00
Total	100.06	100.12	100.20	100.28	100.37	100.47	100.60	100.74	100.91	101.11	100.00	99.35

Table D-6. Group 2 model calculated values.

| % melt crystallized	0.05	0.10	0.15	0.20	0.25	0.30	0.35	0.40	0.45	0.50	Group 2 Parent	Assemblage
SiO2	53.83	54.43	55.10	55.86	56.71	57.69	58.82	60.14	61.70	63.56	53.29	43.01
TiO2	2.37	2.32	2.27	2.21	2.15	2.07	1.99	1.89	1.77	1.62	2.41	3.20
Al2O3	14.58	14.31	14.01	13.67	13.28	12.84	12.34	11.74	11.04	10.20	14.82	19.44
FeO	10.47	10.38	10.27	10.15	10.01	9.85	9.67	9.46	9.20	8.90	10.56	12.22
MnO	0.18	0.19	0.20	0.20	0.21	0.22	0.24	0.25	0.27	0.29	0.17	0.06
MgO	3.80	3.61	3.40	3.16	2.89	2.58	2.23	1.81	1.32	0.73	3.97	7.21
CaO	8.92	8.76	8.58	8.38	8.15	7.89	7.59	7.24	6.82	6.32	9.07	11.81
Na2O	2.85	2.89	2.93	2.99	3.04	3.11	3.19	3.28	3.38	3.51	2.81	2.11
K2O	1.63	1.72	1.81	1.92	2.05	2.19	2.36	2.55	2.78	3.05	1.55	0.05
P2O5	1.41	1.49	1.57	1.67	1.78	1.91	2.06	2.23	2.43	2.67	1.34	0.00
Total	100.05	100.10	100.15	100.22	100.29	100.38	100.47	100.58	100.72	100.88	100.00	99.12

Appendix E: Magma Mixing Model

Table E-1. Average icelandite group 1 and 2 geochemistry and GRB like mafic endmembers used in mixing models. All elemental concentrations are in units of ppm.

Element	Average Group 1	Average Group 2	Mafic Endmember Group 1	Mafic Endmember Group 2
Rb	72.6	45.21	41.16	24.79
Ba	1125	904	874	713
Th	8.6	4.35	6.14	2.6
U	2.48	2.16	1.67	1.25
Nb	19.68	10.65	10.6	15.15
Ta	1.26	0.68	0.8	1
K	23127	17756	15194	13320
La	41.97	24.64	33.68	30.17
Ce	86.69	52.51	67.07	66.64
Pb	15.37	9.87	15.31	5.47
Pr	11.42	7.4	9.2	9.747
Sr	312.7	320.32	374.35	498.97
P	2597	2486	6337	6040
Nd	48.03	31.99	40.85	43.42
Zr	294.36	195.93	154.73	179.46
Hf	7.76	5.19	4.28	6.659
Sm	11.42	7.96	10.15	10.57
Eu	3.34	2.24	2.86	2.05
Ti	9788	8503	18375	14938
Tb	1.9	1.41	1.73	1.59
Dy	11.59	8.85	10.45	10.22
Y	60.59	48.01	53.69	49.02
Yb	5.63	4.71	4.298	4.23
Lu	0.9	0.76	0.632	0.647
Gd	11.5	8.34	10.91	10.91
Ho	2.38	1.86	2.09	1.97
Er	6.41	5.13	5.52	4.99
Tm	0.91	0.75	0.724	0.72

Table E-2. Average icelandite group 1 and 2 geochemistry and GRB like mafic endmembers used in mixing models. All elemental concentrations are in units of ppm.

| Element	Average Lower Littlefield	Average Upper Littlefield	Average DIT 1	Average DIT 2	Average DIT 3	Average DIT 4
Rb	144.93	108.25	63.89	74.25	88.49	50.97
Ba	1338	1689	1297	1447	1083	1253
Th	16.44	12.81	6.98	7.08	7.35	5.01
U	5.21	3.65	2.95	3.06	3.28	2.18
Nb	19.75	32.24	20	17.73	23.95	15.54
Ta	1.49	2.03	1.23	1.14	1.43	0.99
K	43539	39820	32113	35614	42618	23284
La	79.54	57.95	38.72	39.41	41.41	30.49
Ce	93.69	118.1	77.16	78.9	87.71	62.61
Pb	23.76	17.96	14.71	13.86	14.88	10.16
Pr	11.24	15.01	10.44	10.5	11.04	8.38
Sr	169.69	176.5	191.64	127.08	56.63	220.03
P	608	233	268	210	415	1460
Nd	85.64	60.43	41.39	42.24	43.63	34.84
Zr	321.46	504.5	381.4	364.11	365.79	255.52
Hf	8.54	13.04	10.13	9.45	9.48	6.67
Sm	9.24	14.04	9.55	9.88	10.13	8.16
Eu	2.65	3.47	1.59	1.93	1.68	2.21
Ti	4233	2398	1762	1883	2524	6142
Tb	1.38	2.41	1.79	1.79	1.78	1.44
Dy	8.31	15.08	11.98	11.7	11.44	9.18
Y	43.43	79.02	67.59	65.12	63.04	51.11
Yb	4.22	8.06	7.88	6.98	6.72	5.13
Lu	0.66	1.27	1.26	1.12	1.08	0.84
Gd	8.35	13.8	9.57	10	9.9	8.38
Ho	1.69	3.13	2.62	2.5	2.42	1.94
Er	4.6	8.68	7.68	7.13	6.85	5.42
Tm	0.67	1.28	1.2	1.08	1.04	0.81

LOWER LITTLEFIELD RHYOLITE MIXING PLOTS
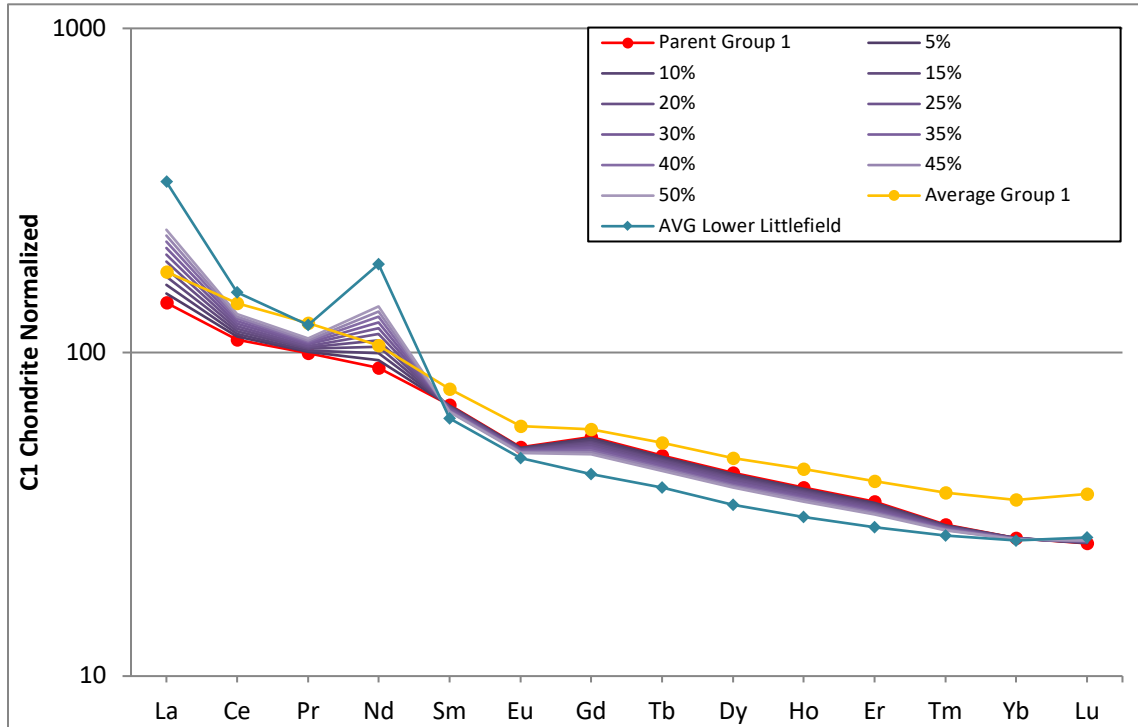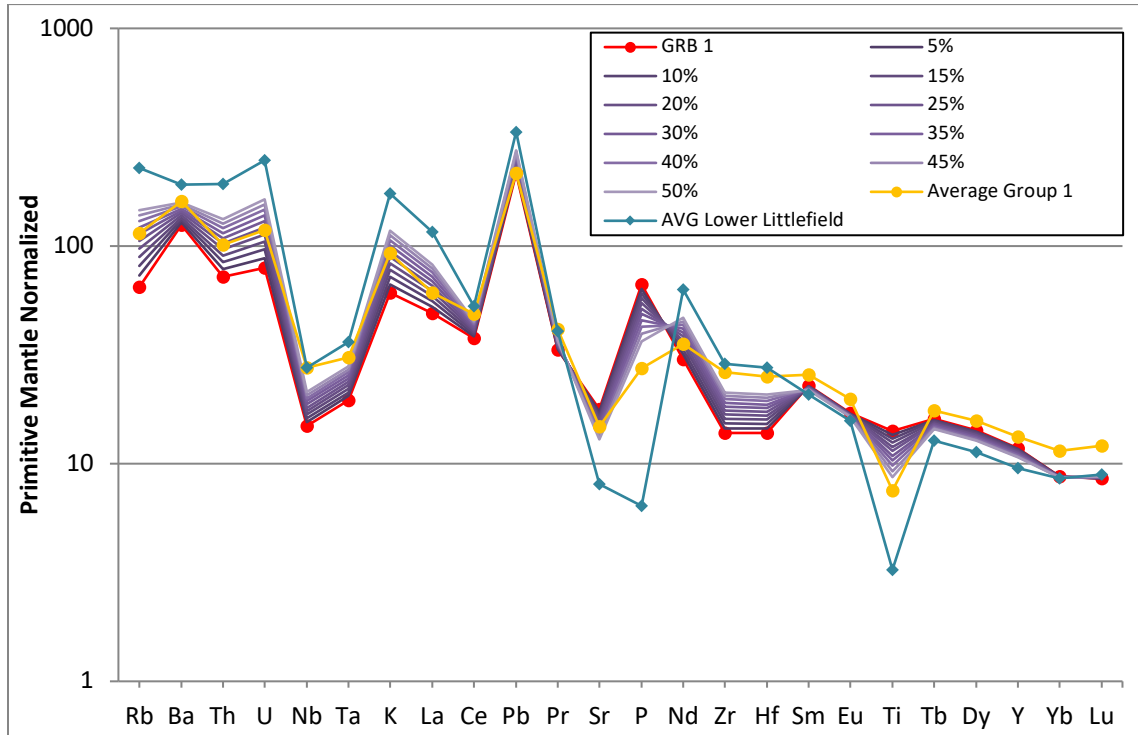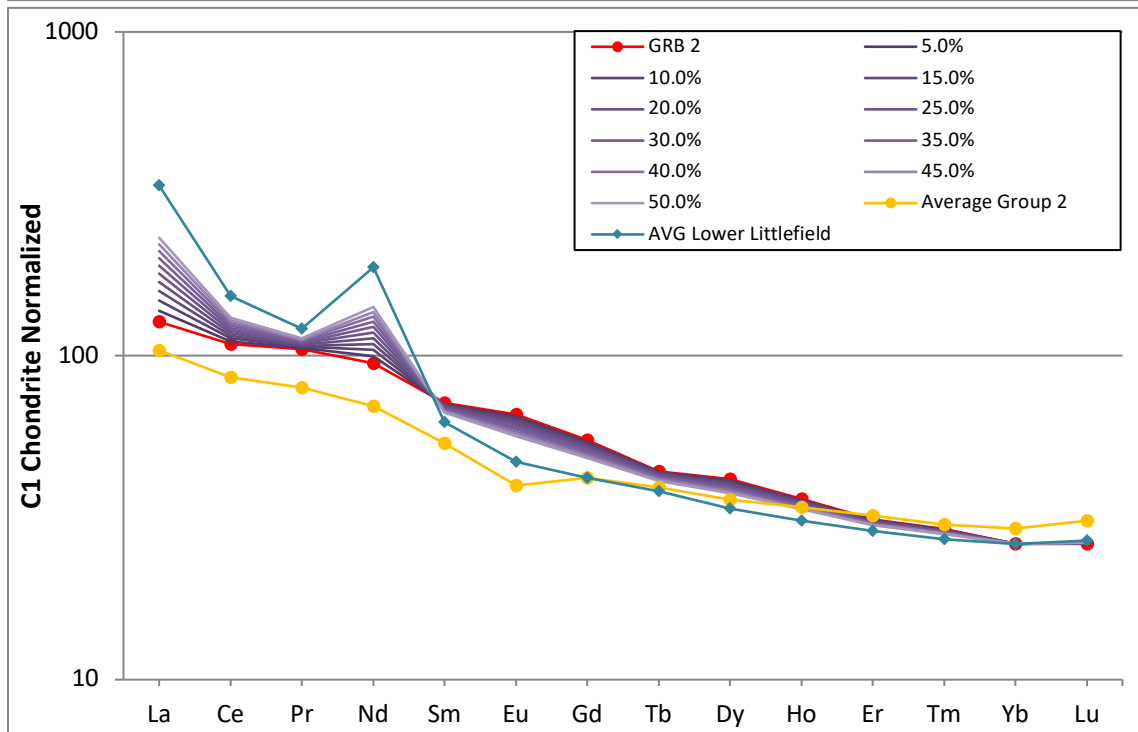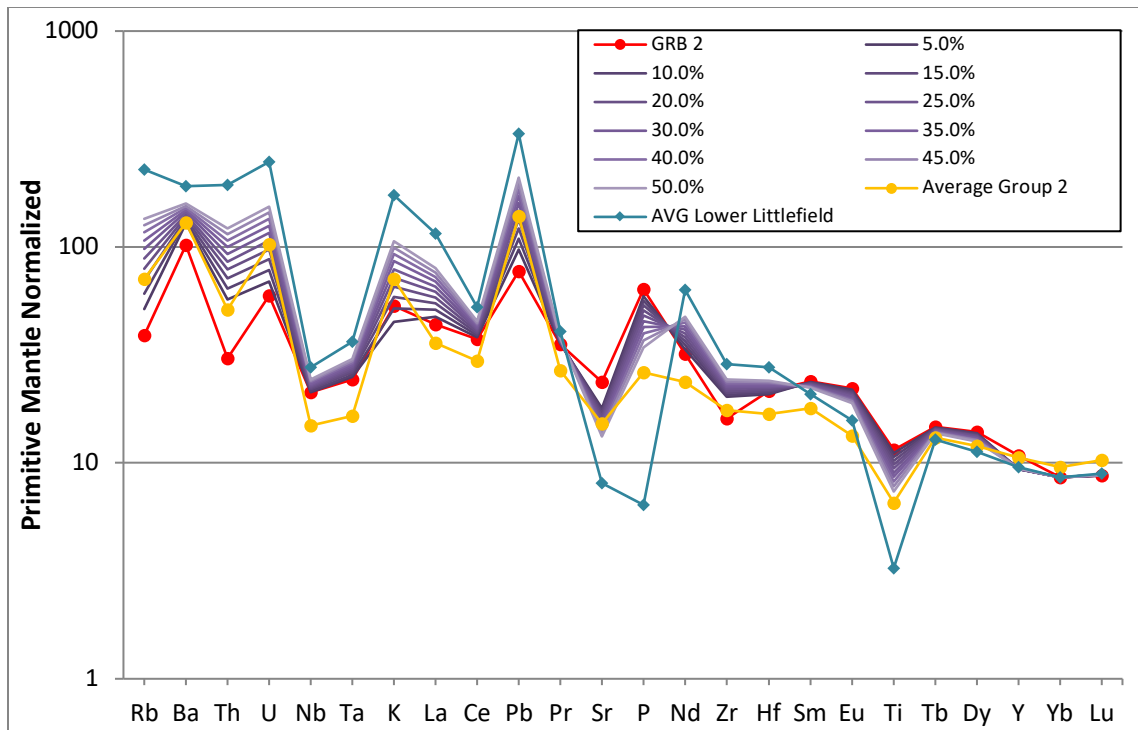
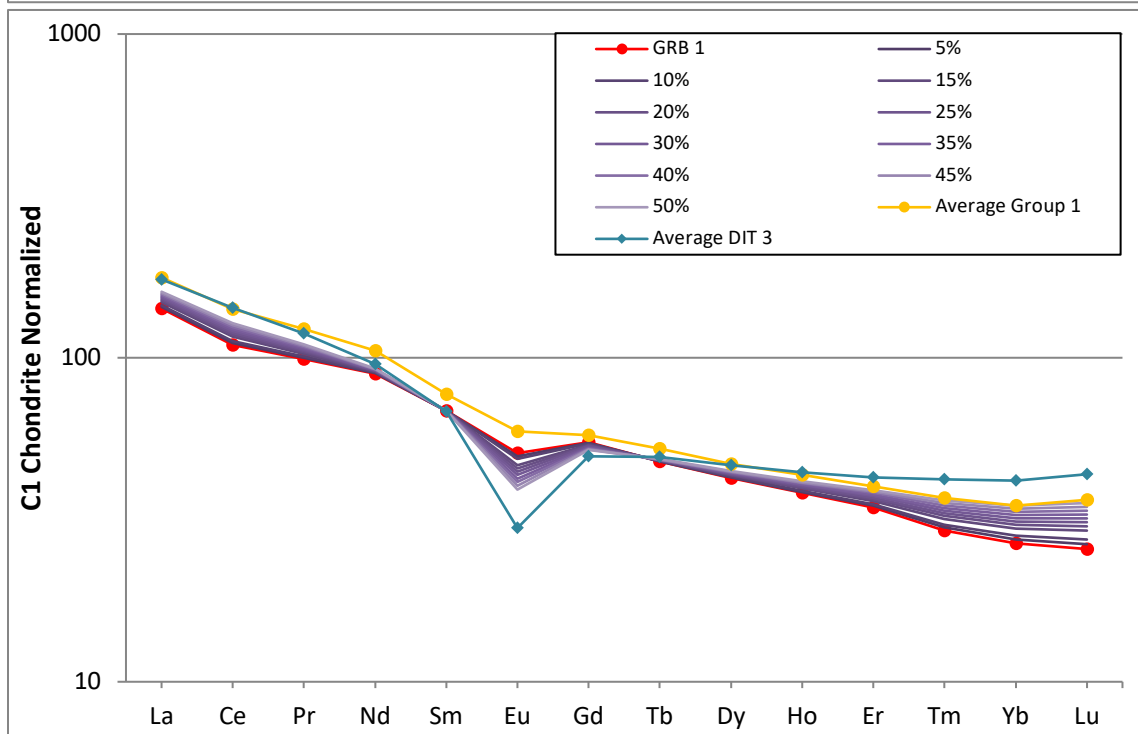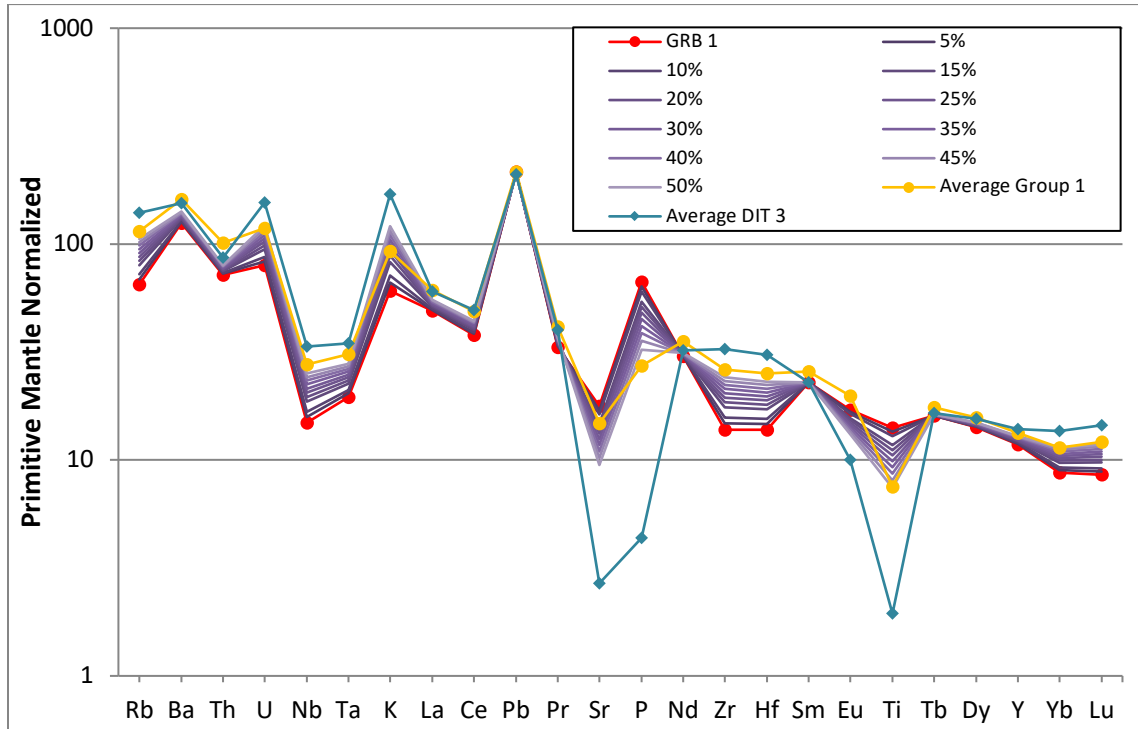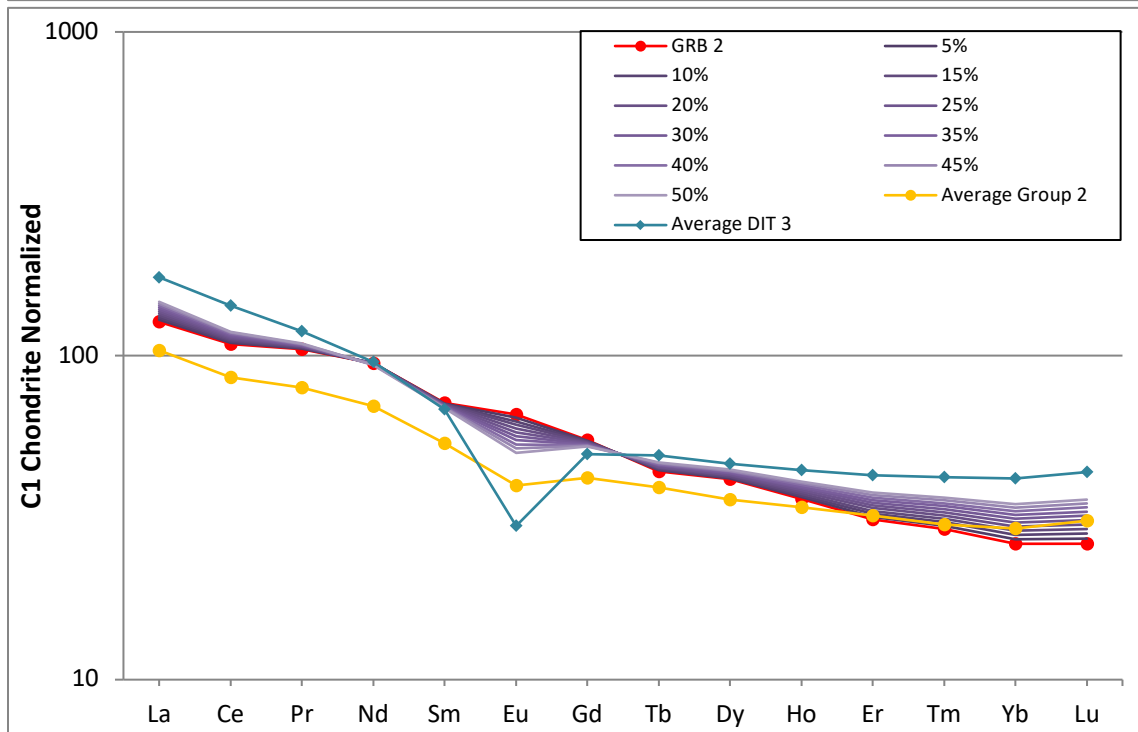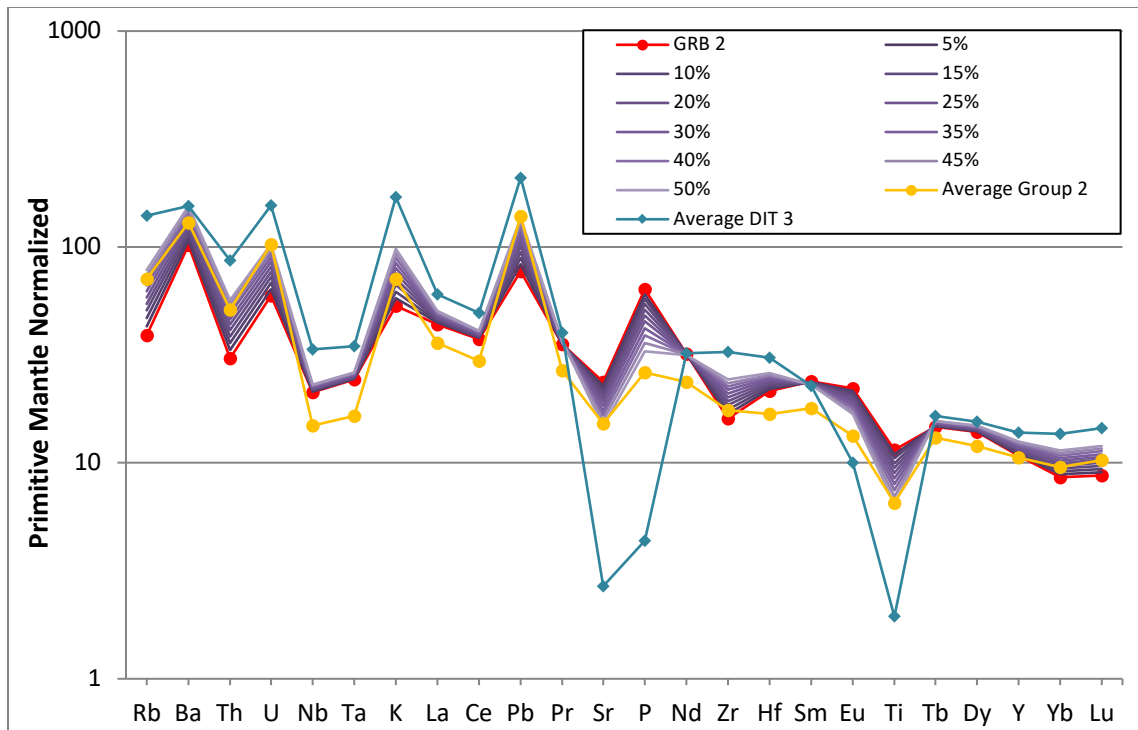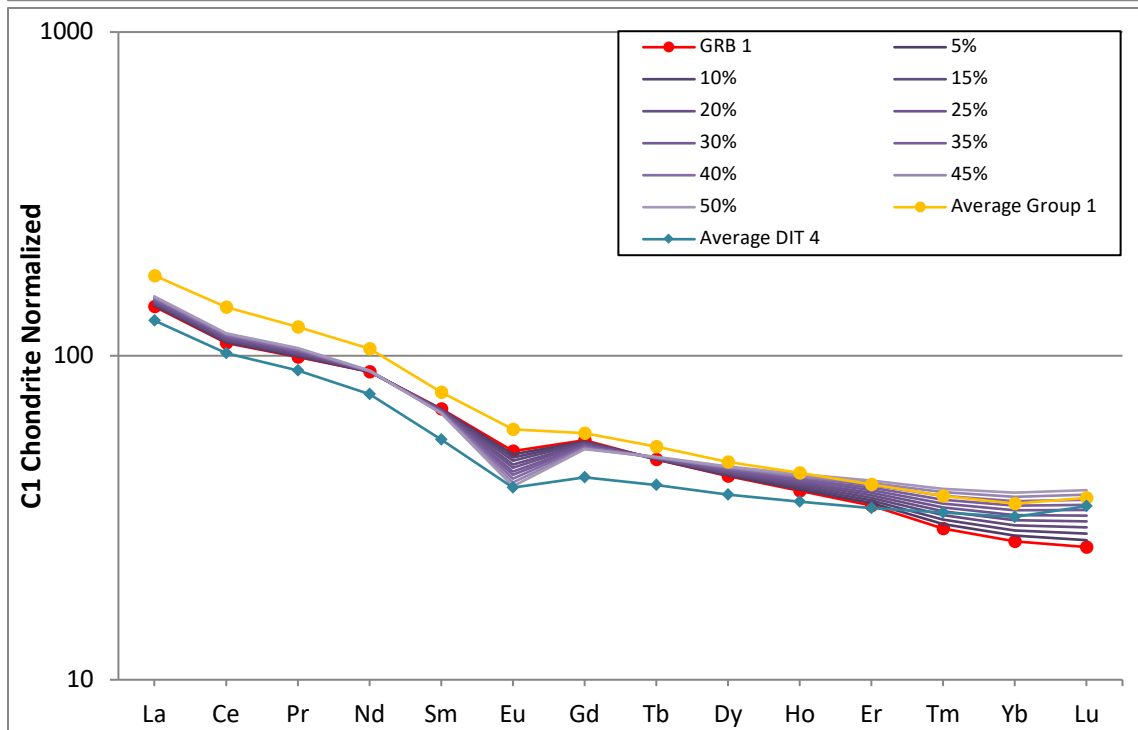# Upper Littlefield Rhyolite Mixing Plots
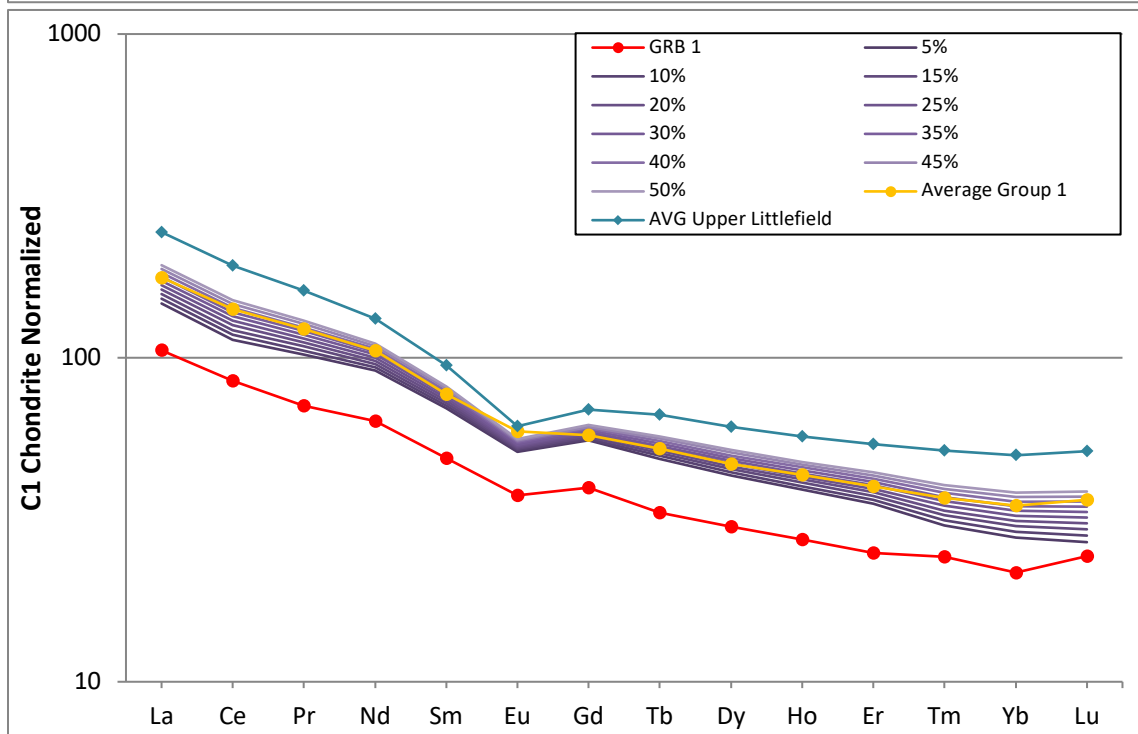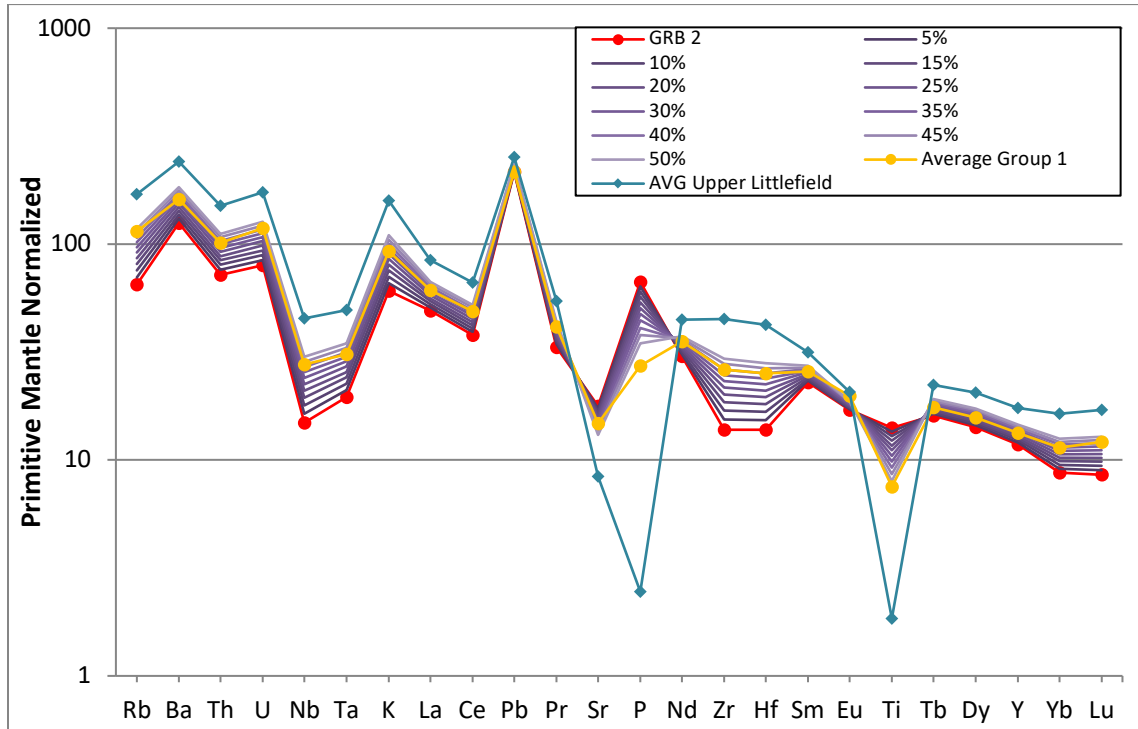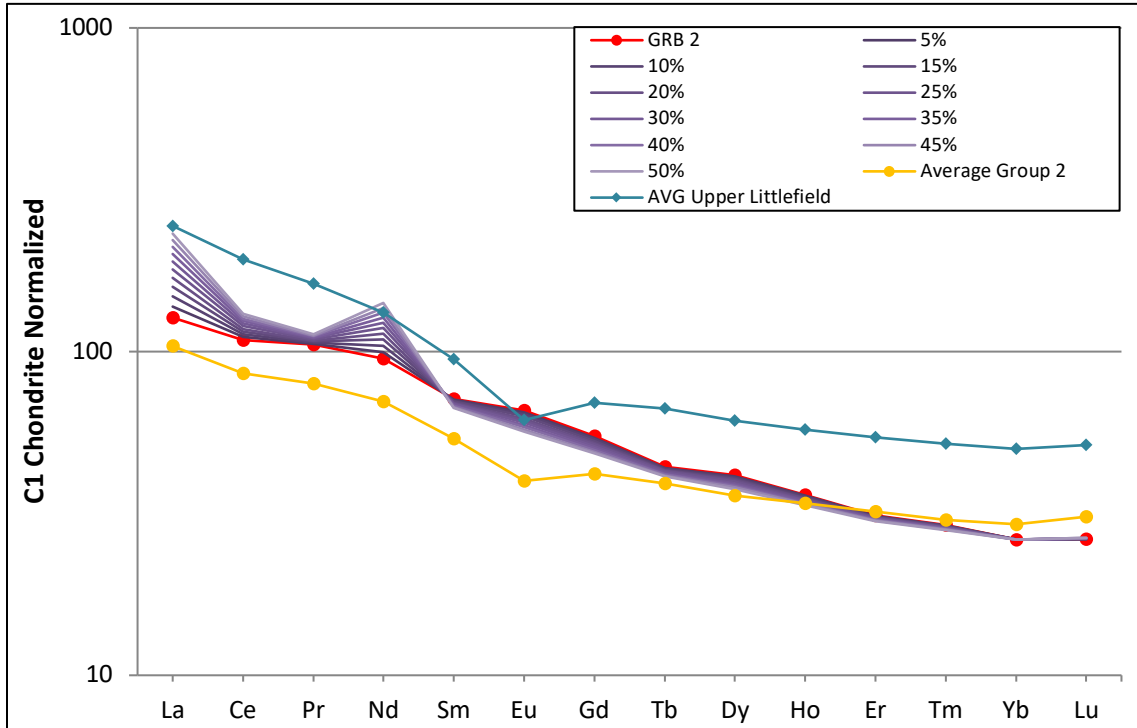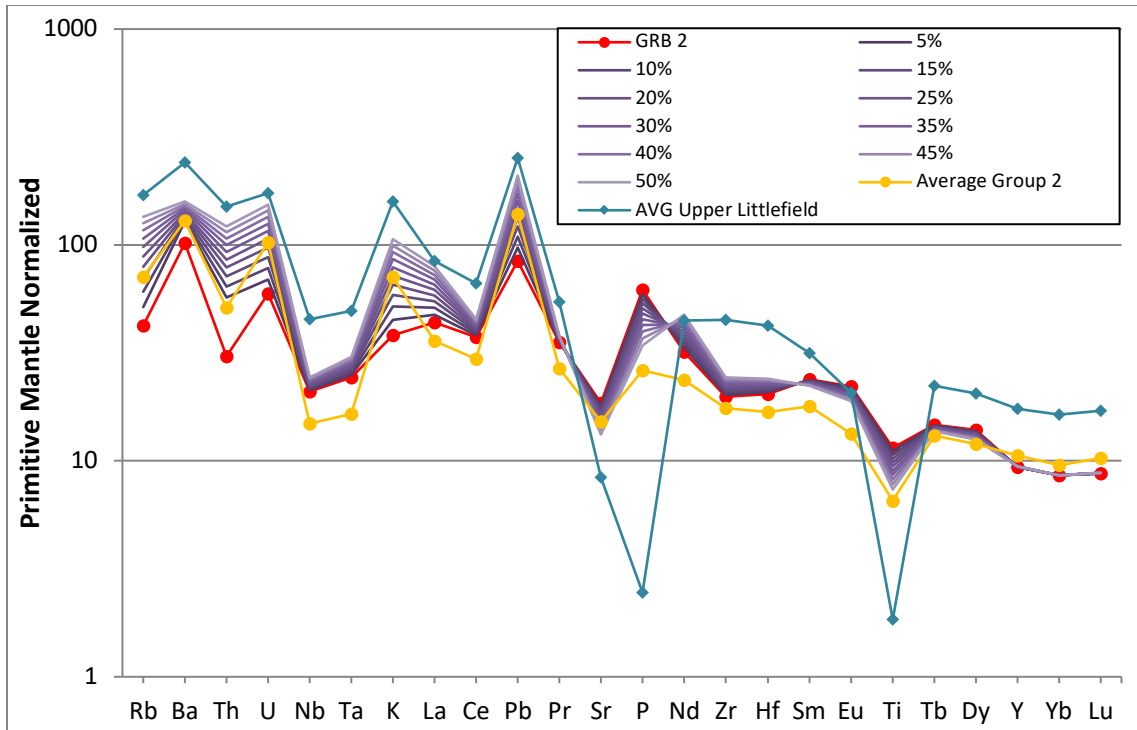
DINNER CREEK TUFF UNIT 1 MIXING PLOTS
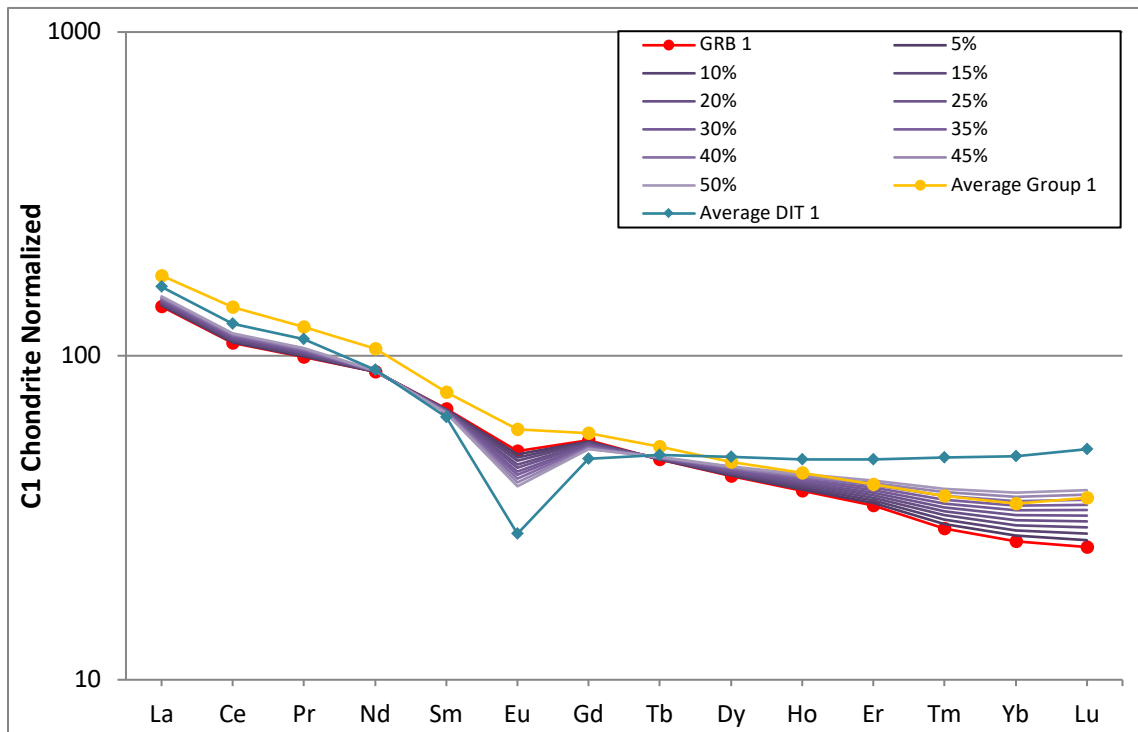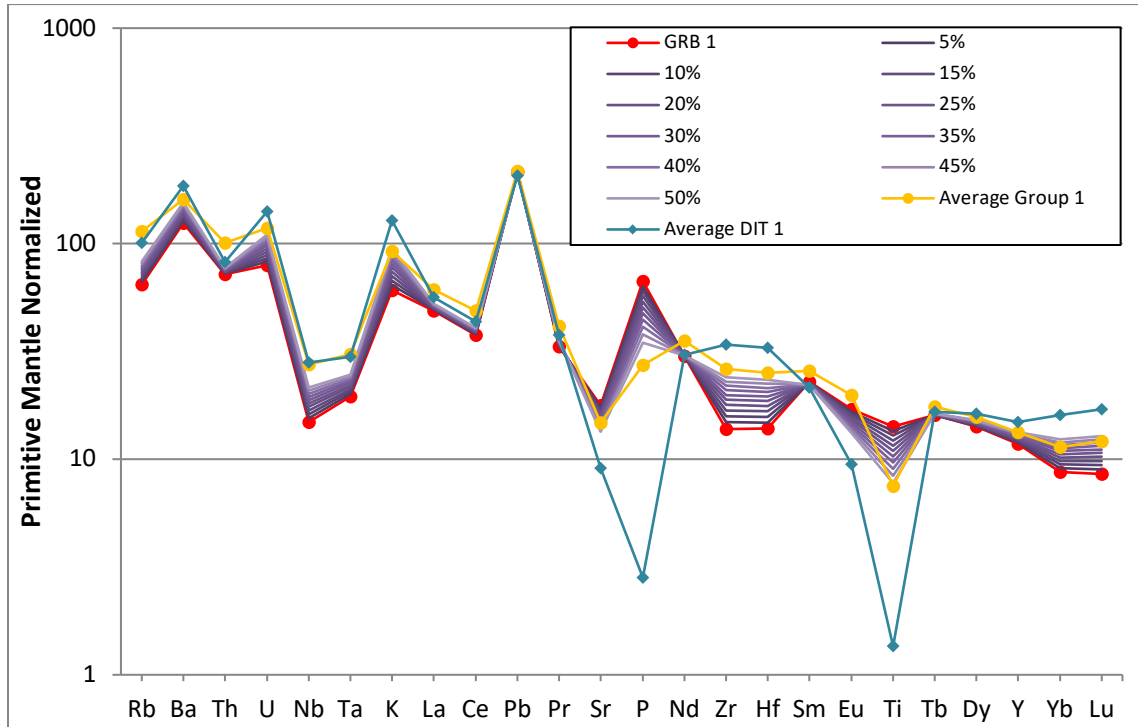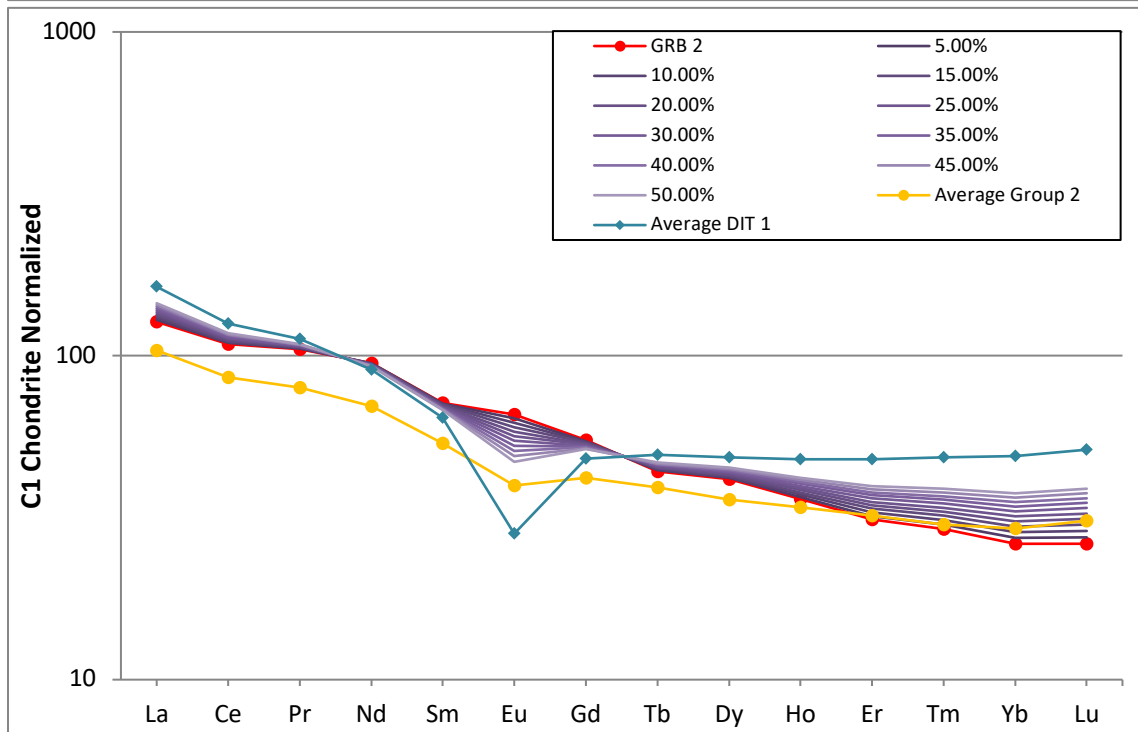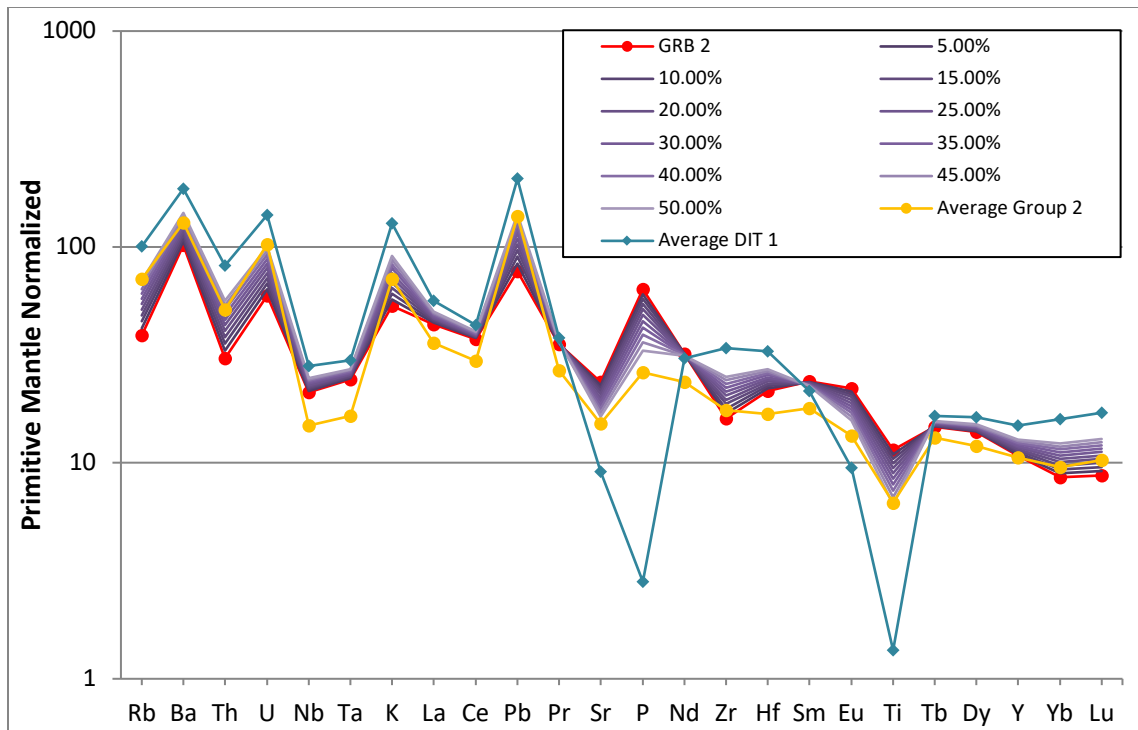
DINNER CREEK TUFF UNIT 2 MIXING PLOTS
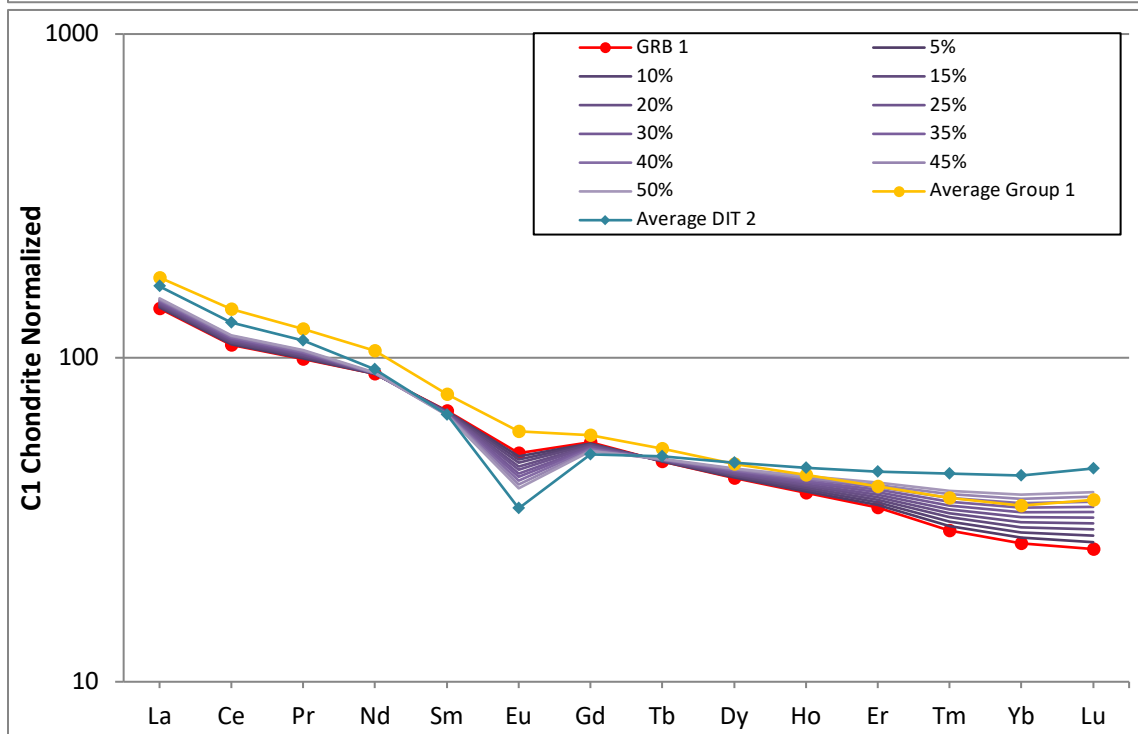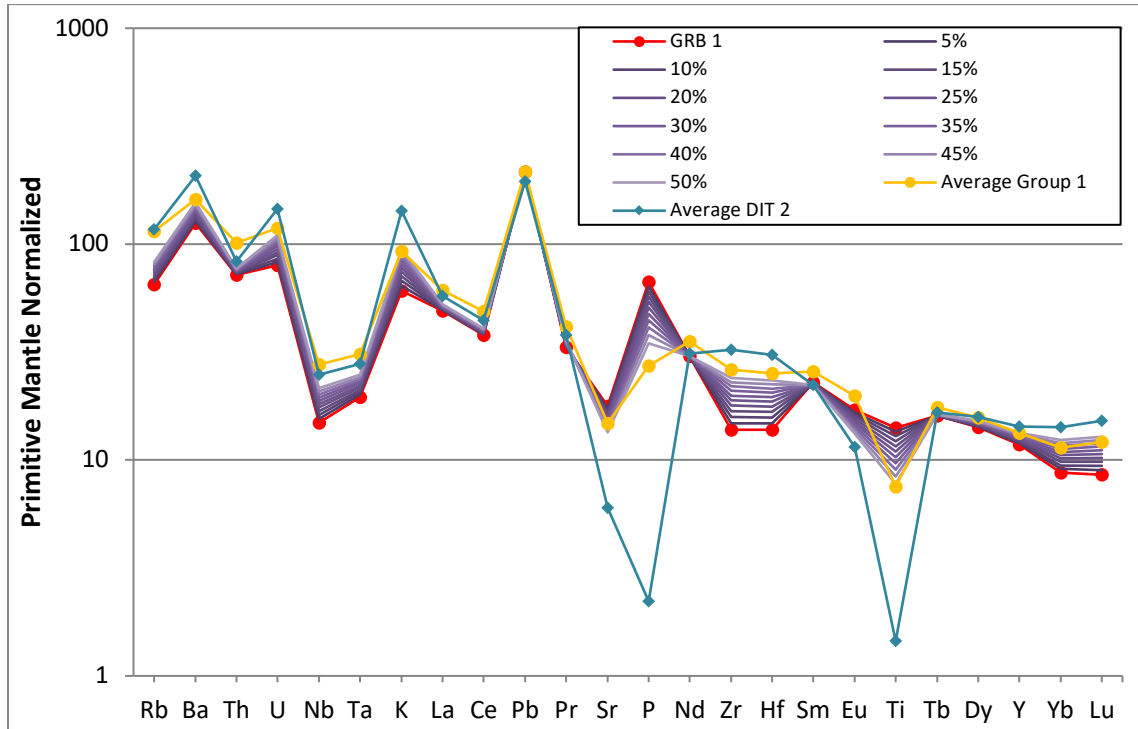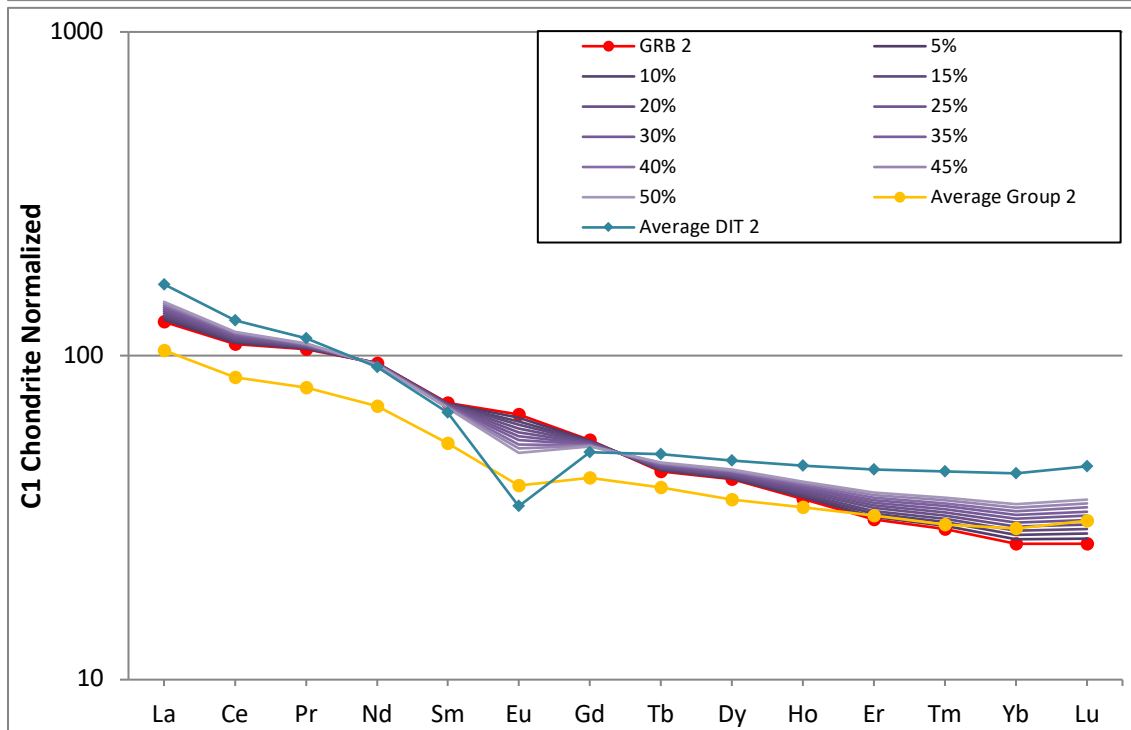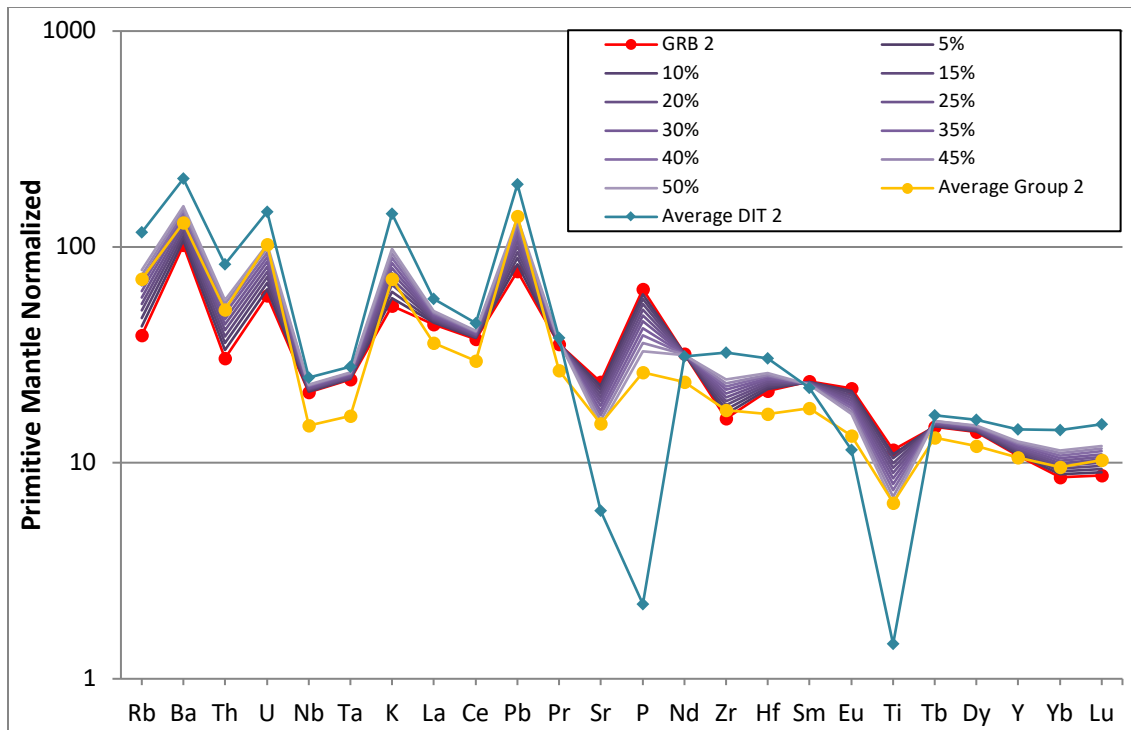
DINNER CREEK TUFF UNIT 3 MIXING PLOTS
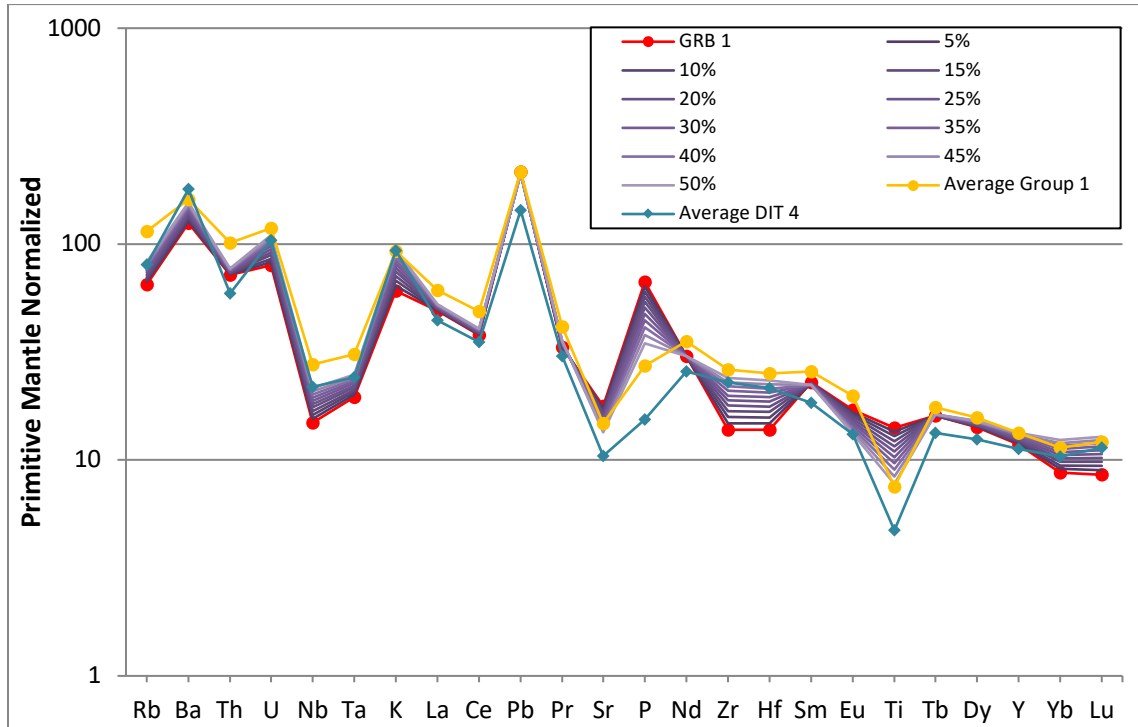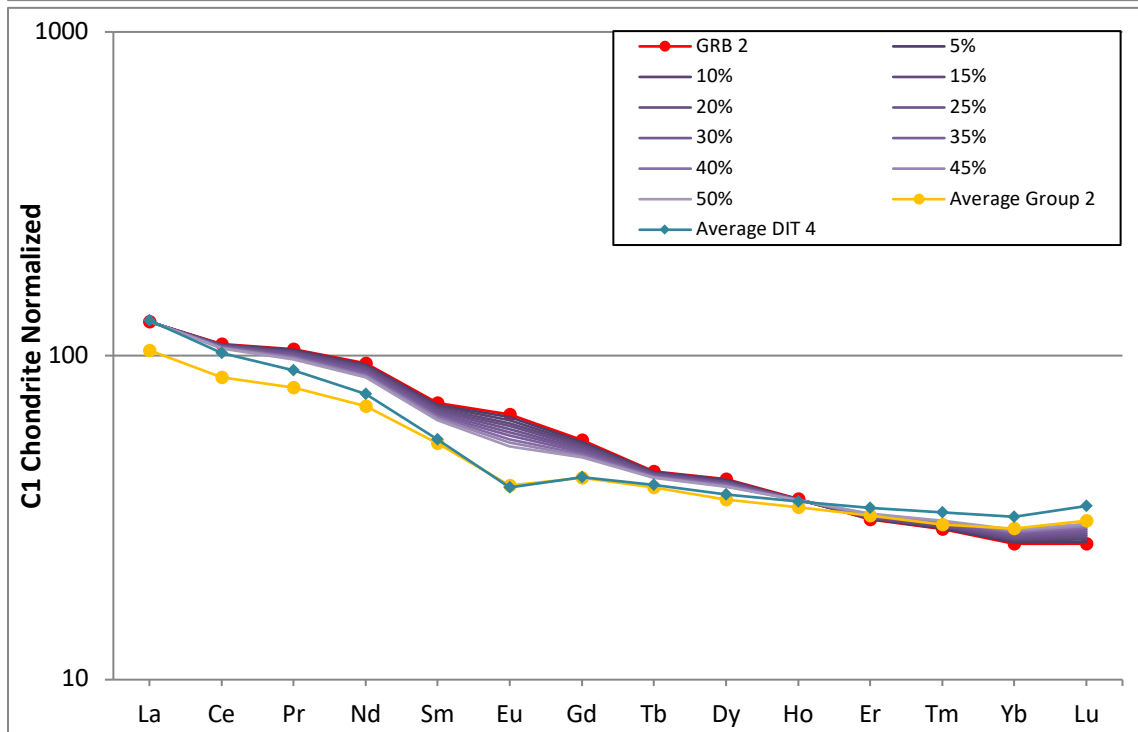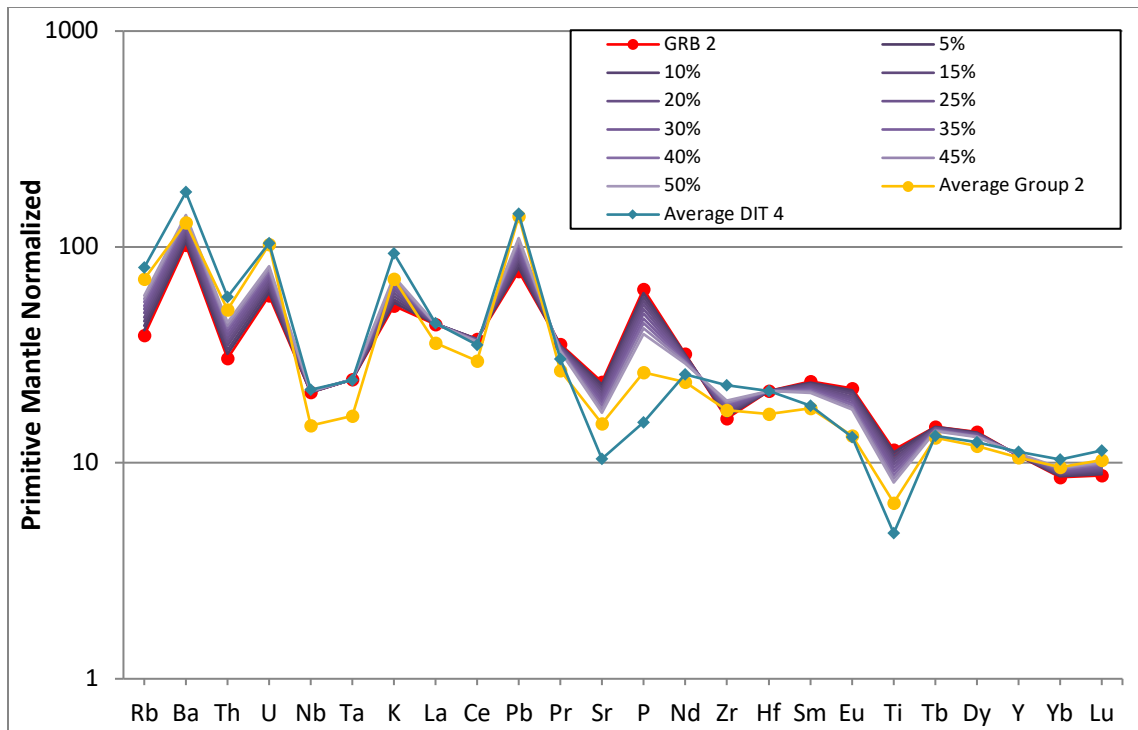
Appendix F: Petrographic Analysis

Table F-1. Locations of samples used for petrographic analysis and status of geochemical analysis.

Sample ID	Easting (m)	Northing (m)	UTM Zone	Geochemical Analysis
MAC-17-04a	373668.06	5003693.36	11N	Yes
MAC-17-06	376393.40	5005731.80	11N	Yes
MAC-17-16	415699.62	5003692.37	11N	Yes
MAC-17-18	412329.51	5038786.97	11N	Yes
MAC-17-29	389606.53	5029335.61	11N	Yes
MC-94-16	418812.57	4900676.68	11N	Yes
MS-12-34	463326.29	4874738.45	11N	Yes
BW-14-37A	433140.00	4826063.21	11N	Yes
BW-14-37B	433167.00	4826016.21	11N	Yes
MC-106-16	409638.45	4909351.14	11N	Yes
MC-98-16	409980.37	4902902.89	11N	No
MC-15-16	407222.62	4873690.51	11N	No
MC-18-16	406509.06	4877655.42	11N	No
MC-101-16	410314.97	4902622.79	11N	No

Table F-2. Petrographic analysis of thin sections.

Sample ID	Unit	Rock	Description
MAC-17-04a	Fiddlers Hell	Icelandite	Aphanitic with groundmass matrix is a mix of plagioclase, clinopyroxene, FeTi-oxide, and glass. groundmass <63μm in size. Phenocrysts and microphenocryst of plag and cpx. simple twinning is present in plag phenocrysts. Some cpx appear to have grown into and around microphenocrysts of plag. Plag are mostly euhedral to subhedral. cpx range from anhedral to subhedral and in shape. At least one cpx exhibits undulatory extinction. Zoning present in larger phenocrysts of plagioclase. plag phenocryst size from 0.8 to 1.7mm and cpx from 0.8-1.2mm
MAC-17-06	Fiddlers Hell	Icelandite	Aphanitic with groundmass matrix is a mix of plagioclase, clinopyroxene, FeTi-oxide, and glass. Plag and cpx phenocrysts and micro phenocrysts. cpx and plag exhibit twinning. Cpx is anhedral to subhedral and plag is subhedral to euhedral. opaque minerals are most likely to be magnetite. plag phenocryst size from 0.3 to 0.79 mm and cpx from 0.17-0.76 mm. several plag also have melt inclusions or secondary mineralization within grain.
MAC-17-16	Fiddlers Hell	Icelandite	Aphanitic with very fine-grained groundmass. Groundmass matrix is a mix of plagioclase, clinopyroxene, FeTi-oxide, and glass. Groundmass is more glassy than other thin sections of Group. Phenocrysts of plag and cpx. Plag are euhedral and cpx are euhedral to subhedral. fractured plag have secondary mineralization in cracks. simple twinning in plag. plag phenocrysts size from 0.27 to 1.59 mm and cpx from 0.16-1.1 mm.
MAC-17-18	Fiddlers Hell	Icelandite	Aphanitic with groundmass matrix is a mix of plagioclase, clinopyroxene, FeTi-oxide, and glass. Groundmass is glassier compared to previous sections. Large euhedral opaque minerals are most likely magnetite. plag are mostly euhedral and cpx is subhedral to anhedral. plag phenocrysts size from 0.49 to 1.15 mm and cpx from 0.36-1.34 mm. plag exhibit simple twinning. some plag crystals also have faint zoning. at least one pyroxene appears to have twinning.
MAC-17-29	Fiddlers Hell	Icelandite	Aphanitic with groundmass matrix is a mix of plagioclase, clinopyroxene, FeTi-oxide, and glass. plag phenocrysts range in size from 0.34 to 0.94 mm and cpx of 0.22-0.63 mm. brown secondary mineralization present in thin section ground mass and in fractured plagioclase. plag have simple twinning.
MC-94-16	Hunter Creek Basalt	Icelandite	Aphanitic with very fine-grained groundmass. Groundmass matrix is a mix of plagioclase, clinopyroxene, FeTi-oxide, and glass. Plag phenocrysts present are euhedral laths with simple twinning, cpx micro phenocrysts also present but are sparse. Cpx micro phenocrysts are anhedral to slightly subhedral. one phenocryst of plag? looks to have embayed crystal and also has reaction rim on exterior of crystal as well as the exterior of the embayed crystal.

Table F-2 cont'd. Petrographic analysis of thin sections.

Sample ID	Unit	Rock	Description
MS-12-34	Hunter Creek at Neal Hot Springs	Icelandite	Contains sparse phenocrysts of plagioclase feldspar and clinopyroxene. Plag phenocrysts and the cpx phenocrysts range from moderately anhedral to euhedral. Two largest cpx and at least 5 plag phenocrysts show textures that are consistent with being actively resorbed. The texture of the sample is aphanitic, and the phenocryst content is between 1-1.5% at most.
BW-14-37A	Icelandite of Alder Creek	Icelandite	Aphanitic texture containing groundmass feldspar, magnetite, clinopyroxene, and interstitial glass. Contains rare large (1-3.5 mm) tabular plagioclase feldspar phenocrysts.
BW-14-37B	Icelandite of Alder Creek	Icelandite	Aphanitic texture containing groundmass feldspar, magnetite, clinopyroxene, and interstitial glass. Contains rare large (1-3.5 mm) tabular plagioclase feldspar phenocrysts.
MC-106-16	Hunter Creek Basalt	Icelandite	Microlitic texture. Gray fine plagioclase lathe and brown-black glass groundmass in PP, dark gray in XP. 0 - 5 % euhedral plagioclase phenocrysts, simple twinning. Opaque minerals are probably magnetite. (Cruz, 2017)
MC-98-16	Hunter Creek Basalt	Icelandite	Microlitic texture. Gray fine plagioclase lathe and brown-black glass groundmass in PP, dark gray in XP. 0 - 5 % euhedral plagioclase phenocrysts, simple twinning. Opaque minerals are probably magnetite. (Cruz, 2017)
MC-15-16	Hunter Creek Basalt	Icelandite	Microlitic texture. Gray fine plagioclase lathe and brown-black glass groundmass in PP, dark gray in XP. Opaque minerals are probably magnetite. (Cruz, 2017)
MC-18-16	Hunter Creek Basalt	Icelandite	Microlitic texture. Gray fine plagioclase lathe and brown-black glass groundmass in PP, dark gray in XP. Opaque minerals are probably magnetite. (Cruz, 2017)
MC-101-16	Hunter Creek Basalt/DIT2?	Tuff?	Microlitic texture. Brown glass, with calcite replacing plagioclase and/or glass. Circular zeolite along contact with DIT2.Opaque minerals are probably magnetite. (Cruz, 2017)

Thin section images on pages 145-171 are taken at 100x magnification.

MAC-17-04a

MAC-17-04a

MAC-17-04a

Plag

MAC-17-04a

Plag

MAC-17-04a

MAC-17-04a

MAC-17-04a

Cpx

Vesicle

MAC-17-04a

Plag

Vesicle

MAC-17-06

Cpx

MAC-17-06

Plag

157

MAC-17-06

MAC-17-06

MAC-17-06

MAC-17-06

MAC-17-06

MAC-17-06

MAC-17-16

Plag

MAC-17-16

MAC-17-16

Plag

Cpx

MAC-17-16

MAC-17-16

MAC-17-16

MAC-17-18

MAC-17-18

MAC-17-18

MAC-17-18

MAC-17-18

MAC-17-18

MAC-17-29

MAC-17-29

MAC-17-29

MAC-17-29

MAC-17-29

MAC-17-29

MC-94-16

5 mil

MC-94-16

Cpx

Plag

5 mil

170

MC-94-16

Plag

5 mil

MS-12-34

Cpx

100x

MS-12-34

FeTi Oxide

100x

MS-12-34

Plag

100x

MS-12-34

Plag

100x